SMIP22

SMIP22 SEMINAR ON
UTILIZATION OF STRONG-MOTION DATA

October 12, 2022

PROCEEDINGS

Sponsored by

California Strong Motion Instrumentation Program
California Geological Survey
California Department of Conservation

Co-Sponsors

California Seismic Safety Commission
California Governor's Office of Emergency Services
California Department of Health Care Access and Information
California Department of Transportation

California
Department of
Conservation
California Geological Survey

The California Strong Motion Instrumentation Program (CSMIP), a program within the California Geological Survey (CGS) of the California Department of Conservation, records the strong shaking of the ground and structures during earthquakes for analysis and utilization by the engineering and seismology communities, through a statewide network of strong motion instruments (www.conservation.ca.gov/CGS/smip). CSMIP is advised by the Strong Motion Instrumentation Advisory Committee (SMIAC), a committee of the California Seismic Safety Commission. Major program funding is provided by an assessment on construction costs for building permits issued by cities and counties in California, with additional funding from the California Governor's Office of Emergency Services (Cal OES), the California Department of Health Care Access and Information (HCAI) and the California Department of Transportation (Caltrans).

In July 2001, Cal OES began funding for the California Integrated Seismic Network (CISN), a newly formed consortium of institutions engaged in statewide earthquake monitoring that grew out of TriNet, funded by FEMA, and included CGS, USGS, Caltech and UC Berkeley. The goals of CISN are to record and rapidly communicate ground shaking information in California, and to analyze the data for the improvement of seismic codes and standards (www.cisn.org). CISN produces ShakeMaps of ground shaking, based on shaking recorded by stations in the network, within minutes following an earthquake. The ShakeMap identifies areas of greatest ground shaking for use by Cal OES and other emergency response agencies in the event of a damaging earthquake.

The Center for Engineering Strong Motion Data (CESMD) is operated by the CSMIP in cooperation with the National Strong-Motion Project (NSMP), a part of the Advanced National Seismic System (ANSS) of the U.S. Geological Survey (USGS). The CESMD builds on and incorporates the CISN Engineering Data Center and will continue to serve the California region while expanding to serve other ANSS regions. The Data Center provides strong-motion data rapidly after a significant earthquake in the United States. Users also have direct access to data from previous earthquakes and detailed information about the instrumented structures and sites. The CESMD also provides access to the U.S. and international strong ground motion records through its Virtual Data Center (VDC). The Data Center is co-hosted by CGS and USGS at www.strongmotioncenter.org

DISCLAIMER

SMIP22

SMIP22 SEMINAR ON
UTILIZATION OF STRONG-MOTION DATA

October 12, 2022

PROCEEDINGS

Edited by

Daniel Swensen

Sponsored by

California Strong Motion Instrumentation Program
California Geological Survey
California Department of Conservation

Co-Sponsors

California Seismic Safety Commission
California Governor's Office of Emergency Services
California Department of Health Care Access and Information
California Department of Transportation

PREFACE

The California Strong Motion Instrumentation Program (CSMIP) in the California Geological Survey of the California Department of Conservation established a Data Interpretation Project in 1989. Each year CSMIP funds several data interpretation contracts for the analysis and utilization of strong-motion data. The primary objectives of the Data Interpretation Project are to further the understanding of strong ground shaking and the response of structures, and to increase the utilization of strong-motion data in improving post-earthquake response, seismic code provisions and design practices.

As part of the Data Interpretation Project, CSMIP holds annual seminars to transfer recent research findings on strong-motion data to practicing seismic design professionals, earth scientists and post-earthquake response personnel. The purpose of the annual seminar is to provide information that will be useful immediately in seismic design practice and post-earthquake response, and in the longer term, useful in the improvement of seismic design codes and practices. Proceedings and individual papers for each of the previous annual seminars are available at http://www.conservation.ca.gov/cgs/smip/seminar in PDF format. Due to State budget constraints, CSMIP did not hold an annual seminar in 2010 or 2011. The SMIP22 Seminar is the thirty-first in this series of annual seminars.

The SMIP22 Seminar is divided into two sessions in the morning and two sessions in the afternoon. There are seven presentations in total; six are on the results of CSMIP-funded projects. The sessions in the morning include three presentations. The first session will commemorate the 50th anniversary of CSMIP. Farzad Naeim, SMIAC Chair, and Hamid Haddadi, CSMIP Program Manager, will present on the history, accomplishments, and future direction of CSMIP. The second session will focus on ground response topics. Professor Ziotopoulou of UC Davis will present on developing input motions for site response and nonlinear deformation analyses. She will be followed by a presentation from Professor Stewart of UCLA on horizontal-to-vertical spectral ratio peak protocols.

The two sessions in the afternoon include four presentations. The third session will focus on structural response topics. Professor Kunnath of UC Davis will present on ASCE-41 nonlinear modeling guidelines and acceptance criteria for reinforced concrete shear wall buildings. He will be followed by a presentation from Professor Tsampras of UC San Diego on diaphragm seismic design provisions and higher-mode responses of buildings. The last session will focus on lifeline response topics. Professor Olsen of San Diego State University will present on seismic hazard analysis of embankment dams. He will be followed by a presentation from Professor Athanasopoulos-Zekkos of UC Berkeley on dynamic response parameters of earth dams. Individual papers and the proceedings are available for download by the SMIP22 participants at the provided link and will be available at the CSMIP website in the future.

Daniel Swensen
CSMIP Data Interpretation Project Manager

Appreciation to Members of the Strong Motion Instrumentation Advisory Committee

Main Committee

Farzad Naeim, Chair, Farzad Naeim, Inc.
Norman Abrahamson, UC Berkeley
Bruce Clark, Leighton & Associates
Martin Eskijian, California State Lands Commission (retired)
David Gutierrez, GEI Consultants
Marshall Lew, Wood
Bret Lizundia, Rutherford + Chekene
Carlos Ventura, University of British Columbia
Chris Tokas, California Department of Health Care Access and Information
Chris Traina, California Department of Transportation
Jia Wang-Connelly (ex-officio), Seismic Safety Commission

Ground Response Subcommittee

Marshall Lew, Chair, Wood
Zia Zafir, Kleinfelder
Martin Hudson, Turner

Buildings Subcommittee

Bret Lizundia, Chair, Rutherford + Chekene
Lucie Fougner, Degenkolb Engineers
Ifa Kashefi, City of Los Angeles (retired)
Michelle Yu, City of San Francisco
Eduardo Miranda, Stanford University
Roy Lobo, California Department of Health Care Access and Information
Chia-Ming Uang, UC San Diego

Lifelines Subcommittee

Martin Eskijian, Chair, California State Lands Commission (retired)
David Gutierrez, GEI Consultants
Faiz Makdisi, Gannett Fleming
Chris Traina, California Department of Transportation

Data Utilization Subcommittee

Representatives from each Subcommittee

TABLE OF CONTENTS

Final Program v

Broadening the Utilization of CSMIP Data: Double Convolution Methodology towards Developing Input Motions for Site Response & Nonlinear Deformation Analyses 1
Renmin Pretell, S. K. Sinha, Katerina Ziotopoulou, Jennie Watson-Lamprey and Dimitrios Zekkos

Measurement and Identification Protocols for Horizontal-to-Vertical Spectral Ratio Peaks 13
Pengfei Wang, Paolo Zimmaro, Sean K. Ahdi, Alan Yong and Jonathan P. Stewart

Enhancing ASCE-41 Nonlinear Modeling Guidelines and Acceptance Criteria using Instrumented Reinforced Concrete Shear Wall Buildings 14
Laura Hernandez-Bassal and Sashi Kunnath

Validation of Seismic Design Provisions for Diaphragms and Assessment of Higher-Mode Responses on Earthquake-Resistant Buildings 28
C. Franco Mayorga and Georgios Tsampras

Next Generation Seismic Hazard Analysis of Embankment Dams: Case of the Long Valley Dam, CA 43
Kim Olsen, T.-Y. Yeh and Daniel Roten

Using CSMIP Data to Derive Reliable Values of Dynamic Response Parameters for Earth Dams in California 64
Makbule Ilgac and Adda Athanasopoulos-Zekkos

SMIP22 SEMINAR ON UTILIZATION OF STRONG-MOTION DATA

October 12, 2022

FINAL PROGRAM

9:15 am **WELCOMING REMARKS**
Farzad Naeim, Chair, Strong Motion Instrumentation Advisory Committee (SMIAC)
David Shabazian, Director, California Department of Conservation

9:25 am **INTRODUCTION**
Hamid Haddadi, Program Manager, California Strong Motion Instrumentation Program
Dan Swensen, Senior Civil Engineer, California Strong Motion Instrumentation Program

Session I

Moderator: *Chris Tokas*, HCAI and SMIAC

9:30 am **50th Anniversary of CSMIP: Past, Present and Future**
Hamid Haddadi, California Strong Motion Instrumentation Program
Farzad Naeim, SMIAC

10:30 am **Break**

Session II

Moderator: *Zia Zafir*, Kleinfelder and SMIAC

11:00 am **Broadening the Utilization of CSMIP Data: Double Convolution Methodology towards Developing Input Motions for Site Response & Nonlinear Deformation Analyses**
Renmin Pretell, S. K. Sinha and *Katerina Ziotopoulou*, UC Davis
Jennie Watson-Lamprey, Slate Geotechnical Consultants
Dimitrios Zekkos, UC Berkeley

11:30 am **Measurement and Identification Protocols for Horizontal-to-Vertical Spectral Ratio Peaks**
Pengfei Wang, Paolo Zimmaro and *Jonathan P. Stewart*, UC Los Angeles
Sean K. Ahdi and Alan Yong, US Geological Survey

12:00 pm **Lunch Break**

Session III

Moderator: *Bret Lizundia*, Rutherford + Chekene and SMIAC

1:00 pm **Enhancing ASCE-41 Nonlinear Modeling Guidelines and Acceptance Criteria using Instrumented Reinforced Concrete Shear Wall Buildings**
Laura Hernandez-Bassal and *Sashi Kunnath*, UC Davis

1:30 pm **Validation of Seismic Design Provisions for Diaphragms and Assessment of Higher-Mode Responses on Earthquake-Resistant Buildings**
C. Franco Mayorga and *Georgios Tsampras*, UC San Diego

2:00 pm **Break**

Session IV

Moderator: *Martin Eskijian*, California State Lands Commission and SMIAC

2:30 pm **Next Generation Seismic Hazard Analysis of Embankment Dams: Case of the Long Valley Dam, CA**
Kim Olsen, T.-Y. Yeh and Daniel Roten, San Diego State University

3:00 pm **Using CSMIP Data to Derive Reliable Values of Dynamic Response Parameters for Earth Dams in California**
Makbule Ilgac and *Adda Athanasopoulos-Zekkos*, UC Berkeley

3:30 pm **Adjourn**

BROADENING THE UTILIZATION OF CSMIP DATA: DOUBLE CONVOLUTION METHODOLOGY TOWARDS DEVELOPING INPUT MOTIONS FOR SITE RESPONSE AND NONLINEAR DEFORMATION ANALYSES

Renmin Pretell[(1)], Sumeet K. Sinha[(2)], Katerina Ziotopoulou[(1)], Jennie A. Watson-Lamprey[(3)], and Dimitrios Zekkos[(2)]

[(1)] Department of Civil and Environmental Engineering, University of California, Davis
[(2)] Department of Civil and Environmental Engineering, University of California, Berkeley
[(3)] Slate Geotechnical Consultants

Abstract

The double convolution methodology for the development of input motions for site response analyses and nonlinear deformation analyses is briefly presented. This methodology uses deep V_S profiles and random vibration theory to modify ground motions recordings from top-of-soil stations ("reference site") such that they are compatible with conditions at a neighboring location ("target site") and some selected depth (halfspace), while preventing numerical errors associated with the inverse nature of a deconvolution analysis. The methodology can be particularly useful for obtaining input ground motions for the forensic investigation of case histories or further modified to meet some design criteria and used for site response analyses and the subsequent determination of hazard at the surface for the seismic performance assessment of structures. The proposed approach is termed "double convolution" as it uses two site response analyses (SRAs) to compute a desired transfer function (TF). The methodology is briefly presented followed by a demonstration of its implementation in an open-access webtool.

Introduction

Ground surface seismic stations are dominant in most seismic networks around the world. Recordings from these stations are commonly used as input motions in site response analyses (SRAs) and 2- or 3-dimensional (2D or 3D hereafter) nonlinear deformation analyses (NDAs) employed for (1) the design of structures such as dams, bridges, and buildings; and (2) the study of case histories either towards validating numerical procedures or towards forensically investigating possible causes of failures (e.g., Pretell et al. 2021). For instance, Figure 1 presents a schematic of a typical scenario where input ground motions are needed for the evaluation of the seismic performance of a dam using NDAs. In this case, the target site and depth are the location of the dam and the depth of the halfspace, respectively.

Common approaches for developing input ground motions for the design of structures consist of two steps: (1) the selection of recordings based on a seismic scenario and site conditions consistent with the halfspace; and (2) the modification of the recordings to approximately match a spectral shape, a ground motion intensity measure, or meet some other criterion such that the resulting ground motions are consistent with the halfspace (e.g., Abrahamson 1992a, Hancock et al. 2006, Watson-Lamprey and Abrahamson 2006, Baker et al. 2011, Arteta and Abrahamson 2019, Mazzoni et al. 2020). The first step strongly depends on the

candidate recordings available, which are often selected from recording stations (i.e., reference site in Figure 1) that have an inverse of the average slowness on the top 30 m (V_{S30}) higher than 760 m/s, i.e. rock sites (ASCE 2016). These stations are commonly referred to as "outcropping rock." Outcropping rock stations are not widely available in shallow crustal tectonic regions as they add up to only 3% of the ground motion recordings from the Center for Engineering Strong Motion Data (CESMD) as of June 2020. In the case of forensic studies, the ability to replicate the case history strongly depends on available seismic stations as candidate ground motions should be representative of the specific seismic scenario, at a specific location and depth. The limited number of ground motions recorded at outcropping rock sites leads practitioners and researchers to use ground surface motions recorded at soil sites, hereafter referred to as "ground surface recordings," with some modifications.

Several procedures are used for the development of input ground motions in the absence of recordings from rock stations. A common approach is deconvolution analysis, which is a type of 1D SRA that allows for the computation of ground motions that would have been recorded at some depth given ground motion recordings at the ground surface at the same site. Deconvolution can occasionally lead to numerical errors and spurious ground motions (Kramer 1996). Other approaches for the modification of ground surface recordings include the procedures proposed by Cabas and Rodriguez-Marek (2017) and Ntritsos et al. (2021), which respectively use V_S-κ_0 correction factors, and a four-step approach including deconvolution to account for differences between the target and reference (i.e., recording station) sites.

This paper presents a methodology for the modification of ground motion recordings from ground surface stations to be representative of conditions at some target depth and an example of its implementation in an open-access webtool. The ultimate goal of this work is to broaden the utilization of data from the Center for Engineering Strong Motion Data (CESMD) and ground surface stations in general. Specific results are expected to provide: (1) a robust yet practical methodology for the development of at-depth input ground motions based on ground surface recordings, and (2) a user-friendly web-based tool accompanied by a user guide and example applications.

Approaches for developing input ground motions

Deconvolution analysis (Schnabel et al. 1972, Kramer 1996) is commonly used in engineering practice and research for the development of ground motions at depth based on a ground motion recorded at the ground surface (e.g., Mejia and Dawson 2006, Chiaradonna et al. 2018). It is a practical technique; however, it is also highly sensitive to the analysis input parameters such as the V_S profile (Cadet et al. 2011) and may run into numerical instabilities that impact the accuracy of the resulting ground motions (e.g., Roesset et al. 1995, Di Giulio et al. 2014). Common practices for preventing numerical issues when using deconvolution analysis include (1) scaling down the ground motion amplitudes such that only the ground motion fraction that can be explained by vertical propagation of waves is used (e.g., Silva 1988); (2) post-filtering of ground motions to remove any unreasonably high-frequency content (e.g., Silva 1988, Markham et al. 2015), and (3) using strain ratios and number of iterations different than the values traditionally used in equivalent linear SRAs (Bartlett et al. 2005). These approaches are either not implemented in most commercial programs or are developed based on observations specific to a single site and are thus of little use to the practicing engineer. In addition, oftentimes

the site and depth of interest are not the seismic station and the sensor depth, but rather a neighboring location. Thus, a subsequent convolution analysis accompanied by scaling or other procedures may be required to adapt the deconvolved ground motion to the target location. Cabas and Rodriguez-Marek (2017) as well as Nritsos et al. (2021) have presented other approaches for dealing with this issue.

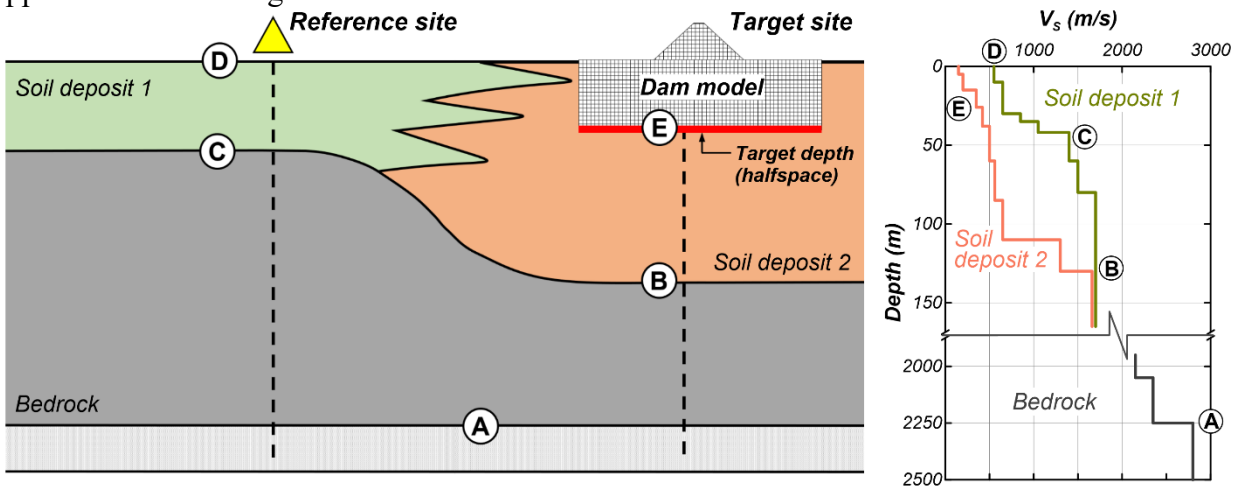

Figure 1. Schematic of a typical scenario where input ground motions for site response analyses (SRAs) or nonlinear deformation analyses (NDAs) at a target site can be developed based on a ground motion recorded at a reference site (seismic station).

Double convolution methodology for the development of input ground motions

The double convolution methodology allows for the development of ground motion recordings at a target site and depth (consistent with the conditions there) based on recordings from a ground surface station. Figure 1 shows a schematic of a project site with a neighboring seismic station where the approach can be used for the modification of ground motion recordings. In this schematic, input ground motions are developed for NDAs at the halfspace, location "E" at the "*target site*," based on ground motion recordings from a neighboring top-of-soil station, location "D" at the "*reference site*." Three additional locations need to be defined in Figure 1. Assuming that the target and the reference sites are sufficiently close, the geological conditions at these sites should become increasingly similar with depth, such that there are two locations, "B" and "C," on a common geological horizon (see later Figure 3). Ongoing research is investigating several scenarios such that the range of acceptable closeness or distance between the reference and target sites can be determined. Thus, an earthquake generated at a deeper location should cause the same upgoing wavefield from an arbitrary location "A" to "B" and to "C." In fact, the Vs profiles at the reference and target sites can stop at the depth corresponding to "B," but herein a deeper location ("A") is considered for simplicity in computing the profiles. Based on this reasoning and assuming that 1D wave propagation holds for kilometer-deep applications, random vibration theory (RVT)-based 1D SRAs (Hanks and McGuire, 1981; Boore, 2003; Rathje et al., 2005) can be conducted assuming an input motion at "A" to estimate the ground motions at "B," "C," "D," and "E." Then, the input ground motion at "E" can be estimated as:

$$\mathrm{FAS}_{\mathrm{E}}^{\mathrm{target}} = \frac{\mathrm{FAS}_{\mathrm{C}}}{\mathrm{FAS}_{\mathrm{D}}} \cdot \frac{\mathrm{FAS}_{\mathrm{E}}}{\mathrm{FAS}_{\mathrm{B}}} \cdot \mathrm{FAS}_{\mathrm{D}}^{\mathrm{rec}} \qquad (1)$$

where $\mathrm{FAS}_{\mathrm{E}}^{\mathrm{target}}$ is the Fourier amplitude spectrum (FAS) of the target input ground motion, $\mathrm{FAS}_{\mathrm{D}}^{\mathrm{rec}}$ is the ground motion recorded at the reference station, and $\mathrm{FAS}_{\mathrm{C}}$, $\mathrm{FAS}_{\mathrm{D}}$, $\mathrm{FAS}_{\mathrm{E}}$, and $\mathrm{FAS}_{\mathrm{B}}$ are computed using SRAs given an assumed input ground motion, $\mathrm{FAS}_{\mathrm{A}}$.For convenience, each ratio on the right-hand side of Equation (1) can be expressed as a TF:

$$\mathrm{FAS}_{\mathrm{E}}^{\mathrm{target}} = \mathrm{TF}_1 \cdot \mathrm{TF}_2 \cdot \mathrm{FAS}_{\mathrm{D}}^{\mathrm{rec}} \qquad (2)$$

where TF_1 modifies the ground motion recording at "D" to be compatible with the stiffer horizon at "C," and TF2 propagates the ground motion from "B" (equivalent to "C") to "E." With TF_1 and TF_2 calculated, then the ground motion at location "E" is estimated by taking the inverse Fast Fourier Transform (iFFT) of $\mathrm{FAS}_{\mathrm{E}}$. Figure 2 illustrates a flow diagram for the double convolution methodology.

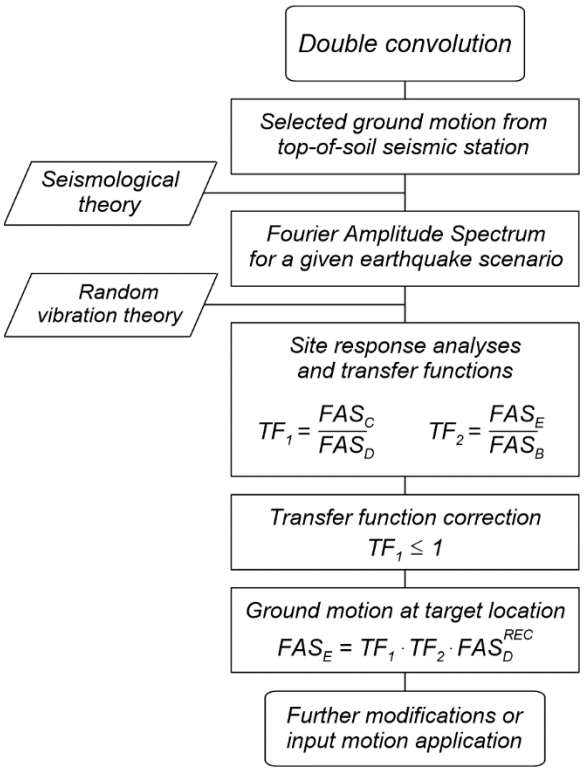

Figure 2. Methodology for the development of input ground motions for site response and nonlinear deformation analyses. Adapted from Pretell et al. (2019).

The input motion at "A" is defined using seismological models (e.g., Brune 1970, 1971; Boore, 2003), finite fault simulations (e.g., Beresnev and Atkinson, 1998), or any other method, and different attention is required depending on the application. In the case of modifying weak ground motions that do not yield any level of soil nonlinearity, any input ground motion can be used if linear elastic 1D SRAs are conducted for the double convolution approach. In the case of modifying strong ground motions that lead to a moderate level of soil nonlinearity (i.e., shear strains lower than 0.1% based on Kaklamanos et al., 2013), then the input motion should be defined based on the characteristics of the specific recording's earthquake event (e.g., magnitude and distance) and calibrated to yield a FAS at "D" that is like the recorded ground motion. The

accuracy in the input ground motion allows to properly capture any softening that the soil underwent during the earthquake. RVT is recommended herein as it does not require time histories and thus ease the input motion definition at "A."

Simplifications and extensions of the double convolution approach can be included depending on specific needs and site conditions. In cases where the ground motion recordings are needed at some depth at the reference site (i.e., from "D" to "C" in Figure 1), then $TF_2 = 1$. In cases where input ground motions are needed for forensic analyses and the target and reference stations are relatively far apart (with this still being under investigation), then the resulting ground motion can be further modified to account for differences in path effects (e.g., Chiaradonna et al., 2018; Ntritsos et al., 2021). Similarly, in cases where the input ground motions are required for engineering design, then the ground motions resulting from double convolution can be further modified to match a design spectrum (e.g., Hancock et al., 2006; Watson-Lamprey and Abrahamson, 2006; Baker et al., 2011; Kalkan and Chopra, 2010; Kwong and Chopra, 2015; Arteta and Abrahamson, 2019; Mazzoni et al., 2020), or to generate a suite of incoherent ground motions (Abrahamson, 1992b, 1993; Zerva, 2009) for the analysis of geographically distributed geosystems.

The double convolution methodology is different from previously proposed approaches. This methodology provides (1) a robust and practical technique for the modification of ground surface recordings to make them compatible with conditions at some target site and depth; (2) the ability to account for moderate soil nonlinearities such as those handled by equivalent linear SRAs, i.e., maximum shear strains lower than 0.1% (Kaklamanos et al. 2013); and (3) the potential for efficient propagation of uncertainties. The double convolution approach uses deep V_S profiles to account for site effects within high-V_S materials, which are typically considered negligible and might lead to underestimation of the seismic response (Steidl et al. 1996). The interested reader is directed to Pretell et al. (2021) for more information on the deep V_s profiles and some of the challenges involved in the process. The proposed methodology uses 1D linear elastic or equivalent linear SRAs along with RVT, and thus carries the same limitations as these tools, e.g., omission of ground motion lengthening effects and changes in ground motion phase due to wave propagation.

Web-based application tool

An open-access web application tool is being developed to make the double convolution methodology accessible and usable by the broader community of practicing engineers and researchers. This tool will facilitate the generation of input motions for SRAs, NDAs, and similar applications. The web tool provides a user-friendly and intuitive graphical user interface (GUI) for taking the input parameters of the model: reference and target site profile characteristics, target depths for the development of input ground motions, and the recorded earthquake motion at the ground surface. These input data are then synthesized to generate time histories of accelerations that can be used as input ground motions for SRAs, NDAs, and other similar applications. The web tool is developed using React (Facebook Inc. 2021), Flask (Pallets Projects 2021), and pystrata (Kottke et al. 2022). Figure 3 shows the web application architecture and request-response cycle. React is used to build the front end, i.e., the application's user interface (UI). Flask is used to build the back-end server to receive, send, and process the requests made by the user. Finally, any analysis involved in the double convolution methodology is performed in the back end using python and the pystrata implementation (Kottke 2019). The

web tool will be made available online and accessible to the public. In addition, a user manual with analysis guidelines and example applications will be provided to assist the users in using the tool. Its capabilities and intuitive and user-friendly GUI are expected to be of valuable use to the geotechnical engineering practice and academia in providing a practical yet robust approach for developing ground motions. Figure 4 illustrates the interface of the web application tool with the tabs "Reference Site," "Target Site," "Ground Motion," "Analysis Parameters" for receiving input parameters, and the "Results" tab for showing the synthesized input ground motions after performing the double convolution analysis.

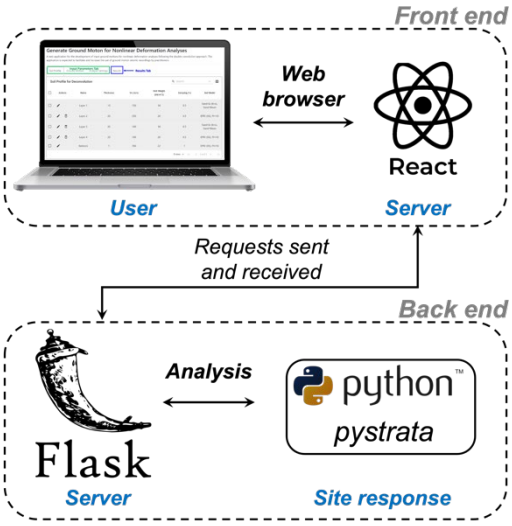

Figure 3. Web application tool architecture and request response-cycle.

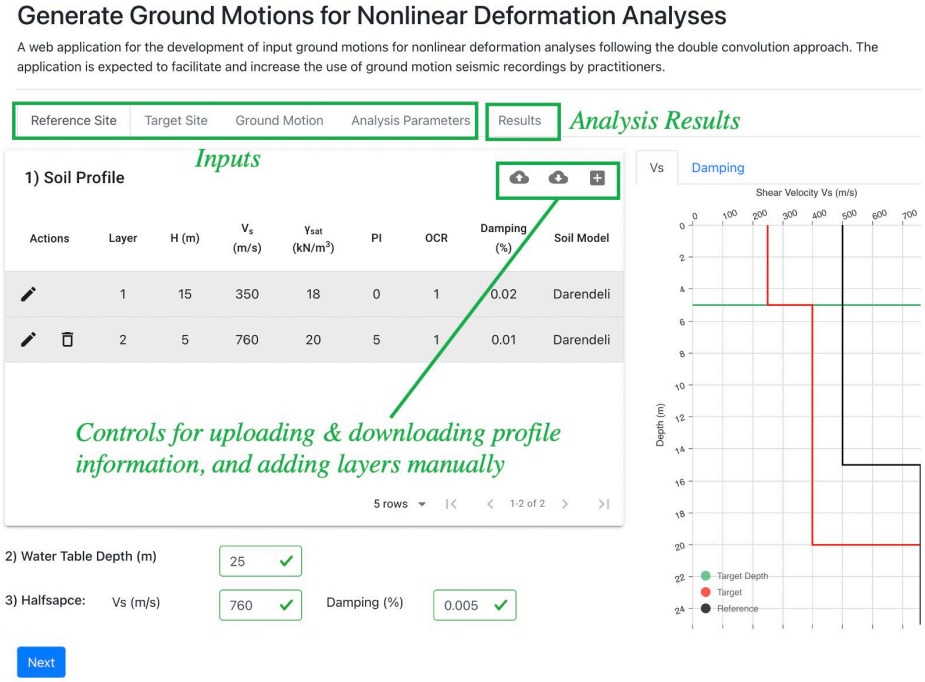

Figure 4. Web application interface for inputting reference and target soil profile

Features and Simple Example

Some currently implemented features of the webtool are:

1) Interactive plots of shear wave velocity and damping profiles for target and reference site.
2) Performs both linear elastic and equivalent linear analyses. These options are available under the "*Analysis Parameters*" tab. (Figure 7)
3) Ability to download and upload the soil profile data for reference and target site (see annotations of Figure 4).
4) The Fourier Amplitude Spectrum (FAS) of the ground motion can be generated from the Earthquake-Source model or can be provided as a separate file under the "*Ground Motion*" tab (Figure 5).
5) Results from the 1-D site response analysis include plots of (a) Transfer Functions and (b) maximum shear strain profiles (Figure 8).
6) For generating input motions from the obtained transfer functions: the user can either select a suite of motions (provided in the tool) or upload their own motion file. Results from the motion analysis include: (a) time-history, (b) Fourier Amplitude, and (c) Response spectrum plots. (Figure 9)
7) Tooltips (graphical user interface elements in which, when hovering over a screen element or component, a text box displays information about that element) are also currently being implemented at multiple locations of the tool in order to assist users more efficiently.
8) Allows downloading of the generated input motion from the analysis. The user can again choose another ground motion and correspondingly generate the input motion for the NDA analysis. (Figure 9)

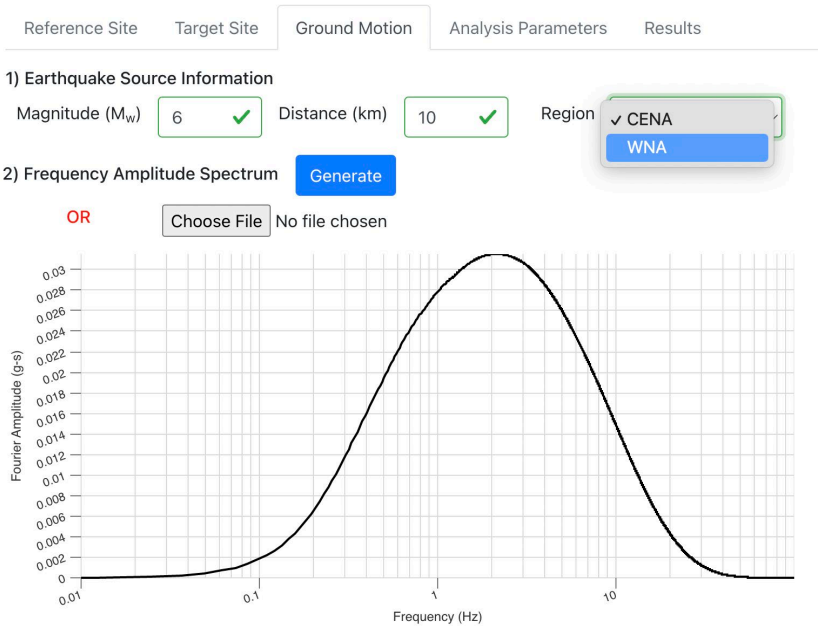

Figure 5. Options for specifying input motion.

Figure 5 illustrates a simple scenario to demonstrate how the web tool may be used. For simplicity Point A is considered the common horizon of upward traveling waves. Here, the goal

is to find the motion at point C (target site) subject to knowing the motion at point B (top-of-soil recording at reference site). All shear wave velocities are considered uniform.

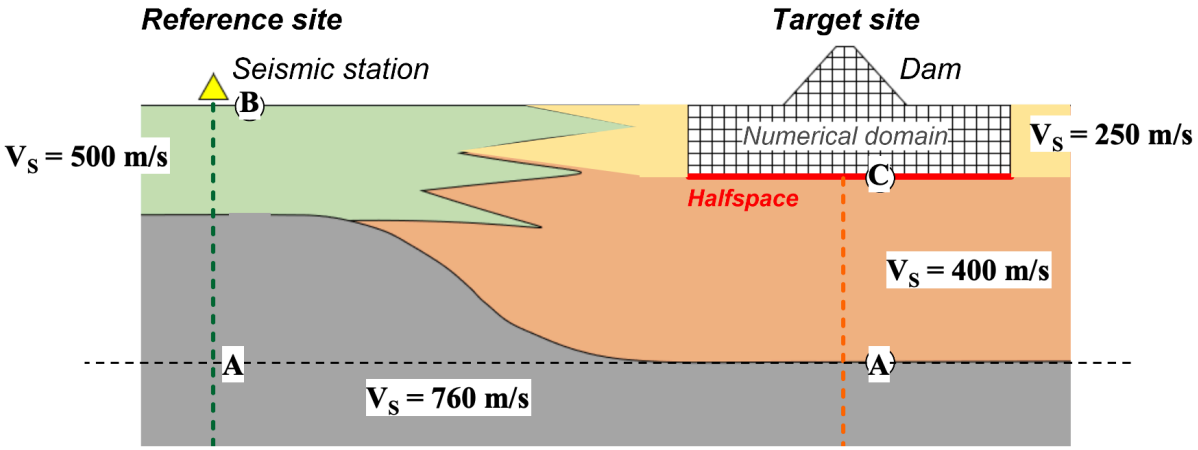

Figure 6. Example profile. The points are renamed relative to Figure 1 and the common deep horizon is at A considering that the target site is not very deep.

The model is generated by tabbing through the available menus starting from specifying the two sites and the depth of interest at the target site. Options include specifying the depth of the water table (assuming constant across) and the stiffness of the halfspace in terms of shear wave velocity. Figure 5 illustrates the options for specifying the Motion at Point B. Figure 7 shows the available options under the "Analysis Parameters" tab for the Equivalent Linear method. Once the user enters those, the analysis automatically commences. When done, results are automatically presented under the Results tab (Figures 8 and 9). The user has the option of downloading the developed motion. An planned addition is to add the ability to run multiple scenarios so uncertainties can be tracked.

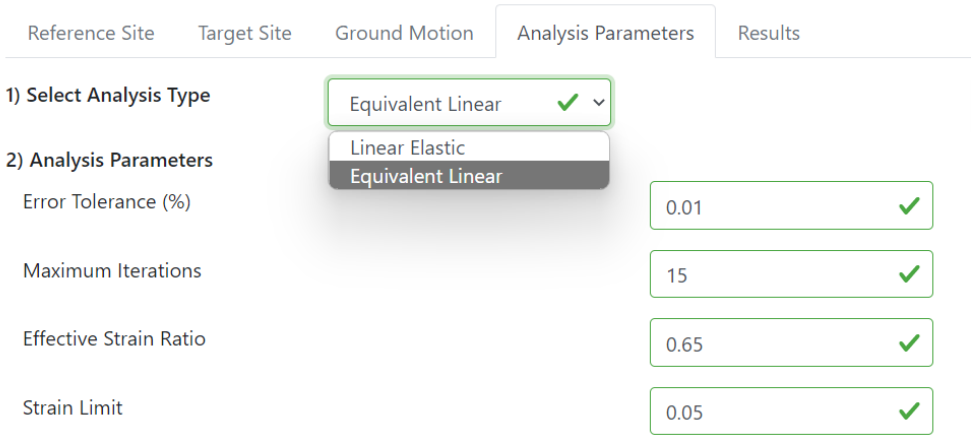

Figure 7. Web application interface for specifying analysis parameters.

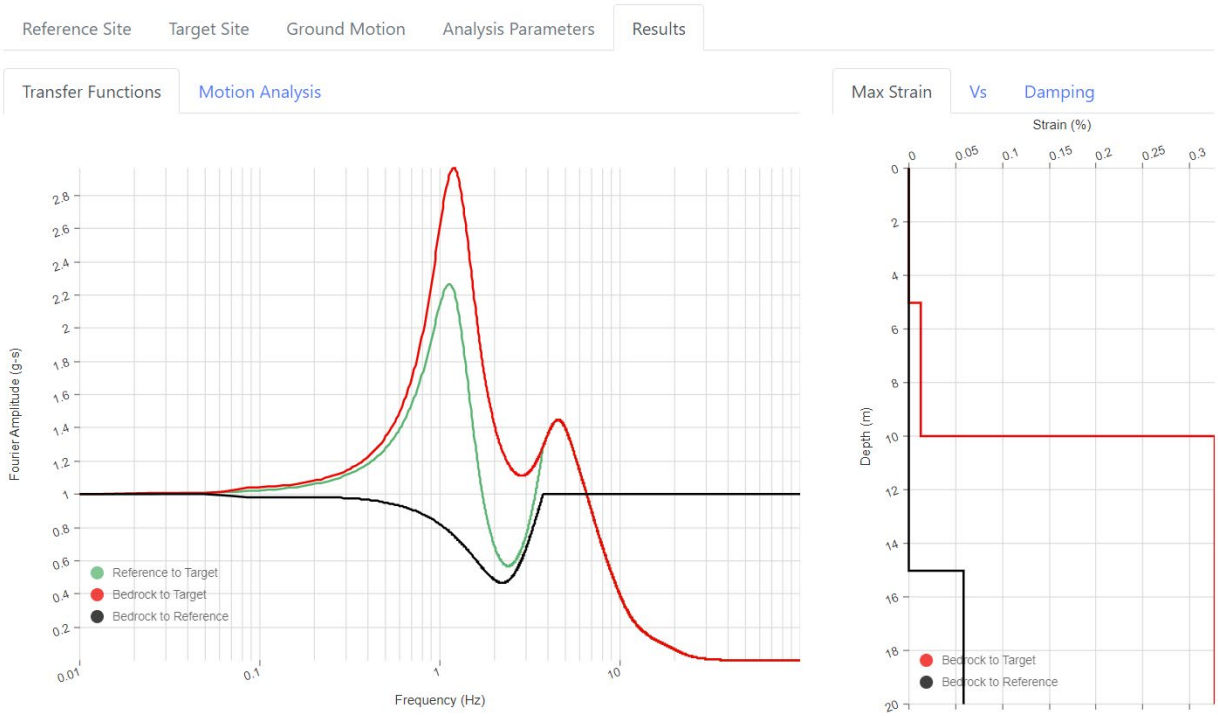

Figure 8. Results on transfer functions (see earlier descriptions) between the different locations of interest and the maximum shear strain profiles obtained from the site-response analysis

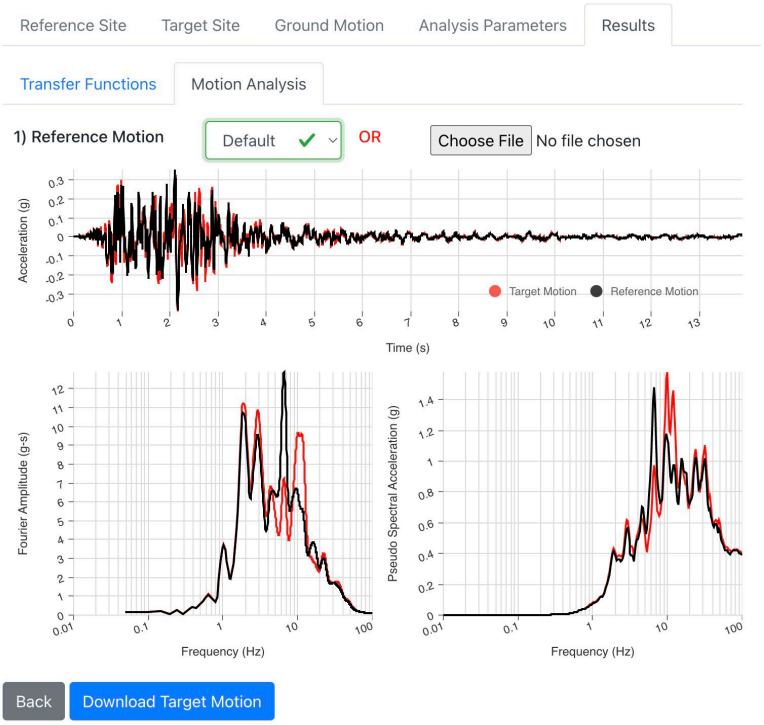

Figure 9. Motion analysis under Results. Results are presented in terms of accelerations time history, Fourier Amplitude Spectra, and Pseudospectral Accelerations.

Final Remarks

This paper briefly presented the double convolution methodology for the development of input ground motions primarily for the performance of site response analyses (SRAs) and nonlinear deformation analyses (NDAs) towards the design of structures or the forensic investigation of case histories. The double convolution methodology utilizes ground surface recordings, which dominate most seismic networks in the world. Advantages of the double convolution methodology as compared to commonly used and previously proposed approaches are: (1) its robustness in computing ground motions at a target depth based on ground surface recordings, (2) its implementation in a user-friendly interface to eventually facilitate the use of the proposed methodology in engineering practice and research, (3) the ability to account for moderate soil nonlinearities, and (4) the potential for efficient propagation of uncertainties.

The double convolution methodology addresses a problem of practical importance. Expected outcomes of this investigation include: (1) a robust yet practical methodology for the development of input ground motions, and (2) a user-friendly web-based tool accompanied by a user guide and example applications. The paper presented the webtool interface that is currently under development and a workflow alongside with the results it yields.

Acknowledgements

Discussions with Prof. Norman A. Abrahamson and Prof. Ellen M. Rathje were critical in the development of the proposed approach. Dr. Christine Goulet provided clarifications on the SCEC velocity models. Drs. Mei-Hui Su and Philip Maechling provided helpful assistance in the use of the UCVM software. The authors are grateful for all of the above assistance and feedback.

References

Abrahamson, N.A. (1992a). “Non-stationary spectral matching.” *Seism. Res. Lett.* 63:1, 30.

Abrahamson, N.A. (1992b). “Generation of spatially incoherent strong motion time histories.” *10th World Conference on Earthquake Engineering*, II:845–850.

American Society of Civil Engineers, ASCE (2016) Minimum design loads for buildings and other structures.

Arteta, C.A., and Abrahamson N.A. (2019). “Conditional Scenario Spectra (CSS) for hazard-consistent analysis of engineering systems.” *Earthquake Spectra*, 35(2): 737–757.

Baker, J.W., Lin, T., Shahi, S.K., and Jayaram, N. (2011). New Ground Motion Selection Procedures and Selected Motions for the PEER Transportation Research Program. PEER 2011/03.

Bartlett, S.F., Ostadan, F., and Abghari, C.F. (2005). “Development of design spectra for deep and soft soil sites.”

Beresnev, I.A., and Atkinson, G.M. (1998). "FINSIM: A FORTRAN program for simulating stochastic acceleration time histories from finite faults." *Seismological Research Letters*, 69, 27–32.

Boore, D.M. (2003). SMSIM - Fortran Programs for Simulating Ground Motions from Earthquakes: Version 2.0 - A Revision of OFR 96-80-A. A modified ver. of OFR 00-509, USGS.

Brune, J.N. (1970). "Tectonic stress and the spectra of seismic shear waves from earthquake." *Journal of Geophysics Research*, 75(26):4997–5009.

Brune, J.N. (1971). Correction. Journal of Geophysics Research, 76:5002.

Cabas, A., and Rodriguez-Marek, A. (2017). "V_S-κ_0 correction factors for input ground motions used in seismic site response analyses." *Earthquake Spectra*, 33(3): 917-941.

Cadet, H, Bard, P.-Y., and Rodriguez-Marek, A. (2011). "Site effect assessment using KiK-net data: Part 1. A simple correction procedure for surface/downhole spectral ratios." *Bulletin of Earthquake Engineering*, 10: 421-448.

Chiaradonna, A., Tropeano, G., d'Onofrio, A., and Silvestri, F. (2018). "Interpreting the deformation phenomena of a levee damaged during the 2012 Emilia Earthquake." *Soil Dynamics and Earthquake Engineering*,124: 389-398.

Di Giulio, G., Gaudiosi, I., Cara, F., Milana, G., and Tallini, M. (2014). "Shear-wave velocity profile and seismic input derived from ambient vibration array measurements: the case study of downtown L'Aquila." *Geophysical Journal International,* 198: 848-866.

Ely, G.P., Jordan, T.H., Small, P., and Maechling, P.J. (2010). "A V_{S30}-derived near surface seismic velocity model." AGU Fall Meet., San Francisco, California, 13–17 December, Abstract.

Facebook Inc. (2021). React - a JavaScript library for building user interfaces. v17.0.2.

Hancock, J., Watson-Lamprey, J., Abrahamson, N.A., Bommer, J., Markatis, A., McCoyh, E., and Mendis, R. (2006). "An improved method of matching response spectra of recorded earthquake ground motion using wavelets." *Journal of Earthquake Engineering*, 10(S1): 67–89.

Idriss, I.M. (2011) "Use of V_{S30} to represent local site conditions." *4th IASPEI/IAEE international symposium. Effects of source geology on seismic motion.*

Kaklamanos, J., Bradley, B.A., Thompson, E.M., and Baise, L.G. (2013) "Critical parameters affecting bias and variability in site-response analyses using KiK-net downhole array data." *Bulleting of the Seismological Society of America*, 103: 1733-1749.

Kottke, A.R. Millen, M., and Bot, S. (20229). pystrata, a module for conducting site response analysis. v0.5.1. https://zenodo.org/record/7105778

Kramer, S.L. (1996). Geotechnical Earthquake Engineering. Upper Saddle River: Prentice Hall.

Markham, C.S., Bray, J.D., and Macedo, J. (2015). "Deconvolution of surface motions from the Canterbury earthquake sequence for use in nonlinear effective stress site response analyses." *6th Int. Conf. on Earthquake Geotechnical Engineering*, Christchurch, New Zealand.

Mazzoni, S., Gregor, N., Al Atik, L., Bozorgnia, Y., Welch, D.P., and Deierlein, G.G. (2020). Probabilistic seismic hazard analysis and selecting and scaling of ground-motion records. PEER 2020/14.

Mejia, L.H., and Dawson, E.W. (2006). "Earthquake deconvolution for FLAC." *4th International FLAC Symposium*, Madrid, Spain.

Ntritsos, N., Cubrinovski, M., and Bradley, B.A. (2021). "Challenges in the definition of input motions for forensic ground-response analysis in the near-source region." *Eq. Spectra*.

Pallets Projects (2021). Flask – web development, one drop at a time. v2.0.1.

Pretell, R., Ziotopoulou, K., and Abrahamson, N. (2019). "Methodology for the development of input motions for nonlinear deformation analyses." *7th International Conference on Earthquake Geotechnical Engineering*, Rome, Italy.

Pretell, R., Ziotopoulou, K., and Davis, C.A. (2021). "Liquefaction and cyclic softening at Balboa Blvd. during the Northridge 1994 Earthquake." *Journal of Geotechnical and Geoenvironmental Engineering*, 147(2): 05020014.

Roesset, J.M., Huerta, C.I., Stokoe II, K.H. (1995). "Effect of magnitude and type of damping on soil amplification." *3rd International Conference on Recent Advances in Geotechnical Earthquake Engineering and Soil Dynamics*, Paper No. 10.25. St. Louis, MO.

Schnabel, P.B., Lysmer, J., and Seed, H.B. (1972). SHAKE: A Computer Program for Earthquake Response Analysis of Horizontally Layered Sites, Report UCB/EERC-72/12, Earthquake Engineering Research Center, University of California, Berkeley, CA.

Silva, W.J. (1988). Soil response to earthquake ground motion. EPRI Report NP-5747, CA.

Steidl, J.H., Tumarkin, A.G., and Archuleta, R.J. (1996). "What is a reference site?" *Bulletin Seismological Society of America*, 86: 1733-1748.

Watson-Lamprey, J.A. and Abrahamson, N.A. (2006). "Selection of ground motion time series and limits on scaling." *Soil Dynamics and Earthquake Engineering*, 26(5) 477-482.

MEASUREMENT AND IDENTIFICATION PROTOCOLS FOR HORIZONTAL-TO-VERTICAL SPECTRAL RATIO PEAKS

Pengfei Wang, Paolo Zimmaro, Sean K. Ahdi, Alan Yong, Jonathan P. Stewart

PW/JPS: UCLA Samueli Engineering
PZ: University of Calabria, Italy
SKA/AY: USGS

Abstract[1]

Peaks in horizontal-to-vertical spectral ratios (HVSR) of Fourier amplitudes from three-component recordings are used to identify site resonances, which are an important component of site response. We address two topics: (1) how should HVSR peaks be identified; and (2) are there appreciable differences in HVSR derived by using different instruments recording microtremors and seismic strong ground motions? We propose to identify peaks by considering peak amplitudes relative to neighboring ordinates and peak width. The procedure incorporates a regression tree algorithm that can be tuned to conform with user preferences toward relatively "conservative" or "liberal" peak identification (producing relatively few or many sites with peaks, respectively). Recommended parameters for both cases are provided. We then investigate the consistency of microtremor-based HVSR (mHVSRs) derived from seismometers and accelerometers, which show a high rate of false negatives (missed peaks) from accelerometers. In contrast, mHVSRs derived from co-located temporary and permanent instruments (optimized to record teleseismic signals) have about 60–80% consistency, with no apparent bias in peak assessments between instrument types. This indicates that mHVSR from accelerometers is not reliable, but that mHVSR can be reliably obtained with similar levels of quality from temporary or permanent seismometers. Lastly, we compare seismometer-based HVSR from microtremor and earthquake sources (mHVSR versus eHVSRs). Results are consistent for 60–70% of sites (i.e., both either do, or do not, have significant peaks; and when peaks are present, they occur at similar frequencies, <20% change). For sites with an mHVSR peak, the false-positive rate is nearly 50%, whereas for sites without an mHVSR peak the false-negative rate is relatively low (about 20%). The false positive rate is sufficiently high that the use of eHVSR to derive site response models is likely too optimistic (overestimates model effectiveness); mHVSR is preferred for consistency with information available in forward applications.

[1] Wang, P, P Zimmaro, SK Ahdi, A Yong, JP Stewart (in review). Measurement and identification protocols for horizontal-to-vertical spectral ratio peaks, submitted to *Bulletin of the Seismological Society of America*.

ENHANCING ASCE-41 MODELING GUIDELINES AND ACCEPTANCE CRITERIA USING INSTRUMENTED REINFORCED CONCRETE SHEAR WALL BUILDINGS

Laura L. Hernández-Bassal and Sashi K. Kunnath

Department of Civil and Environmental Engineering
University of California, Davis

Abstract

A preliminary set of evaluations on a low-rise reinforced concrete shear wall building is presented with the goal of assessing the modeling guidelines and acceptance criteria in ASCE-41 (ASCE/SEI 41, 2017). First, the ability of available commercial and open-source software to simulate the nonlinear flexural and combined shear-flexural response of experimentally tested walls is investigated. Next, a commonly-used commercial software, Perform-3D (CSI 2021) is utilized to conduct an assessment of a 3-story shear-wall building wherein all four analysis methods specified in ASCE-41 are applied. The simulation model is validated against instrumented data obtained during the 2010 Maricopa earthquake prior to its use in the ASCE-41 assessments. Results of the different assessments indicate that linear procedures are highly conservative with Collapse Prevention limits being exceeded whereas the application of nonlinear procedures suggest that the building performance is within Life Safety limits.

Introduction

Beyond facilitating the seismic assessment of buildings, the guidelines in ASCE-41 (ASCE/SEI 41, 2017) also represent a significant advance in the practice of performance-based earthquake engineering. However, calibration of the analysis procedures and acceptance criteria to real building performance should be a continuing effort. The use of strong motion data obtained from instrumented buildings experiencing strong ground shaking is an essential part of this process.

However, many of the nonlinear modeling guidelines in ASCE-41 include unspecified parameters left to the judgement of the engineer – with the potential for considerable variation in the predicted seismic demands. Additionally, as pointed out in a recent research report (NEHRP Consultants Joint Venture, 2013), "ASCE/SEI 41 generalized force-deformation curves are presented with single, deterministic values, without any information on the uncertainty or reliability of the parameters." Another issue that arises from using ASCE-41 is the choice of the analysis procedure since as many as four are permitted to estimate seismic demands: Linear Static Procedure (LSP), Linear Dynamic Procedure (LDP), Nonlinear Static Procedure (NSP), and Nonlinear Dynamic Procedure (NDP). This implies that the assessment of a regular low to mid-rise building (that meets the criteria for the use of linear and/or static procedures) using any of the methods should result in the same conclusion on the likely performance of the building.

The aforementioned issues are being addressed in an ongoing project that focuses on modeling and acceptance criteria for shear-wall buildings. Shear wall buildings form an

important subset of RC buildings and are a common choice for buildings where deformation control is important. Since shear walls make up the primary (and generally the only) lateral force resisting system in a building, they are less redundant than moment-frame structures and damage or failure of a single wall can have more significant consequences on the performance of the structure.

Assessment of Existing Shear Wall Models

ASCE-41 does not provide specific guidelines on modeling a shear wall element. Many options exist for modeling a concrete wall: the simplest approach is to model the wall as a beam-column element with inelastic behavior lumped into a concentrated spring with aggregated shear; the next level of refinement would be a beam-column element with distributed properties where selected integration points are discretized into fibers representing cover concrete, core concrete and reinforcing steel. RC walls have also been modeled using multi-spring macro-models consisting of a set of springs distributed in a manner that captures the strain distribution across the section of the wall as well as the migration of the neutral axis under lateral cyclic loading. In order to understand the capabilities of the available 2D models in different software programs, two computational platforms were considered: OpenSees (McKenna, 2011) and Perform-3D (CSI 2021). Validation studies were carried out on two shear wall specimens. The first wall considered is specimen **RW2** (Fig. 1a), part of the set of walls tested by Thomsen and Wallace (1995). This is a relatively slender wall with a height to width ratio of 3.0, in which inelastic deformations are expected to be dominated by flexure, and subjected to a constant axial load of $0.07 f_c' A_g$ throughout the test. The second wall is specimen **RW-A15-P10-S78** (Fig. 1b), tested by Tran and Wallace (2012). This wall has a height to width ratio of 1.5 and nonlinear shear deformations are expected to contribute to the overall response. A constant axial load of $0.064 f_c' A_g$ was maintained at the top of the wall. Both wall elevations are shown in Fig. 1.

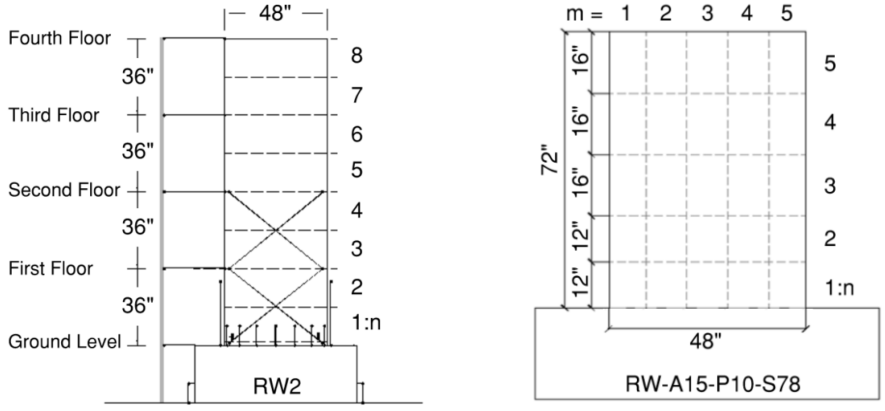

(a) (b)

Figure 1. Elevation of wall specimens: (a) Specimen 1 (Thomsen & Wallace 1995); (b) Specimen 2 (Tran & Wallace 2012)

The two walls were modeled in OpenSees using three different modeling options: a beam-column element with fiber-section discretization, the Multiple Vertical Line Element

Model (MVLEM), and the Cyclic Shear-Flexural Interaction Multiple Vertical Line Element (SFI-MVLEM). They were modeled in Perform-3D using the Shear Wall element with Inelastic section – for Specimen 1, an elastic shear material was used whereas an inelastic shear material was used for Specimen 2. Note that MVLEM and SFI-MVLEM are derivatives of the original element introduced by Japanese researchers (Kabeyasawa et al. 1983) and later enhanced by others (Orakcal et al. 2004; Massone et al. 2006; Kolozvari et al. 2015).

Fig. 2 compares the numerically simulated response for Specimen 1 versus the measured cyclic response for all four modeling choices. In general, all models produce a good match. Both the MVLEM and SFI-MVLEM models capture the initial stiffness well, whereas the beam-column with fiber-section and Perform-3D models slightly overestimate it though they do a better job in predicting the strength in each cycle. Since the material models in Perform-3D are multilinear, the resulting force-deformation response is also multilinear.

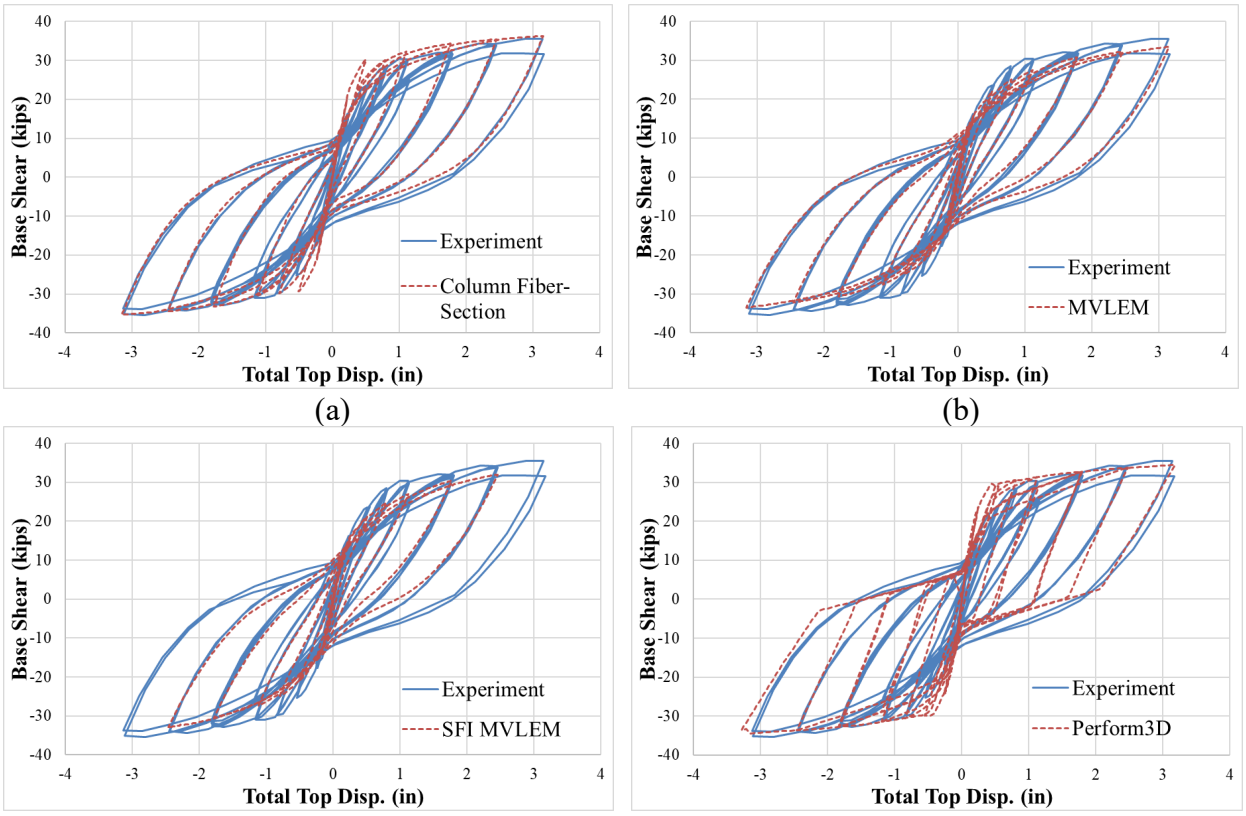

Figure 2. Validation of modeling approaches using results from Specimen 1: (a) OpenSees with beam-column element and fiber section; (b) OpenSees MVLEM; (c) OpenSees SFI-MVLEM; (d) Perform-3D

Fig. 3 shows the results for Specimen 2. It is evident that the SFI-MVLEM model produces the best results. The beam-column element with fiber-section (and aggregated shear spring) and the MVLEM model are unable to accurately capture the pinched response observed in the experiment. In Perform-3D, it is unclear as to how shear is coupled with flexure. The manual simply indicates that the shear wall is a "compound" element with either elastic or

inelastic shear material. Despite numerous attempts to tune the inelastic shear material properties, it was difficult to obtain a suitable response.

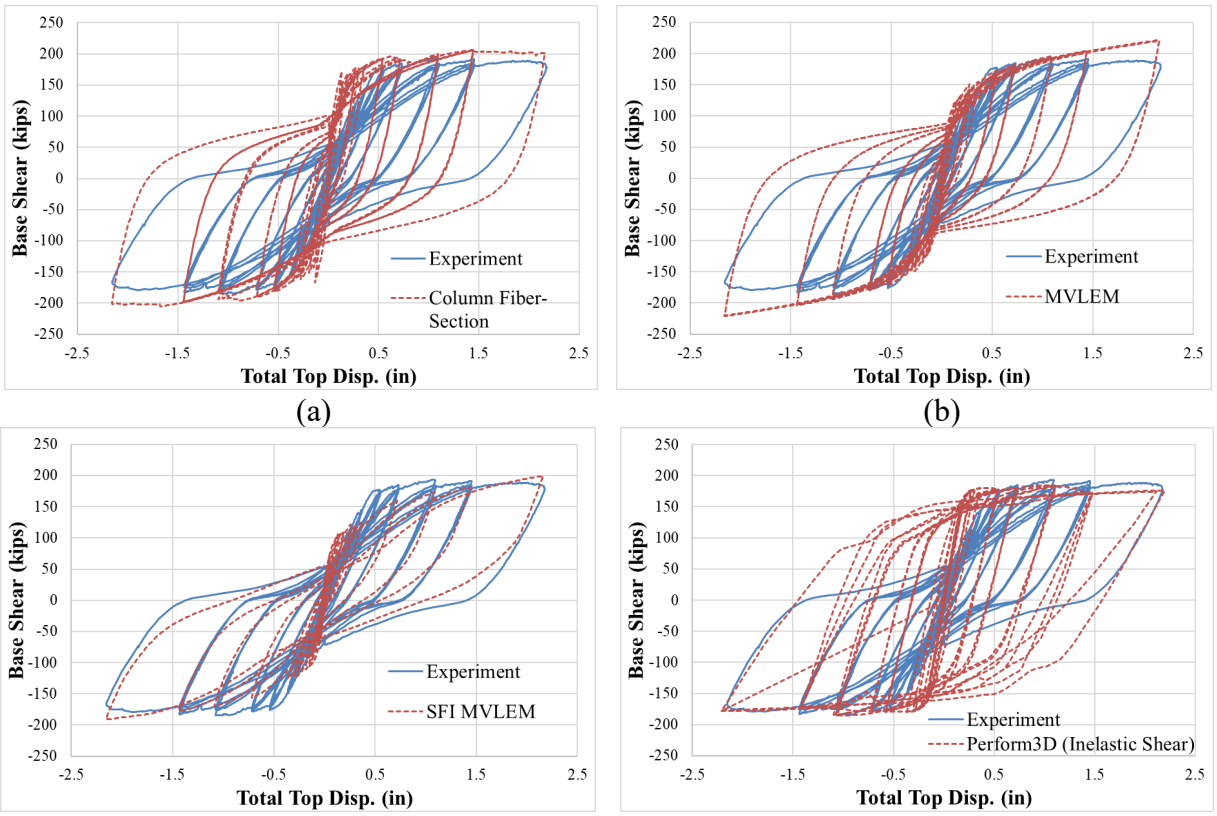

Figure 3. Validation of modeling approaches using results from Specimen 2: (a) OpenSees with beam-column element and fiber section; (b) OpenSees MVLEM; (c) OpenSees SFI-MVLEM; (d) Perform-3D

Building Assessment: Modeling and Validation

In order to realistically evaluate the issues outlined in the introduction, it is important to begin with realistic computer models of existing buildings. Hence calibrating the models to observed data is a critical aspect of the proposed evaluation – since the contribution of non-structural components is inherent in the measurements. The first structure selected for the assessment is a 3-story school building designed in 1948 and located in Taft, California. The gravity system is composed of reinforced concrete slabs, supported on pan joists, and beams, supported by walls and columns. The lateral force resisting system includes concrete slab diaphragms and shear walls. There are four principal L-shaped walls at the corners with embedded columns at the gridlines, and two additional rectangular walls in the longitudinal direction. The building wall framing conserves symmetry. Fig. 4 shows the typical floor plan of the building.

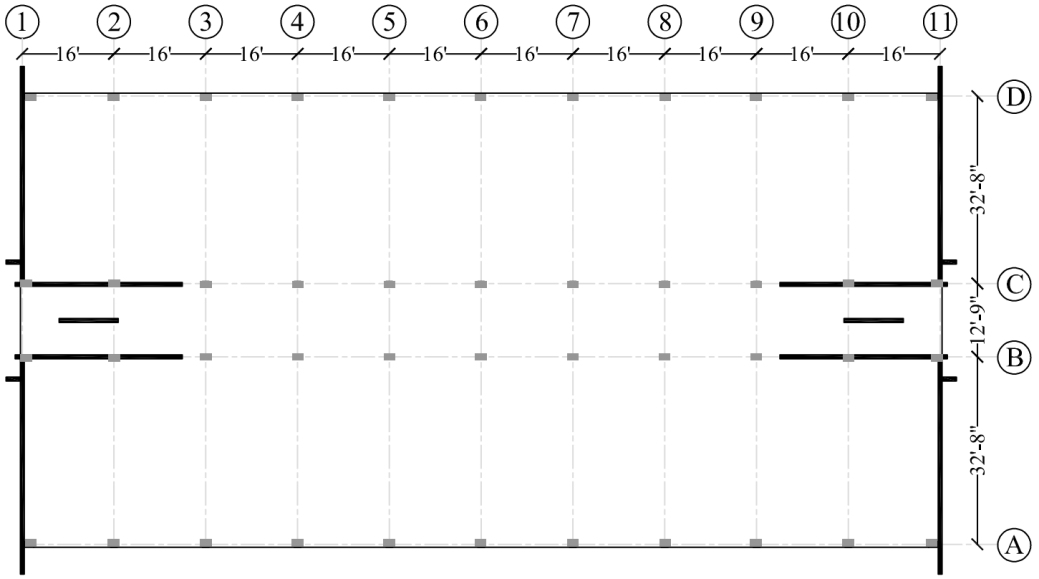

Figure 4. Plan view of building at typical floor

The building has been instrumented by the California Strong Motion Instrumentation Program (CSMIP Station 35409) with thirteen accelerometers: six at the ground level to record base accelerations in all three orthogonal directions, three at the 2nd floor, and four at the roof of the building – as shown in Fig. 5. There are a total of six recorded earthquakes measured at this site. However, only the 2010 Maricopa Earthquake sensor recordings will be used for the calibration since this is the earthquake with the largest ground peak acceleration.

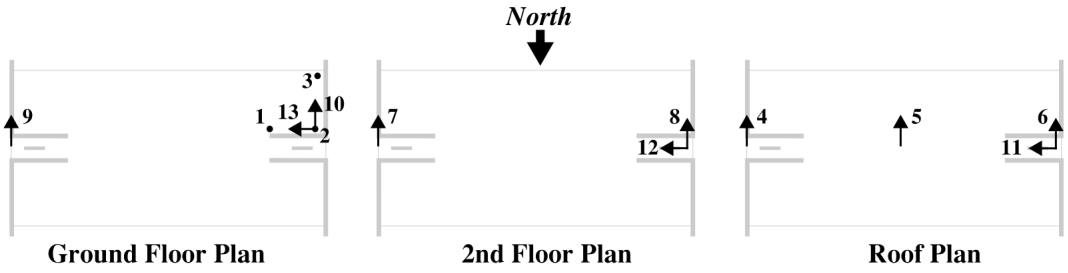

Figure 5. Locations of installed sensors

Modeling and Validation

Given that the main lateral load resisting system is composed of L-shaped walls, it was necessary to create a three-dimensional building model, in order to capture any potential torsional modes as well as to account for non-symmetric response following inelastic action. Therefore, the analyses were carried out using the commercial software Perform-3D (CSI 2021). Fig. 6 shows the 3D and transverse/longitudinal elevation views of the model.

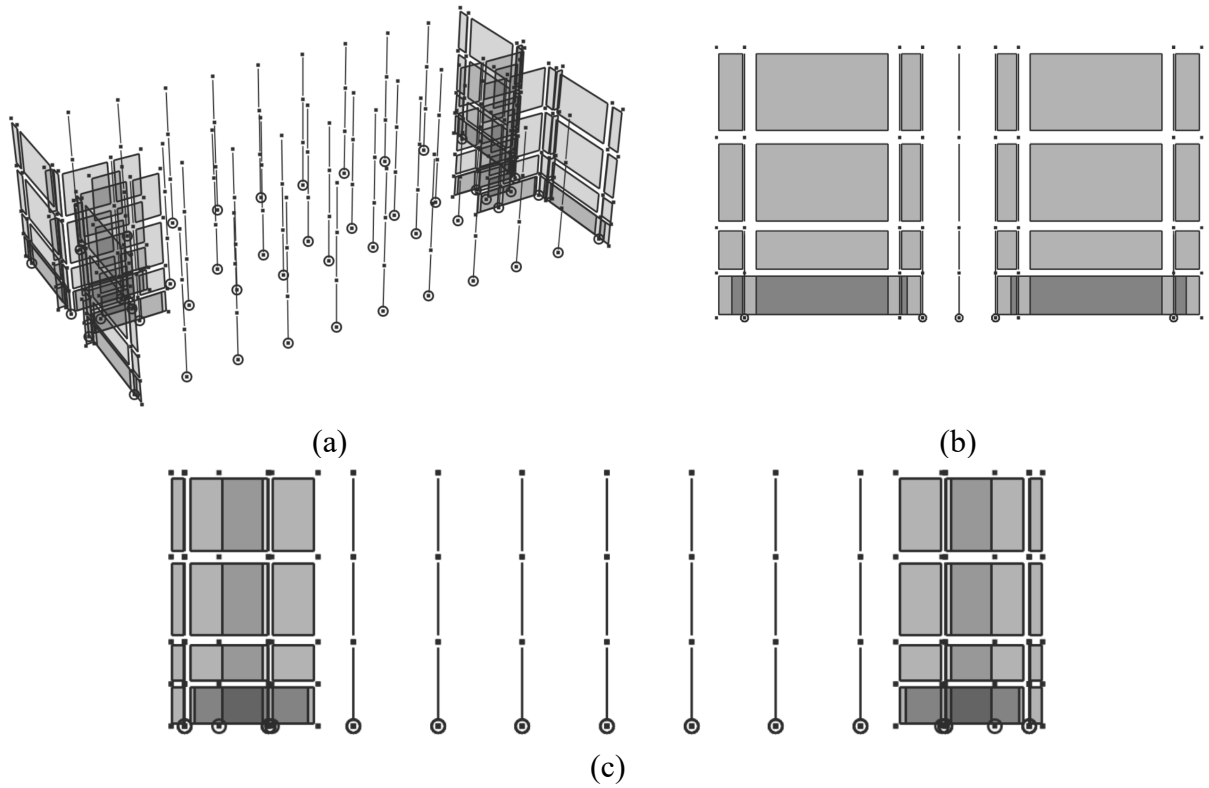

**Figure 6. Perform3D model: (a) 3D view,
(b) N-S elevation (transverse), (c) E-W elevation (longitudinal)**

The walls were modeled using the *Shear Wall, Inelastic Section*, and the columns using the *Column, Inelastic Fiber Section*. The wall elements at the first story were divided into two elements along the height, to ensure a proper hinge length for inelastic action, while the upper story walls were modeled at the full height for each element. The unconfined and confined concrete were modeled using the *Inelastic 1D Concrete Material*, and were assigned to the walls and columns respectively. The rebar was modeled using the *Inelastic Steel Material, Non-Buckling*. For both concrete and steel materials, strength loss was considered. The parameters used follow the stress-strain relationship shown in Fig. 7 and are listed in Table 1. Cyclic degradation for the three materials was specified with the following energy factors: 1, 0.4, 0.4, 0.1, 0.1 at points Y, U, L, R, and X respectively, as recommended by Lowes et. al (2016). The shear material was specified as elastic with a shear modulus equal to 0.4 times the elastic modulus.

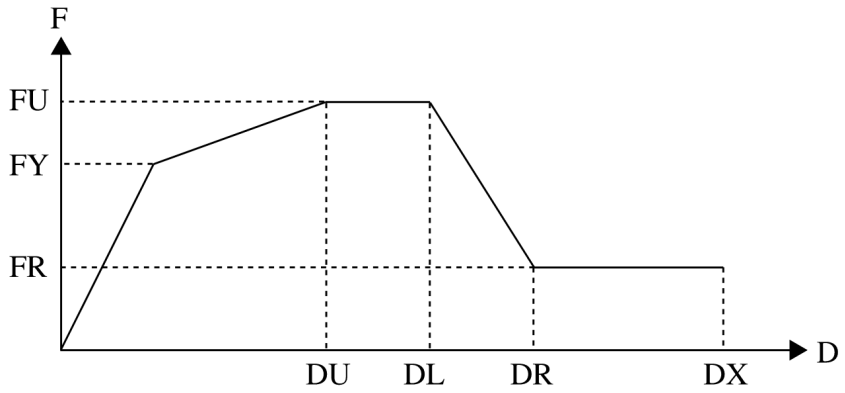

Figure 7. Perform-3D: Parameters for stress-strain relationships

Table 1. Stress-strain properties

Properties	Unconfined Concrete	Confined Concrete	Steel Rebar
E (ksi)	3491	3694	29000
FY (ksi)	2.25	2.52	41.25
FU (ksi)	3.75	4.2	51.5625
DU	0.0025	0.0035	0.045
DL	0.003	0.004	0.07
DR	0.01	0.035	0.1
DX	0.2	0.2	0.2
FR/FU	0.1	0.2	0.2

A diaphragm constraint was applied at each level. There are elastic springs at all base nodes which have a footing. The spring stiffness values were originally calculated and updated in the model; however, the analysis showed that the foundation was introducing too much flexibility to the system. Therefore large stiffness values were assigned to the springs, essentially creating a fixed base model, and better capturing the recorded response in the model. An eigenvalue analysis was carried out on the model and the first and second mode periods were estimated to be 0.194 sec and 0.143 sec in the longitudinal and transverse directions, respectively. A value of 7.5% of critical damping in the two modes were assigned. The structure was then subjected to the recorded base motion during the Maricopa earthquake. The corresponding ground motions recorded at sensors 13 and 10 were applied to the longitudinal and transverse directions, respectively. Fig. 8 compares the simulated and recorded roof response after final calibration of the model.

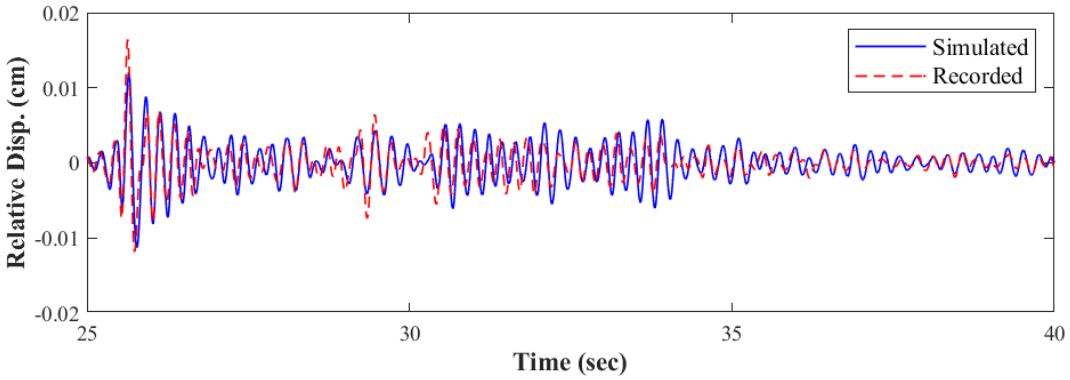

(a)

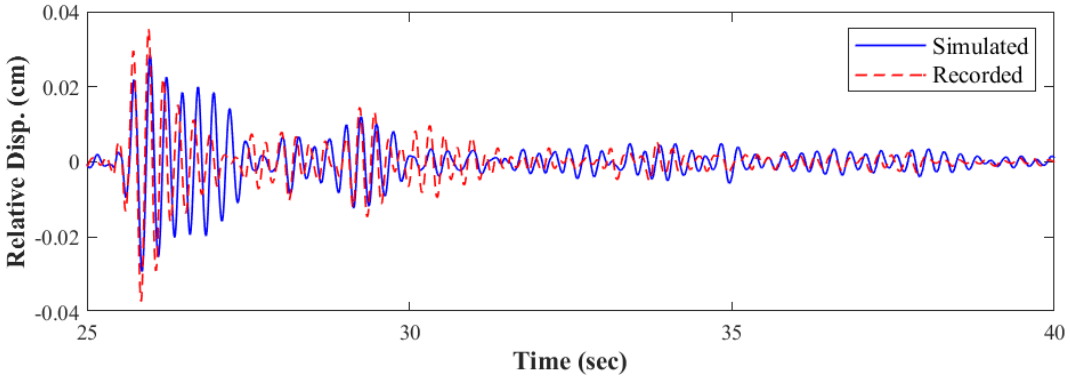

(b)

Figure 8. Comparison of recorded vs. simulated roof displacement histories during the Maricopa earthquake: (a) Transverse; (b) Longitudinal direction

Building Assessment using ASCE 41 Guidelines

A seismic performance assessment of the building was carried out by analyzing the validated computer model of the 3D building and using both linear and nonlinear analysis procedures prescribed in ASCE 41. Note that in all procedures described hereafter, the lateral load application is preceded by the application of the sustained gravity loads on the frame. The seismicity considered in the assessment is based on the BSE-2E hazard level, which represents a 5% probability of occurrence in 50 years. The resulting response spectrum for the site is shown in Fig. 9 with the following key parameters: S_{XS} = 1.23 g; S_{X1} = 0.873 g; T_O = 0.14 sec and T_S = 0.71 sec.

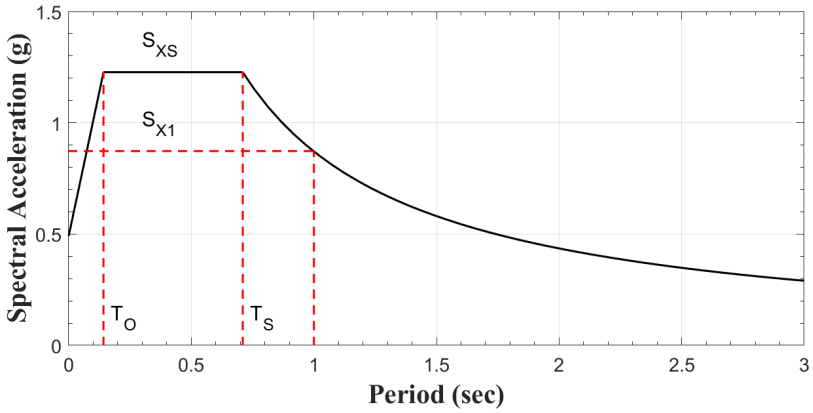

Figure 9. Response spectrum for site

Linear Procedures

For the linear procedures, linear elastic materials were specified in Perform-3D. For the Linear Static Procedure (LSP), an equivalent static load, representative of the seismic hazard, is applied over the height of the building, in each horizontal direction independently. The modification factors are C_1C_2= 1.0 and C_m = 0.8. The effective seismic weight is 5858 kips for the full building. For the Linear Dynamic Procedure (LDP), the assessment was completed by using the Response Spectrum load case type in Perform3D, ensuring that the modes considered captured at least 90% of the participating mass of building. For both linear procedures, the demands in the components were obtained by applying the 100%-30% and 30%-100% combination rule. The walls in the building have been identified in Fig. 10. The final results for the linear procedures are listed in Table 2, and visually presented in Fig. 11. The LSP and LDP results are consistent, with two walls complying with Life Safety (LS), two walls complying with Collapse Prevention (CP), and six walls exceeding CP.

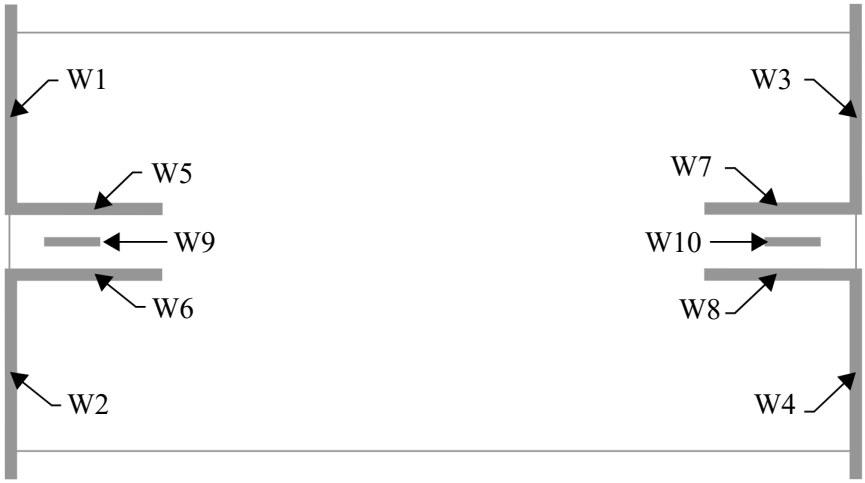

Figure 10. Plan view identifying wall elements

Table 2: LSP and LDP results

Wall #	Capacities	LSP Demands		LDP Demands		ASCE -41 m-Factors		
	V (k)	V (k)	DCR	V (k)	DCR	IO	LS	CP
W1	583	1411	2.4	1722	3.0	2	3	4
W2	229	1411	6.2	1722	7.5	2	3	4
W3	583	1411	2.4	1722	3.0	2	3	4
W4	229	1411	6.2	1722	7.5	2	3	4
W5	356	1229	3.5	1425	4.0	2	3	4
W6	356	1229	3.5	1425	4.0	2	3	4
W7	184	1229	6.7	1425	7.7	2	3	4
W8	184	1229	6.7	1425	7.7	2	3	4

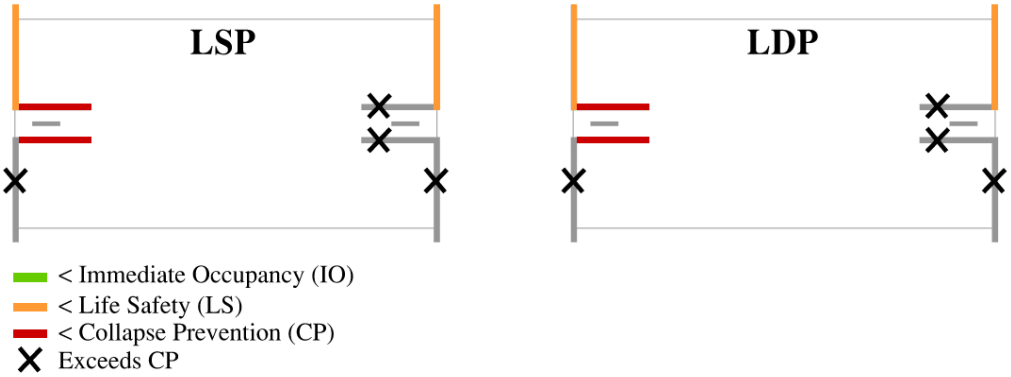

Figure 11. Results of LSP and LDP assessments

Nonlinear Procedures

For the nonlinear procedures, the original nonlinear model was used in the analyses. For the Nonlinear Static Procedure (NSP), the building was pushed to the computed target displacements of 7.16 in (0.0124 drift) and 4.10 in (0.0071 drift) in the longitudinal and transverse directions, respectively. The maximum demands obtained from the two analyses were used in the assessment of the building performance.

For the Nonlinear Dynamic Procedure (NDP), the site hazard was established using the United States Geological Survey (2018) Unified Hazard Tool, based on the site deaggregation. The seismic hazard at the site is controlled by the San Andreas fault. A total of 51 ground motions were downloaded from the PEER NGA ground motion database (ngawest2.berkeley.edu) with the following filters: fault type: strike slip; magnitude: 6 to 8; distance to rupture: 5 to 25; and shear wave velocity Vs30: 200 to 400 m/s, based on the controlling seismic hazard at the site. Ground motions with spectral shapes significantly different from the target spectrum were discarded. The final 11 sets of ground motion (pairs) were selected such that the average maximum direction spectra (RotD100) was at or above 90% of the target response spectrum in the period range 0.2T1 – 1.5T1. Even though the site is classified as near-fault, the horizontal components of each selected ground motion were not rotated to the

fault-normal and fault-parallel directions of the causative fault. Fig. 12 shows the selected records spectral accelerations, and Table 3 lists the details of the ground mtions.

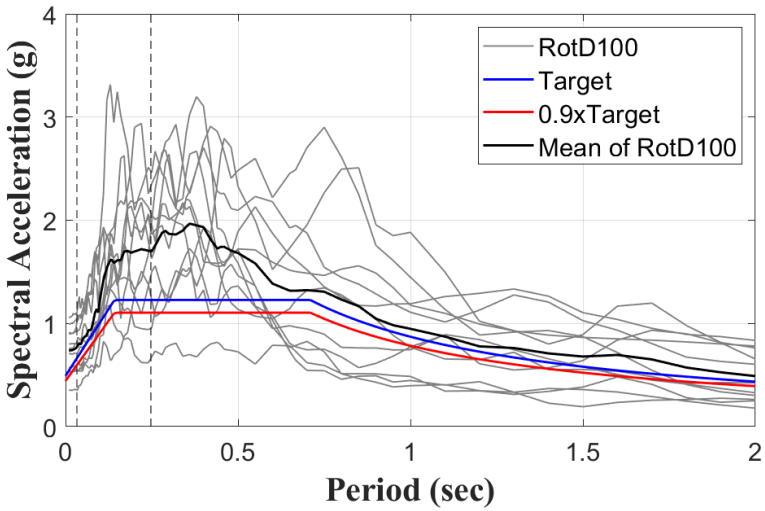

Figure 12. Maximum direction spectra of scaled motions, mean spectra, and site target spectrum

Table 3: Selected ground motions

GM #	Record Sequence Number	Earthquake Name	Year	Station Name	Magnitude	R_{rup} (km)
1	30	"Parkfield"	1966	"Cholame - Shandon Array #5"	6.19	9.58
2	162	"Imperial Valley-06"	1979	"Calexico Fire Station"	6.53	10.45
3	169	"Imperial Valley-06"	1979	"Delta"	6.53	22.03
4	179	"Imperial Valley-06"	1979	"El Centro Array #4"	6.53	7.05
5	184	"Imperial Valley-06"	1979	"El Centro Differential Array"	6.53	5.09
6	185	"Imperial Valley-06"	1979	"Holtville Post Office"	6.53	7.5
7	558	"Chalfant Valley-02"	1986	"Zack Brothers Ranch"	6.19	7.58
8	1101	"Kobe_ Japan"	1995	"Amagasaki"	6.9	11.34
9	1107	"Kobe_ Japan"	1995	"Kakogawa"	6.9	22.5
10	1158	"Kocaeli_ Turkey"	1999	"Duzce"	7.51	15.37
11	1605	"Duzce_ Turkey"	1999	"Duzce"	7.14	6.58

For each ground motion set, the horizontal components were applied concurrently to the model, and then again applied but with the directions switched. The maximum demands for each set were calculated and then used to compute the average demands of the eleven ground motion sets. Table 4 lists the results for both nonlinear procedures and Fig. 13 shows the performance level compliance. The results show that all walls satisfy the LS criteria for NSP, and the IO criteria for NDP. This is significantly different than the performance levels satisfied by the linear procedures.

Table 4: NSP and NDP results

Wall #	NSP Max Rotation	NDP Max Rotation	ASCE 41 Acceptable Plastic Hinge Rotation		
			IO	LS	CP
W1	0.0127	0.0020	0.0050	0.0150	0.0150
W2	0.0130	0.0021	0.0050	0.0150	0.0150
W3	0.0127	0.0017	0.0050	0.0150	0.0150
W4	0.0130	0.0016	0.0050	0.0150	0.0150
W5	0.0067	0.0029	0.0050	0.0150	0.0150
W6	0.0067	0.0029	0.0050	0.0150	0.0150
W7	0.0069	0.0029	0.0050	0.0150	0.0150
W8	0.0069	0.0029	0.0050	0.0150	0.0150

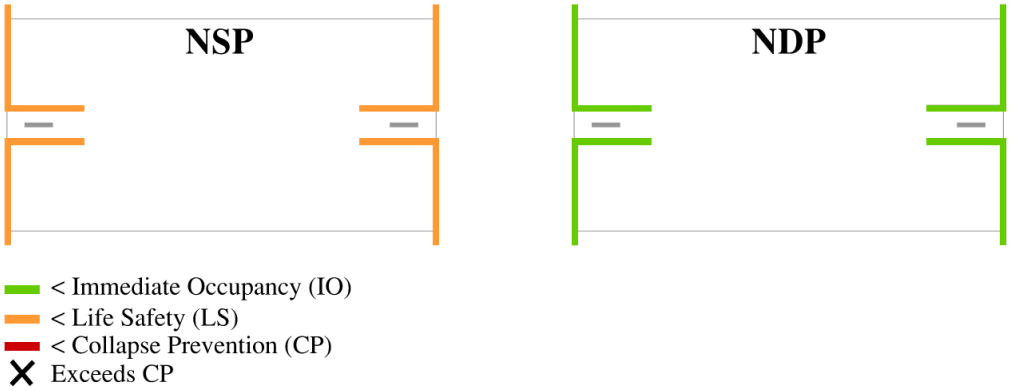

Figure 13. Results of the assessments using NSP and NDP

Conclusions

A comparative study of modeling approaches was completed for two reinforced concrete wall specimens. The walls were modeled using a total of four distinct modeling schemes in OpenSees and Perform3D. The results show that for the flexure-controlled specimen, the MVLEM and SFI-MVLEM models in OpenSees better captured the initial stiffness and the OpenSees beam-column with fiber-section and Perform-3D shear wall models better predicted the strength, albeit all models produced a reasonable match of the overall cyclic force-deformation response. In the shear-controlled specimen, the SFI-MVLEM produced the best results, capturing the stiffness, strength and pinched response under cyclic loading.

An existing three-story shear wall concrete building was selected for the ASCE-41 based assessment. Given the L-shaped walls in the building, it was decided to use Perform-3D for the assessment since SFI-MVLEM was considered more suitable for planar walls. Following calibration of the model to instrumented response from a recent earthquake, a preliminary ASCE-41 assessment was completed utilizing both linear and both nonlinear analysis procedures. The results show that LSP and LDP produced demands exceeding the acceptance

criteria for the CP performance level for as many as four walls. However, the NSP and NDP demands satisfied LS and IO, respectively, for all walls. This demonstrates inconsistency among the four analysis procedures and is the subject of additional ongoing investigation.

Acknowledgements

Funding for this study was provided by the California Department of Conservation, California Geological Survey (Strong Motion Instrumentation Program) under Agreement 1020-005. However, the contents of the paper do not necessarily represent the policy of that agency nor is an endorsement by the State Government of California.

References

ASCE/SEI (2017). Seismic Evaluation and Retrofit of Existing Buildings, ASCE/SEI 41-17, American Society of Civil Engineers, Reston, Virginia.

CSI (2021). Perform-3D: Performance-Based Design of 3D Structures. Computers and Structures Inc., Walnut Creek, CA.

Kabeyasawa, T., Shiohara, H., Otani, S. and Aoyama H. (1983). Analysis of the full-scale seven-story reinforced concrete test structure.J. Fac. Eng..University of Tokyo.XXXVII:2,432–78.

Kolozvari K., Orakcal K., and Wallace J. W. (2015). ”Modeling of Cyclic Shear-Flexure Interaction in Reinforced Concrete Structural Walls. I: Theory”, ASCE Journal of Structural Engineering, 141(5).

Lowes, L., Lehman D., and Baker, C. (2018). Recommendations for Modeling the Nonlinear Response of Slender Reinforced Concrete Walls Using PERFORM-3D, 2016 SEAOC Convention Proceedings, 2016.

Massone, L.M., Orakcal, K. and Wallace J.W. (2006). Shear–flexure interaction for structural walls.ACI special publication—Deformation capacity and shear strength of reinforced concrete members under cyclic loading. ACI-SP236-07, 127–150.

McKenna, F. (2011). OpenSees: a framework for earthquake engineering simulation. Computational Science & Engineering, 13 (4), 58-66. https://doi.org: 10.1109/ MCSE.2011.66

NEHRP Consultants Joint Venture (2013). “Nonlinear Analysis Research and Development Program for Performance-Based Seismic Engineering,” NIST GCR 14-917-27, National Institute of Standard and Technology, US Department of Commerce, Gaithersburg, MD.

Orakcal, K., Wallace, J.W., and Conte, J.P. (2004).Flexural modeling of reinforced concrete walls—model attributes.ACI Structural Journal.101:5,688–98.

Thomsen, J. H., IV, and Wallace, J. W. (1995) ‘‘Displacement-based design of reinforced concrete structural walls: Experimental studies of walls with rectangular and T-shaped cross sections.’’ Rep. No. CU/CEE-95/06, Department of Civil and Environmental Engineering, Clarkson University, Potsdam, NY.

Tran T.A. and Wallace J.W. (2012). Experimental study of nonlinear flexural and shear deformations of reinforced concrete structural walls, Proceedings, 15th World Conference on Earthquake Engineering, Lisbon, Portugal.

VALIDATION OF SEISMIC DESIGN PROVISIONS FOR DIAPHRAGMS AND ASSESSMENT OF HIGHER-MODE RESPONSES ON EARTHQUAKE-RESISTANT BUILDINGS

C. Franco Mayorga and Georgios Tsampras

Department of Structural Engineering
University of California San Diego

Abstract

This research utilizes recorded strong-motion acceleration data to assess the Alternative Design Provisions for Diaphragms per ASCE/SEI 7-22 Section 12.10.3. The design acceleration coefficients computed using the Alternative Design Provisions are compared with the peak floor accelerations in buildings included in the California Strong Motion Instrumentation Program. Buildings within the California Geological Survey Network with recorded maximum peak floor accelerations larger than 0.2g are considered. Preliminary observations on the magnitude and distribution of the design acceleration coefficients over the height of buildings are presented.

Introduction

Floor diaphragms and their connections to the vertical elements of the seismic force-resisting systems are critical components of earthquake-resistant buildings. Underestimating the level of seismic-induced horizontal forces to which the diaphragms are subjected to could be catastrophic. The loss of the ability of the connections of diaphragms to transfer forces to the seismic force-resisting system could lead to local collapse of the floor or complete collapse of the building. More specifically, diaphragm collapses were observed after the Northridge earthquake due to the loss of connections between floor diaphragms and the vertical elements of precast concrete buildings and the vertical elements of tilt-up-wall buildings (Fleischman et al. (2013), Iverson and Hawkins (1994), Tilt-up-Wall Buildings (1996)). After the 2010-2011 Christchurch earthquakes, excessive damage and collapse of floor diaphragms were attributed to inadequate integrity of the load path, underestimation of seismic-induced horizontal forces, and poorly understood interactions between floor diaphragms and walls, supporting beams, and reinforced concrete (RC) moment frames (Gonzalez et al. (2017), Scarry (2014), Kam et al. (2011)). The complex interactions between diaphragms and other structural elements results to unpredictable seismic response of buildings which often lead to damage of structural members that are designed to remain undamaged (Kam et al. (2011), Bull (2004), Wallace et al. (2012), Henry et al. (2017)).

Earthquake numerical simulations of buildings have shown that the seismic-induced horizontal forces in floor diaphragms can be large relative to the strength of the floor diaphragms. These excessive forces can lead to an inelastic and potentially non-ductile response of the diaphragms (Fleischman and Farrow (2001)). The contribution of second and higher mode responses in the total dynamic response of buildings (termed higher mode effects) may contribute to the excessive forces and floor total accelerations (Sewell et al. (1986), Chopra

(2007)). For instance, it has been shown that high floor accelerations due to the higher mode effects can be expected in buildings with seismic force-resisting systems that develop a flexural yield mechanism at the base, such as flexural-dominant RC structural walls (Chopra (2007), Priestley and Amaris (2012), Wiebe sand Christopoulos (2009), Panagiotou and Restrepo (2009), Tsampras (2016)).

The Alternative Design Provisions for Diaphragms per ASCE/SEI 7-22 Section 12.10.3 provide estimates of the seismic-induced horizontal forces that can be used to design floor diaphragms. These force estimates were developed based on analysis of experimental data from shaking table tests (Panagiotou et al. (2011), Chen et al. (2016)) and earthquake numerical simulations (Choi et al. (2008), Fleischman (2013)). These force estimates consider the higher mode effects. Thus, it is expected that they should result in a more accurate estimate of the seismic-induced horizontal forces for the design of floor diaphragms.

Recently, the California Strong Motion Instrumentation Program (CSMIP) funded a project that aims to utilize recorded acceleration data to validate the seismic design provisions for diaphragms and assess the effect of higher-mode responses on the seismic response of earthquake-resistant buildings. This paper presents preliminary analysis results of the ongoing project. The design equations per ASCE/SEI 7-22 Section 12.10.3 are summarized. A preliminary assessment of the effect of the design parameters N, R, Ω_0, and z_s (defined later) on the design acceleration coefficients for an assumed structural system is presented. The instrumented buildings under consideration in this preliminary analysis are introduced. Buildings within the California Geological Survey Network (CE) that have more than 12 stories and have been subjected to maximum peak floor accelerations larger than 0.2g are considered in this preliminary analysis. A method that is available in the literature (Şafak and Çelebi 1990) is used to estimate the location of the center of rigidity over the height of a building. This method is validated by replicating calculations given in Şafak and Çelebi (1990). The recorded acceleration data used in this preliminary analysis are transformed to the center of rigidity. A comparison between the design acceleration coefficients and transformed measured peak floor accelerations is performed. Conclusions based on the preliminary analysis results are presented.

ASCE/SEI 7-22 Section 12.10.3 Alternative Design Provisions for Diaphragms

In-plane seismic design forces for diaphragms, including chords, collectors, and their connections to the vertical elements are given in Section 12.10.3 Alternative Design Provisions for Diaphragms of the ASCE/SEI 7-22. The in-plane seismic design forces are defined as

$$F_{px} = \frac{C_{px}}{R_s} w_{px} \geq 0.2\, S_{DS} I_e w_{px} \tag{1}$$

where C_{px} is the design acceleration coefficient at level x, w_{px} is the weight tributary to the diaphragm at level x, R_s is the diaphragm design force reduction factor, S_{DS} is the design, 5% damped, spectral response acceleration parameter at short periods, and I_e is the building importance factor. The distribution of design acceleration coefficients over the normalized building height is presented in Figure 1. In this figure, N is the number of stories above the base, h_x is the height above the base to the level x, h_n is the vertical distance from the base to the

highest level of the seismic force-resisting system (SFRS) of the structure, and C_{p0} is the diaphragm acceleration coefficient at the base. C_{p0} is computed as

$$C_{p0} = 0.4 S_{DS} I_e \tag{2}$$

C_{pi} is the diaphragm design acceleration coefficient at 80% of h_n calculated as

$$C_{pi} = \max\left(0.8 C_{p0}, 0.9 \Gamma_{m1} \Omega_0 C_s\right) \tag{3}$$

where $\Gamma_{m1} = 1 + z_s(1 - 1/N)/2$ is the first modal contribution factor, Ω_0 is the overstrength factor, and C_s is the seismic response coefficient in accordance with Section 12.8.1.1 of the ASCE/SEI 7-22. The term C_{pn} is the diaphragm design acceleration coefficient at h_n computed as

$$C_{pn} = \sqrt{(\Gamma_{m1} \Omega_0 C_s)^2 + (\Gamma_{m2} C_{s2})^2} \geq C_{pi} \tag{4}$$

where

$$C_{s2} = \begin{cases} \min\left(\frac{I_e S_{D1}}{0.03(N-1)}; (0.15N + 0.25) I_e S_{DS}; I_e S_{DS}\right), & N \geq 2 \\ 0 & , \ N = 1 \end{cases} \tag{5}$$

is the higher mode seismic response coefficient and $\Gamma_{m2} = 0.9 z_s (1 - 1/N)^2$. N was previously defined and z_s is the mode shape factor defined in Section 12.10.3.2.1 of the ASCE/SEI 7-22.

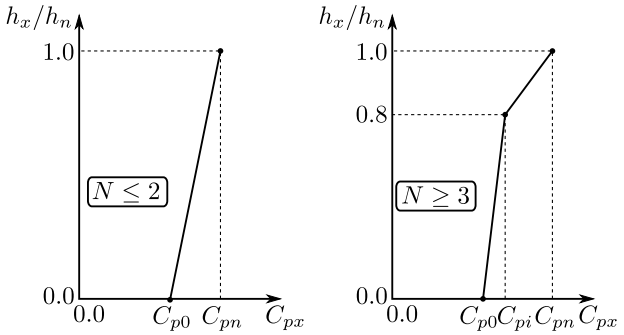

Figure 1 Calculation of the design acceleration coefficients in buildings with N ≤ 2 and in buildings with N ≥ 3 (Figure 12.10-2 in ASCE/SEI 7-22)

Effect of Parameters N, R, Ω_0, and z_s

This section presents the effect of the primary design parameters in the values of C_{px}. An example building with constant story height of 10.0 [ft] is assumed. $S_s = 1.93[g]$ and $S_1 = 0.75[g]$, and Class D site as defined in ASCE/SEI 7-22 are also assumed. The varying parameters are the following: $N = 10, 20, 30, 40, 50$, $R = 4.0, 4.5, 5.0, 5.5., 6.0$, $\Omega_0 = 2.0, 2.2, 2.4, 2.6, 2.8, 3.0$ and $z_s = 0.3, 0.7, 0.85, 1.0$. The results of the sensitivity analysis are shown in Figure 2 for $R_s = 1$. The first plot shows the results for varying N and constant $R = 5.0$, $\Omega_0 = 2.6$, and z_s=1.0. The second plot shows the results for varying R and constant $N = 20$,

$\Omega_0 = 2.6$, and z_s=1.0. The third plot shows the results for varying Ω_0 and constant $N = 20$, $R = 5.0$, and z_s=1.0. The fourth plot shows the results for varying z_s and constant $N = 20$, $R = 5.0$, and $\Omega_0 = 2.6$.

The fundamental period of the structure is estimated using the equations given in Section 12.8.2.1 of the ASCE/SEI 7-22. This fundamental period is used to compute the seismic response coefficient C_s from the design acceleration spectrum. As N increases the fundamental period increases, C_s at the fundamental period decreases and, as a result, C_{px} overall decreases as shown in Figure 2. As N increases Γ_{m1} and Γ_{m2} tend to $1 + z_s/2$ and $0.9z_s$, respectively, as shown in Figure C12.10-3 in ACSE 7-16 Section C12.10.3.2. Note that there is a considerable reduction of the parameter C_{pi} from $N = 20$ to $N = 30$. For $N \geq 30$, the variation of C_{pi} with respect to N is not appreciable. The variation of C_s with respect to the value of period is lower within the range of longer periods, and consequently the variation of C_{pi} is lower within the range of longer periods. In addition, N also affects the higher mode seismic response coefficient C_{s2} governed by the term $I_e S_{D1}/0.03(N-1)$.

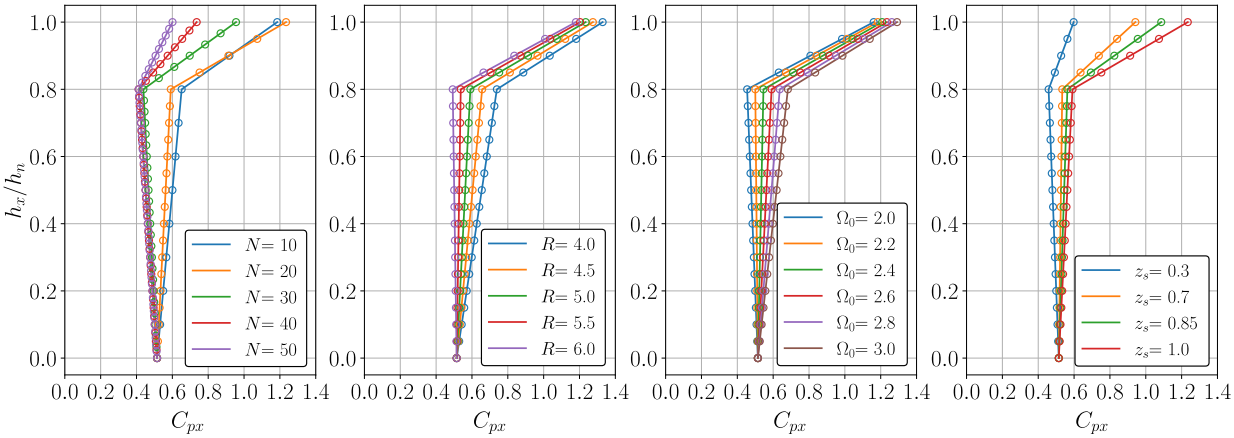

Figure 2 Design acceleration coefficients C_{px}. The number of stories N, the response modification factor of the structure R, the overstrength factor Ω_0, and the mode shape factor z_s effect

Parameters R and Ω_0 directly affect the contribution of the first mode to the C_{px} values. Figure 2 shows that an increase of R results to a reduction of the C_{px} values. An increase of Ω_0 results to an increase of the C_{px} values. These results are consistent with the fact that the inelastic response of SFRS (i.e., R is larger than 1) reduces the level of force responses in the building, and the overstrength in the inelastic response of SFRS increases the level of force responses in the building.

The mode shape factor z_s is positive linearly related to the modal contribution factors Γ_{m1} and Γ_{m2}. z_s affects more the value of Γ_{m2} compared to the value of Γ_{m1}. Therefore, an increase of z_s results to a higher increase in the value of C_{pn} compared to the value of C_{pi} as shown in Figure 2. z_s captures the differences in the distribution of inelastic deformation over the height of different types of seismic force-resisting systems (Section C12.10.3.2 of the ASCE/SEI 7-22).

Buildings Considered in Preliminary Analysis

A set of fourteen instrumented buildings that are part of the California Strong Motion Instrumentation Program (CSMIP) were selected to compare their peak floor accelerations to the design acceleration coefficients defined in the previous section. More specifically, the buildings considered in this preliminary study have more than 12 stories, they were designed assuming risk category II, and soil class D and C, they belong in the California Geological Survey Network (CE), and they have been subjected to ground motions that resulted to recorded floor accelerations larger than 0.2g. Twenty cases of analysis that consider unique combinations of building stations and seismic events are defined in Table 1. Table 1 lists the station of measurement, recorded seismic event, design date, design code, number of stories, building risk category, site class, spectral response acceleration parameter at short periods S_s, and spectral response acceleration parameter at a period of 1 [s] S_1 for each analysis case. These spectral acceleration parameters are obtained based on the building location in terms of latitude and longitude given on the Center for Engineering Strong Motion Data (CESMD) website https://www.strongmotioncenter.org/ and the risk category defined in terms of the building use or occupancy.

Table 1 Analysis case, station of measurement, recorded seismic event, design date, design code, number of stories, building risk category, site class, spectral response acceleration parameter at short periods S_s, and spectral response acceleration parameter at a period of 1 [s] S_1

Case	Station	Recorded seismic event	Design date	Design code**	No. of stories*	Risk Category	Soil Class	S_s[g] *****	S_1[g] *****
1	CE14654	Northridge (1994)	1985	UBC-82	14	II	D	1.851	0.652
2	CE24236	Whittier (1987)	1925	--	14	II	D	2.092	0.750
3	CE24322 ***	Northridge (1994)	1964	--	13	II	D	1.962	0.700
4	CE24322	Encino (2014)	1964	--	13	II	D	1.962	0.700
5	CE24464	Northridge (1994)	1967	LABC-66	20	II	C	2.082	0.747
6	CE24566	Northridge (1994)	1971	--	12	II	C	2.090	0.762
7	CE24569	Northridge (1994)	1961	LABC-60	15	II	C	1.993	0.710
8	CE24601	Landers (1992)	1980	--	17	II	C	1.978	0.705
9	CE24601	Northridge (1994)	1980	--	17	II	C	1.978	0.705
10	CE24602	Sierra Madre (1991)	1988-90	--	52	II	C	1.967	0.700
11	CE24602	Northridge (1994)	1988-90	--	52	II	C	1.967	0.700
12	CE24602	Chino Hills (2008)	1988-90	--	52	II	C	1.967	0.700
13	CE24643	Northridge (1994)	1967	--	19	II	D	2.082	0.744
14	CE24643	Northridge (1994)	1967	--	19	II	D	2.082	0.744
15	CE24680	Encino (2014)	1965	LABC-64	14	II	D	2.270	0.720
16	CE57357	Mt. Lewis (1986)	1972	--	13	II	D	1.530	0.523
17	CE57357 ****	Loma Prieta (1989)	1972	--	13	II	D	1.530	0.523
18	CE58480	Loma Prieta (1989)	1964	--	18	II	D	1.500	0.600
19	CE58483	Loma Prieta (1989)	1964	--	24	II	C	1.802	0.686
20	CE58639	Berkeley (2018)	1975	UBC-73	13	II	C	1.865	1.865

* Number of stories above the ground level
** Design code given in the building station websites. UBC: Uniform Building Code. LABC: Los Angeles Building Code.
*** The building was strengthened with friction dampers after the 1994 Northridge Earthquake.
**** 96 dampers were installed after the Loma Prieta Earthquake to reduce building movement.
***** S_s and S_1 are obtained based on the building location and Risk Category.

Based on the design date (and design code when available), seismic force-resisting systems (SFRS) defined in Table 12.2-1 of the ASCE/SEI 7-22 are assumed for the analysis cases given in Table 1. Table 2 lists the assumed seismic force-resisting system, the corresponding response modification coefficient R, and overstrength factor Ω_0. The considered SFRS are: Precast RC shear walls (SFRS A5), steel concentrically braced frames (SFRS B2), steel moment-resisting frames (SFRS C3), RC moment-resisting frames (SFRS C6), and dual systems (steel concentrically braced frames and moment-resisting frames (SFRS E1), and RC shear walls and moment-resisting frames (SFRS E8)). Additionally, Table 2 lists the approximate fundamental period used to compute the seismic response coefficient C_s. These periods are estimates of the actual periods of the buildings based on approximate equation provided in ASCE/SEI 7-22. In future work, the authors are planning to estimate the periods using identification methods based on the recorded data (Moaveni et al. (2011), Harris et al. (2015), Xiang et al. (2016), Astroza et al. (2016)).

Table 2 Assumed seismic force-resisting systems, response modification coefficients R, overstrength factors Ω_0, and the approximated fundamental periods T

Case	Assumed Seismic Force-Resisting System (SFRS)*	Response modification factor R	Overstrength factor Ω_0	Approximated fundamental period $T \approx c_u T_a$ [s]
1	E1	6.0	2.5	1.421
2	E8	5.5	2.5	1.193
3	C6	5.0	3.0	2.206
4	C6	5.0	3.0	2.206
5	C6	5.0	3.0	2.572
6	C3	4.5	3.0	2.363
7	C3	4.5	3.0	2.825
8	A5	4.0	2.5	1.198
9	A5	4.0	2.5	1.198
10	B2	6.0	2.0	3.876
11	B2	6.0	2.0	3.876
12	B2	6.0	2.0	3.876
13	C3	4.5	3.0	3.454
14	B2	6.0	2.0	1.865
15	E8	5.5	2.5	1.266
16	C3	4.5	3.0	2.564
17	C3	4.5	3.0	2.564
18	C3	4.5	3.0	3.036
19	E8	5.5	2.5	1.594
20	A5	4.0	2.5	0.976

* The SFRS nomenclature refers to Table 12.2-1 of the ASCE/SEI 7-22.
** The upper limit of the approximated fundamental period $c_u T_a$ given in Section 12.8.2.1 of the ASCE/SEI 7-22 is used as the fundamental period T in the computation of the seismic response coefficient C_s.

It is noted that at this time the preliminary analysis considers a limited number of buildings. The authors will expand the scope of the analysis to include a larger number of buildings.

Estimation of Floor Accelerations at the Center of Rigidity

The torsional component of the seismic response of buildings may contribute to the floor

total accelerations measured away from the center of rigidity of the buildings (e.g., sensor 18 on the 49th floor of the CE24602 building station shown in Figure 3). This contribution of the torsional response to the floor total acceleration is more important for buildings with asymmetric floor plans in which the center of mass is expected to be located eccentrically with respect to the center of rigidity. In this study, the recorded floor total accelerations are decomposed to two horizontal translational components of accelerations and one torsional component of accelerations at the center of rigidity. At the center of rigidity, the horizontal translational floor accelerations are theoretically independent of the torsional floor accelerations. In this study, C_{px} values are compared to the horizontal translational accelerations computed at the center of rigidity using the accelerations measured at the location of the sensors.

The location of the center of rigidity at a floor of a building primarily depends on the elastic properties of the structural system. However, the actual location of the center of rigidity is affected by the nonstructural components and the inelastic response of the building. Şafak and Çelebi (1990) proposed a method to compute the center of rigidity from recorded acceleration data. This method is used to compute the location of the center of rigidity in this paper.

Theoretically, the translational motions are not correlated with the torsional motion at the center of rigidity. However, due to measurement errors and considering the possibility of having coupled translational-torsional modes in buildings, the cross-correlation is different to zero when recorded translational floor accelerations and torsional floor accelerations are compared. Based on this, Şafak and Çelebi relaxed the condition of zero cross-correlation. Şafak and Çelebi proposed to minimize the cross-correlation in function of the feasible coordinates of the center of rigidity.

To apply the method proposed by Şafak and Çelebi (1990), the measurements must satisfy the following conditions: (1) At least three measurements are required; (2) the measurements should be obtained from a minimum of two different point locations on the floor; (3) the directions of the measurements should not intersect at one point; and (4) the directions of measurements should not be parallel. Then, it is assumed that the data is measured at points P and Q with coordinates (x_p, y_p) and (x_q, y_q), respectively. Considering that the seismic response of the building results in torsion that can be assumed to be small (i.e., small angle approximation), the translational and torsional motions of a point G (x_g, y_g) located in another point on the floor plane can be computed as

$$\begin{aligned} U_g &= U_p + (y_p - y_g)\theta \\ V_g &= V_p - (x_p - x_g)\theta \end{aligned} \tag{6}$$

where (U_p, V_p) and (U_g, V_g) are the translational motions of the points P and G, respectively, and $\theta = -(U_p - U_q)/(y_p - y_q) = (V_p - V_q)/(x_p - x_q)$ is the floor torsional rotation (independent of the coordinate reference). Note that, for the implemented criterion, G is considered equal to the center of rigidity when the cross-correlation between U_g and θ termed $R_{U_g\theta}(t, \tau)$, or the cross correlation between V_g and θ termed $R_{V_g\theta}(t, \tau)$, are minimum. In general, the cross-correlation for nonstationary functions is a function of both time t and correlation lag τ , however, it is assumed that $R_{U_g\theta}$ and $R_{V_g\theta}$ are functions of τ only. Alternatively in the frequency domain, the

coherence function between U_g and θ termed $\Gamma_{U_g\theta}(f)$, or the coherence function between V_g and θ termed $\Gamma_{V_g\theta}(f)$, can be minimized to find the location of the center of rigidity. At the center of rigidity these motions are expected to be incoherent, but the results could be affected by the frequency content. Şafak and Çelebi (1990) proposed to use the area under the coherence function as an approximate frequency-independent measure defined as shown below

$$L_{U_g\theta} = \int_0^\infty \Gamma^2_{U_g\theta}(f)\, df \quad \text{and} \quad L_{V_g\theta} = \int_0^\infty \Gamma^2_{V_g\theta}(f)\, df \tag{7}$$

where

$$\Gamma^2_{U_g\theta}(f) = \frac{\left|S_{U_g\theta}(f)\right|^2}{S_{U_gU_g}(f)S_{\theta\theta}(f)} \quad \text{and} \quad \Gamma^2_{V_g\theta}(f) = \frac{\left|S_{V_g\theta}(f)\right|^2}{S_{V_gV_g}(f)S_{\theta\theta}(f)} \tag{8}$$

and $S_{lm}(f)$ is the cross-spectrum of the corresponding l and m signals (power spectra or auto-spectra when $l = m$).

Figure 4 shows the results of the calculation of the coherence area that are used to estimate the center of rigidity of the 49th floor of the building station CE24602 (see Figure 3) for the recorded seismic events: Sierra Madre (1991), Northridge (1994), and Chino Hills (2008) (cases 10, 11, 12, respectively, in Table 1). The sensor coordinates with respect to the center of geometry of the floor plan are estimated from the schematics shown in Figure 3. Table 3 lists the coordinates that minimize the coherence areas for each seismic event. These coordinates are estimates of the coordinates of the center of rigidity for each seismic event. As expected, the actual location of the center of rigidity depends on the considered seismic event. The estimate of y_g coordinate is similar using accelerations from the three seismic events (between 4.68 [ft] and 6.24 [ft]). The estimate of x_g coordinate is 24.96 [ft] considering the seismic event Sierra Madre (1991) and it shifts to 35.88[ft] considering the seismic event Northridge (1994).

Table 3 Coordinates of the center of rigidity of the 49th story

Case	Seismic event	Center of rigidity coordinates	
		x_g [ft]	y_g [ft]
10	Sierra Madre (1991)	24.96	4.68
11	Northridge (1994)	35.88	6.24
12	Chino Hill (2008)	35.88	4.68

In the case in which an instrumented floor has only two orthogonal measurements, such as the 14th floor of the CE24602 building station shown in Figure 3, the torsional rotation cannot be computed. In these cases, the two orthogonal measurements of acceleration are used in this preliminary study.

In the future, the authors are planning to compare the results obtained from the presented method used to estimate the location of the center of rigidity against the location of the center of rigidity estimated using the structural floor plans of buildings.

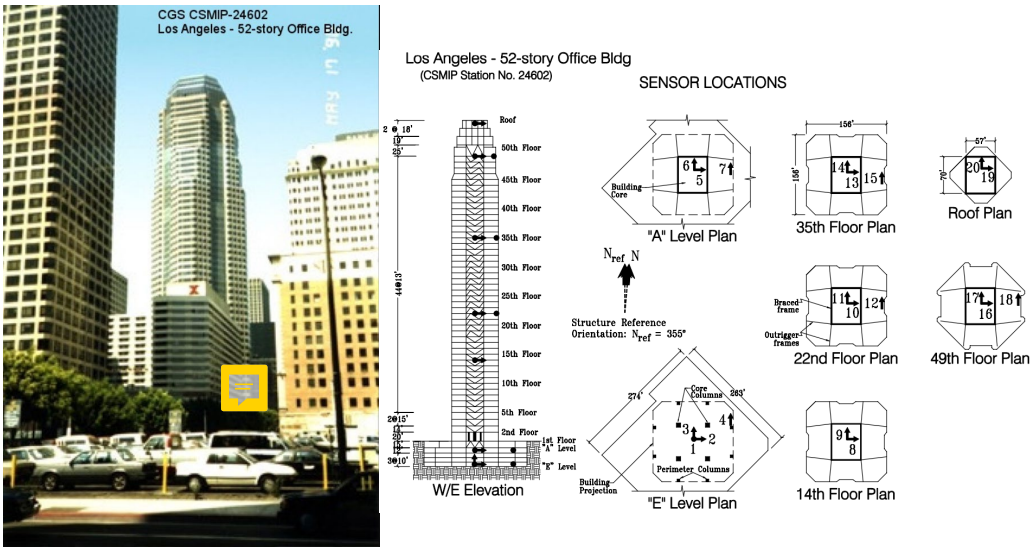

Figure 3 Cases 10, 11, and 12: moment frame building (https://www.strongmotioncenter.org/cgi-bin/CESMD/stationhtml.pl?stationID=CE24602&network=CGS)

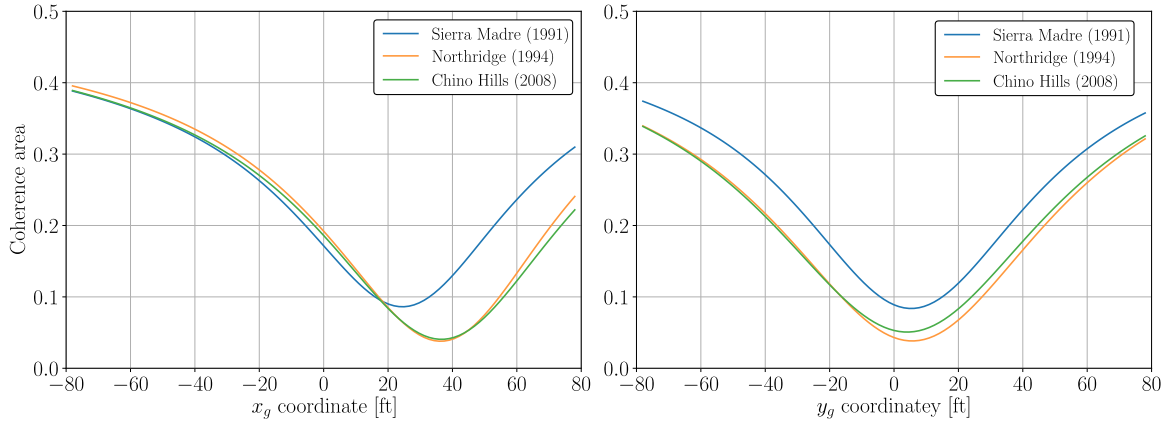

Figure 4 Coherence area versus trial center of rigidity coordinates of the 49th floor. Caso 10: Sierra Madre earthquake (1991), Case 11: Northridge earthquake (1994), and Case 12: Chino Hill earthquake (2008)

Comparison between Design Acceleration Coefficients and Measured Peak Floor Accelerations

Once the responses at the center of rigidity are obtained, the peak horizontal floor accelerations at the instrumented floors are computed. The objective of this preliminary analysis is to compare the magnitude of the peak floor accelerations with the C_{px} values and graphically identify the floors in which higher amplifications of recorded peak floor accelerations with respect to the peak ground accelerations are observed. The preliminary analysis does not compare the distribution of peak floor accelerations over the height of the building with the distribution of C_{px} values over the height of the building. This is because the inelastic response of buildings expected under the design level ground motions may limit the higher mode effects on the peak floor accelerations. Therefore, a comparison between the distribution of peak floor accelerations and the distribution of C_{px} values over the height of the building requires recorded ground motions with intensities close to the seismic design level intensity. Most of the buildings

considered in this preliminary analysis are not subjected to recorded ground motions with intensities close to the design level intensity. Nevertheless, additional buildings in the CSMIP dataset with recorded total accelerations close to the design level intensity will be included in future analysis. For these additional buildings, the distribution of peak floor accelerations versus the distribution of C_{px} values will be compared.

Figure 5 shows the distribution of the peak floor accelerations and the corresponding values of C_{px} over the normalized height of the buildings. Figure 5 shows the results for each analysis case grouped based on the seismic force-resisting system of each building. The square and triangular markers represent the peak floor accelerations in x and y directions, respectively. The solid circular markers are the corresponding C_{px} values for the analysis cases. Analysis cases 3 and 4; 8 and 9; 10, 11, and 12; and 16 and 17 correspond to the same building station subjected to different seismic event. Thus, the C_{px} values for these analysis cases overlap. Cases 13 and 14 correspond to the same building station but with different seismic force-resisting system per direction of analysis. In the longitudinal direction of this building the SFRS is a steel moment frame (SFRS C3) and in the transverse direction of this building the SFRS is a steel concentrically braced frame (SFRS B2). As a result, there are two different distributions of C_{px} values for this building. Table 4 lists the maximum ratio of the measured peak floor accelerations over the C_{px} values for all the analysis cases. This ratio is termed Maximum M/D ratio.

Table 4 Maximum floor acceleration Measured-Design (M/D) ratios

Case	Maximum M/D ratio	Case	Maximum M/D ratio
1	0.52	11	0.80
2	0.23	12	0.52
3	**1.56**	13	**1.25**
4	0.81	14	**1.24**
5	0.66	15	0.51
6	0.51	16	0.73
7	0.47	17	0.82
8	0.29	18	0.78
9	0.52	19	0.53
10	0.45	20	0.33

Figure 5 shows that the peak floor accelerations do not exceed the C_{px} values for most of the cases considered in this analysis, except for Cases 3, 4, and 13 which are discussed at the end of this section. Accordingly, all the M/D ratios presented in Table 4 are lower than one (except for Cases 3, 4, and 13). These results are consistent with the fact that the intensity of the recorded ground motions to which the buildings were subjected to are lower than the seismic design level intensity. Thus, if these buildings had been designed following the current alternative design provisions for diaphragms, the induced inertial forces for the recorded seismic events would have been expected to be lower than the diaphragm design strengths.

Figure 5 shows an amplification in the peak total accelerations at the higher floors of the buildings that are subjected to the larger ground motion intensities in the SFRS A5 and B2 analysis cases. Similar amplification is observed in the peak total accelerations along the x-

direction in Cases 5 and 19 that correspond to SFRS C6 and E8, respectively. This amplification is not identified in the SFRS C3 analysis cases.

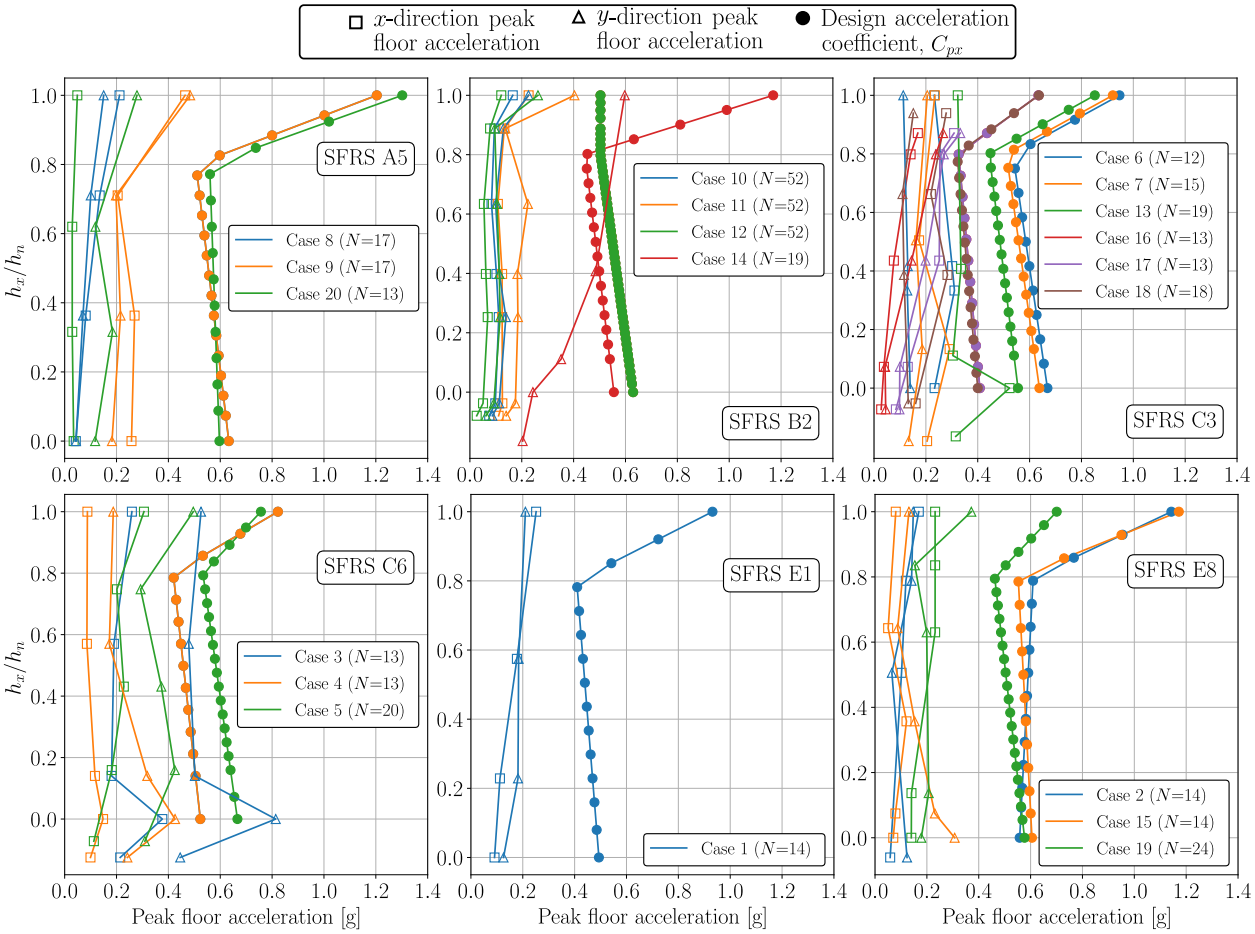

Figure 5 Diaphragm design acceleration coefficients versus peak floor accelerations at the center of rigidity comparison.

Cases 10, 11 and 12 correspond to the same building station (CE24602) subjected to three different recorded ground motions (Sierra Madre (1991), Northridge (1994), and Chino Hills (2008)). These analysis cases demonstrate that the distribution of peak floor accelerations over the height of the building depends on the intensity of the ground motions. A larger amplification in the roof acceleration is observed in the upper floors in the *y*-direction of Case 11 compared to the other two analysis cases. Case 11 corresponds to the recorded seismic event with the largest seismic intensity for this building station (Northridge seismic event). The authors are currently working on the comparison of the seismic-induced spectral accelerations with the design spectral accelerations.

The maximum peak floor accelerations were recorded at the second floor in Cases 3, 4, and 13. The distribution of peak floor accelerations over the height of the building in Case 14 abruptly increased after the first floor. The observations associated with the above-mentioned analysis cases are attributed to the structural irregularities over the height of the buildings. Performance-based assessment of these buildings could be used to estimate the diaphragm design forces.

Conclusions

This paper presented a summary of the ASCE 7-22 alternative design provisions for diaphragms. Results from a limited sensitivity analysis of the design acceleration coefficients (C_{px}) with respect to parameters N, R, Ω_o, and z_s were presented. The instrumented buildings considered in this preliminary analysis were introduced. A method to estimate the location of the center of rigidity over the height of a building using recorded acceleration data proposed by Şafak and Çelebi (1990) was introduced. A comparison between the values of the design acceleration coefficients and the measured peak floor accelerations transformed at the center of rigidity was performed.

The preliminary analysis shows that the recorded peak floor accelerations of the buildings in this study are generally smaller than the C_{px} values. The recorded peak floor accelerations in buildings with vertical irregularities were larger than the C_{px} values. The distribution of the peak floor accelerations over the height depends on the ground motion intensity. Future analyses will include larger number of buildings to derive detailed conclusions with respect to the recorded peak floor accelerations compared to the C_{px} values.

Acknowledgments

The authors acknowledge to the California Strong Motion Instrumentation Program for their support through the project called "Validation of Seismic Design Provisions for Diaphragms and Assessment of Higher-Mode Responses on Earthquake-Resistant Buildings" and to the Chilean National Agency for Research and Development (ANID) for their support through the foreign doctoral scholarship 2020. The authors also acknowledge to Mehmet Çelebi, PhD, PE and Lisa S. Schleicher, Ph.D., Geophysicist, both part of the USGS, for facilitating the data required to replicate the results given in Şafak and Çelebi (1990). Any opinions, findings, and conclusions expressed in this paper are those of the authors and do not necessarily reflect the views of others acknowledged here.

References

ASCE/SEI 7-22 (2021). Minimum design loads and associated criteria for buildings and other structures. *American Society of Civil Engineers*.

Astroza, Rodrigo, Ebrahimian, H., Conte, J. P., Restrepo, J. I., and Hutchinson, C. T. (2016). System Identification of a Full-Scale Five-Story Reinforced Concrete Building Tested on the NEES-UCSD Shake Table. *Structural Control and Health Monitoring* 23, no. 3: 535–59. https://doi.org/10.1002/stc.1778.

Bull, D. K. (2004). Understanding the Complexities of Designing Diaphragms in Buildings for Earthquakes. *Bulletin of the New Zealand Society for Earthquake Engineering* 37, no. 2: 70–88. https://doi.org/10.5459/bnzsee.37.2.70-88.

Chen, Michelle C., Pantoli, E., Wang, X., Astroza, R., Ebrahimian, H., Hutchinson, T.C., Conte, J.P., Restrepo, J. I., Marin, C., Walsh, K. D., Bachman, R.E., Hoehler, M.S., Englekirk,

R., and Faghihi, M. (2016). "Full-Scale Structural and Nonstructural Building System Performance during Earthquakes: Part I – Specimen Description, Test Protocol, and Structural Response." *Earthquake Spectra* 32, no. 2: 737–70. https://doi.org/10.1193/012414eqs016m.

Choi, H., Christopoulos, C., and Tremblay, R. (2008). Comparison of the Seismic Response of Steel Buildings Incorporating Self-Centering Energy Dissipative Braces, Buckling Restrained Braced and Moment Resisting Frames. Research Report 05-2008, University of Toronto,Canada.

Chopra, Anil K (2007). *Dynamics of Structures*. Pearson Education.

Fleischman, R. B., and Farrow, K. T. (2001). Dynamic Behavior of Perimeter Lateral-System Structures with Flexible Diaphragms. *Earthquake Engineering & Structural Dynamics* 30, no. 5: 745–63. https://doi.org/10.1002/eqe.36.

Fleischman, R. B., Restrepo, J. I., Naito, C. J., Sause, R., Zhang, D., and Schoettler, M. (2013). "Integrated Analytical and Experimental Research to Develop a New Seismic Design Methodology for Precast Concrete Diaphragms." *Journal of Structural Engineering* 139, no. 7: 1192–1204. https://doi.org/10.1061/(ASCE)ST.1943-541X.0000734.

González, Alfredo, Spacone, E., and Nascimbene, R. (2017). Performance-Based Seismic Design Framework for RC Floor Diaphragms in Dual Systems. *Procedia Engineering*, X International Conference on Structural Dynamics, EURODYN 2017, 199: 3546–51. https://doi.org/10.1016/j.proeng.2017.09.512.

Harris, Angie, Xiang Y., Naeim, F., and Zareian, F. (2015). Identification And Validation of Natural Periods and Modal Damping Ratios for Steel and Reinforced Concrete Buildings in California. *SMIP15 Seminar Proceedings*.

Henry, Richard S., Dizhur, D., Elwood, K. J., Hare, J., and Brunsdon, D (2017). Damage to Concrete Buildings with Precast Floors during the 2016 Kaikoura Earthquake. *Bulletin of the New Zealand Society for Earthquake Engineering* 50, no. 2: 174–86. https://doi.org/10.5459/bnzsee.50.2.174-186.

Iverson, J. K., and Hawkins, N. M. (1994). Performance Of Precast/Prestressed Building Structures During Northridge Earthquake. *PCI Journal* 39, no. 2. https://trid.trb.org/view/390643.

Kam, W. Y., Pampanin, S., and Elwood, K. (2011). Seismic Performance of Reinforced Concrete Buildings in the 22 February Christchurch (Lyttleton) Earthquake. *University of Canterbury. Civil and Natural Resources Engineering*. https://ir.canterbury.ac.nz/handle/10092/9006.

Moaveni, Babak, He, X., Conte, J. P., Restrepo, J. I., and Panagiotou, M. (2011). System Identification Study of a 7-Story Full-Scale Building Slice Tested on the UCSD-NEES

Shake Table. *Journal of Structural Engineering* 137, no. 6: 705–17. https://doi.org/10.1061/(ASCE)ST.1943-541X.0000300.

Panagiotou, Marios, and Restrepo, J. I. (2009). Dual-Plastic Hinge Design Concept for Reducing Higher-Mode Effects on High-Rise Cantilever Wall Buildings. *Earthquake Engineering & Structural Dynamics* 38, no. 12: 1359–80. https://doi.org/10.1002/eqe.905.

Panagiotou, Marios, Restrepo, J. I., and Conte, J. P. (2011). Shake-Table Test of a Full-Scale 7-Story Building Slice. Phase I: Rectangular Wall. *Journal of Structural Engineering* 137, no. 6: 691–704. https://doi.org/10.1061/(ASCE)ST.1943-541X.0000332.

Priestley, M. J., and Alejandro D. Amaris (2012). *Dynamic Amplification of Seismic Moments and Shear Forces in Cantilever Walls*. IUSS Press.

Şafak, Erdal, and Çelebi, M (1990). Method to Estimate Center of Rigidity Using Vibration Recordings. *Journal of Structural Engineering* 116, no. 1: 85–97. https://doi.org/10.1061/(ASCE)0733-9445(1990)116:1(85).

Scarry, J M (2014). Floor Diaphragms – Seismic Bulwark or Achilles' Heel. *NZSEE Conference*, Auckland, New Zealand.

Sewell, R. T., Cornell, C. A., Toro, G. R., and McGuire, R. K. (1986). A Study of Factors Influencing Floor Response Spectra in Nonlinear Multi-Degree-of-Freedom Structures. *John A. Blume Earthquake Engineering Center Technical Report Series*. https://purl.stanford.edu/vf765pj9489.

The Pandas Development Team (2020). Pandas-dev/pandas: Pandas. *Zenodo*. https://doi.org/10.5281/zenodo.3509134.

Tilt-up-Wall Buildings. (1996). *Earthquake Spectra* 12, no. 1 (suppl): 99–123. https://doi.org/10.1193/1.1585922.

Tsampras, Georgios, Sause, R, Zhang, D., Fleischman, R. B, Restrepo, J. I., Mar, D., and Maffei, J. (2016). Development of Deformable Connection for Earthquake-Resistant Buildings to Reduce Floor Accelerations and Force Responses. *Earthquake Engineering & Structural Dynamics* 45, no. 9: 1473–94. https://doi.org/10.1002/eqe.2718.

Van Rossum, G., & Drake, F. L. (2009). Python 3 Reference Manual. Scotts Valley, CA: CreateSpace.

Wallace, John W., Massone, L. M., Bonelli, P., Dragovich, J., Lagos, R., Lüders, C., and Moehle, J. (2012). Damage and Implications for Seismic Design of RC Structural Wall Buildings. *Earthquake Spectra* 28, no. 1(supl): 281–99. https://doi.org/10.1193/1.4000047.

Wiebe, L., and Christopoulos, C. (2009). Mitigation of Higher Mode Effects in Base-Rocking Systems by Using Multiple Rocking Sections. *Journal of Earthquake Engineering* 13, no. sup1: 83–108. https://doi.org/10.1080/13632460902813315.

Xiang, Yijun, Harris, A., Naeim, F., and Zareian, F. (2016). Identification And Validation of Natural Periods and Modal Damping Ratios for Seismic Design and Building Code. *SMIP16 Seminar Proceedings*.

SIMULATION OF 0-7.5 HZ DETERMINISTIC GROUND MOTIONS FOR MAXIMUM CREDIBLE EARTHQUAKE SCENARIOS AT THE LONG VALLEY DAM, CA

Kim Olsen and Te-Yang Yeh

Department of Geological Sciences
San Diego State University

Abstract

We have used 3D 0-7.5 Hz deterministic wave propagation to model the seismic response of the Long Valley Dam (LVD) in central California. The velocity structure, anelastic attenuation model, and the properties of the dam were calibrated via simulations of a M_w3.7 event and the 1986 M_w6.3 Chalfant Valley earthquake. Our nonlinear simulations of a M_w6.6 Maximum Credible Earthquake scenario generate peak ground accelerations > 1 g at the LVD, where nonlinear damping (Drucker-Prager rheology) reduces PGAs predicted at the dam crest by a factor of 2.5. The simulations predict relative displacements of the dam material of ~ 10 cm.

Introduction

Failure of dams during seismic shaking can have devastating societal consequences. While well-designed Earth dams have generally performed well during earthquake ground shaking (FEMA, 2005), catastrophic failures have still occurred due to various reasons, depending on the ground shaking level, structure design, and material properties (FEMA, 2005; Seed et al., 1978). In this work, we have carried out 3D numerical simulations to predict the seismic response of the Long Valley Dam (LVD) for a Maximum Credible Earthquake (MCE). The LVD is a 55 meter high embankment dam located 35 km northwest of Bishop, CA, just east of the Sierra Nevada range. The completion of the dam in 1941 created Lake Crowley which has been serving as a storage unit for the Los Angeles aqueduct as well as a flood control unit. The major part of the dam consists of extensive rolled earth-fill core (Lai and Seed, 1985). The dam has an array of accelerometers located on the dam crest, downstream wall, abutment and downstream bedrock (Fig. 1, left).

The seismic response of the LVD has been extensively studied in which the soil behavior was modeled by different approaches. Lai and Seed (1985) accounted for the nonlinear response of the dam material by using equivalent linear soil properties. Later studies used more rigorous numerical methods (e.g., finite-elements) to simulate the nonlinear hysteretic behavior of the dam material under cyclic loading with multi-surface plasticity theory (Griffiths and Prevost, 1988; Yiagos and Prevost, 1991; Zeghal and Abdel-Ghaffar, 1992). A potential limitation of the earlier studies is the treatment of the excitation of the dam to estimate the seismic response. Typically, stability analyses for dams use an accelerogram of a historical event, for example, recorded near the downstream base as input motion. Conventionally, the same input ground motion is applied at input nodes along the bottom and sides of the dam, approximating the excitation resulting from a vertically incident plane wave. Such assumption may represent an

oversimplification, as it does not account for scattering caused by heterogeneities at all scales. In addition, modeling the dam response using existing records usually requires scaling of the amplitudes, which is now generally a discouraged practice.

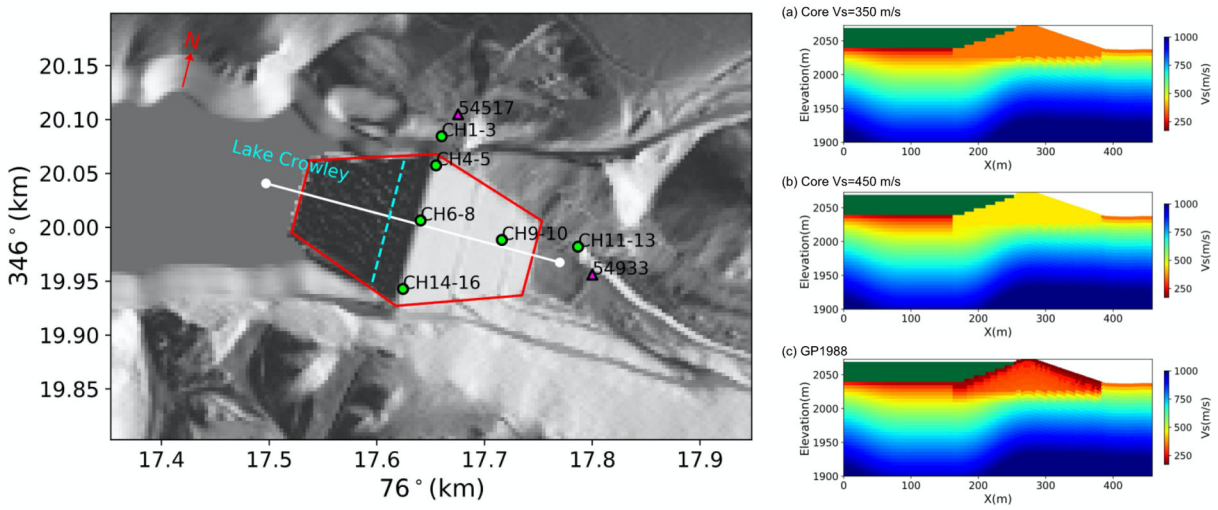

Figure 1: (left) Map view of the Long Valley dam. Blue dashed line depicts the contact of the lake water surface on the upstream face. Green-filled circles are sensor locations in the structure array (station code 54214) installed on the LVD. Magenta triangles are nearby stations, which were used for estimating the geotechnical layer (GTL) tapering depth. (right) 2D Vs transects across the LVD extracted from the three different dam models tested in this study. The dam core in models (a) and (b) is homogeneous, whereas that in (c) has a layered structure computed from the elastic parameters used in Griffiths and Prevost (1988).

The Hilton Creek Fault (HCF) is a significant range-bounding normal fault at the eastern side of the Sierra Nevada Mts. Because it passes just 8 km west of the LVD, it has been identified as a possible source for the MCE that could potentially damage the LVD (Lai and Seed, 1985). Scenario earthquakes on the HCF were also considered in a recent study on earthquake hazards for the Long Valley Caldera-Mono Lake Area by Chen et al. (2014). However, the methods used in this study were based primarily on ground motion prediction equations (GMPEs) which provided only peak ground motion amplitudes and spectral accelerations with very limited spatial resolution. In addition, GMPE-based approaches provide only rudimentary control on the effects of the source parameters, with no support of the complete time history of particle motions (FEMA, 2005). In this study, we utilize the power of supercomputers to address these issues by performing fully-coupled 3D deterministic simulations considering both linear and nonlinear response of the material within the LVD and its surroundings. Our simulation approach enables us to fully account for source, path, and site effects in a single numerical model.

Numerical method

We use the 4th-order accurate finite-difference code AWP-ODC, with support for frequency-dependent attenuation (Cui et al., 2010; Withers et al., 2015). In order to reduce the computational cost, we used 3 velocity meshes separated vertically with a factor-of-three

increase in grid spacing with depth (3.5 m, 10.5 m, and 31.5 m) via a discontinuous mesh approach (Nie et al., 2017). We used a minimum shear wave velocity of 175 m/s in the top block, ensuring at least 6.7 points per minimum wavelength (O'Reilly et al., 2021).

Support for surface topography is needed to model the seismic response of the LVD. For the validation work of the 2015 M_w3.7 event, we used the curvilinear grid approach by O'Reilly et al. (2022). However, this version of AWP-ODC does not yet support nonlinear soil response calculations. For this reason, we performed the validation with the 1986 M_w6.2 Chalfant Valley event and simulations of the HCF scenarios using a Cartesian-grid version of AWP-ODC with a vacuum formulation for the free surface (Graves, 1996). Previous studies clearly show that the accuracy of the vacuum formulation is reduced, as compared to explicit free surface formulations. However, we verified the seismic response of the LVD using the vacuum formulation, as compared to those from the curvilinear solution, to ensure that our analysis of the LVD is sufficiently accurate (not shown).

Velocity model

Our reference model is extracted from the SCEC CVM version 4.26-M01 (CVM-S in the following, Small et al., 2017). It has been shown (Ely et al., 2010; Hu et al., 2022) that CVM-S generally causes underprediction of peak amplitudes and coda duration outside the basins, due to unrealistically high near-surface velocities. To alleviate this underprediction, Ely et al. (2010) proposed a simple generic overlay-based tapering of time-averaged shear wave velocity (V_S) in the top 30 m (V_S30) to merge with tomography at a depth of 350 m. Hu et al. (2022) found that applying the taper to deeper depths (700-1,000 m) significantly improved the fit between deterministic synthetics and strong motion data for the 2014 M_w5.1 La Habra earthquake in the greater Los Angeles area. Following this approach, we estimate the optimal tapering depth for the near-surface material near the LVD in the Sierra Nevada Mts.

For the surface topography, we used the 1m-resolution digital elevation model (DEM) from the U.S. Geological Survey. This DEM does not provide elevations of areas under water, including part of the upstream face and the entire Lake Crowley. As we need to include the lake water directly into our simulations, we made the following adjustments to the DEM. First, we removed the lake water from the DEM by manually lowering the elevations of the grids located inside the lake from 2066 m to 2036 m, assuming a flat lake bed and an average water depth of 30 m. Secondly, we mirrored the surface elevations of the downstream face to the upstream side with respect to the center line of the crest of the dam (axis of the dam), assuming symmetry of the LVD with respect to the axis of the dam. We then applied Gaussian filters of 7 m resolution to smooth the topography around the edges of the area where we removed the lake water, to minimize artifacts introduced by these adjustments. In our calculations, the lake water is modeled as a purely elastic material with V_P=1,050 m/s, V_S=0 m/s, and ρ=1,492 kg/m^3, and the bathymetry of areas under lake water, including the lower portion of the upstream face, are described in a staircase fashion.

Anelastic attenuation

In our simulations, we adopted a frequency-dependent attenuation model where Q_s values are given by

$$Q_s(f) = Q_{s,0}, \quad f < f_0,$$
$$Q_s(f) = Q_{s,0}\left(\frac{f}{f_0}\right)^{\gamma}, \quad f \geq f_0,$$

where the power-law exponent γ controls the rate of increase of Q_s above the transition frequency, f_0, set at 1 Hz (Withers et al., 2015), and $Q_{s,0}$ is a constant Q_s value. Following Olsen et al. (2003), we assumed $Q_{s,0}$ to be proportional to the local S-wave speed, $Q_{s,0} = kV_s$, where k is a parameter specific to the study area. For simplicity, the relationship of $Q_p = 2Q_s$ was assumed throughout this study, following the findings of Olsen et al. (2003). The parameters k and γ are estimated in Section **Anelastic Attenuation**.

Validation I: 2015 M3.7 event

Our first validation event is a M_w3.7 earthquake from 2015. Due to its small magnitude, it is reasonable to approximate this event as a point source, thereby eliminating uncertainty of modeling finite-fault effects. For this reason, we use this event to constrain the anelastic attenuation parameters for the layers in our model domain as well as the depth of the GTL. This event has a normal-faulting focal mechanism (158°/75°/-103°, 20°/20°/-50°) and is located 7 km to the west of the LVD (-118.7878°, 37.5975°) at a depth of 4.8 km (Fig. 2, left). In this analysis we focused on the ground accelerations recorded by strong motion sensors installed on and nearby the dam (structure array 54214, stations 54517 and 54933) which are operated under California Strong Motion Instrumentation Program (CSMIP) with network code CE.

Source description

To describe the source of the M_w3.7 event, we assume a Brune-type spectral shape (Brune, 1970) with a f^{-2} decay at frequencies above the corner frequency (f_c), given by

$$M(f) = \frac{M_0}{1 + (f/f_c)^2},$$

where M_0 is the seismic moment. After an inverse Fourier transform of the source spectrum with the constraint of minimum phase, the moment rate function has the following expression in the time domain,

$$M(t) = \frac{t}{T_c^2} e^{\frac{-t}{T_c}},$$

where T_c is the characteristic time controlling the width of the pulse, which depends on the corner frequency $T_c = 1/2\pi f_c$. We determined the corner frequency using

$$f_c = k\beta \left(\frac{16}{7} \frac{\Delta\sigma}{M_0} \right)^{\frac{1}{3}},$$

where k is a constant, β is the V_s at the source (3,410 m/s), and Δσ is the stress drop. Using k = 0.32 assuming a circular rupture with a rupture speed of $V_r = 0.9V_s$ and a stress drop of 3 MPa, we get $T_c = 0.0593$s, and $f_c = 2.7$Hz.

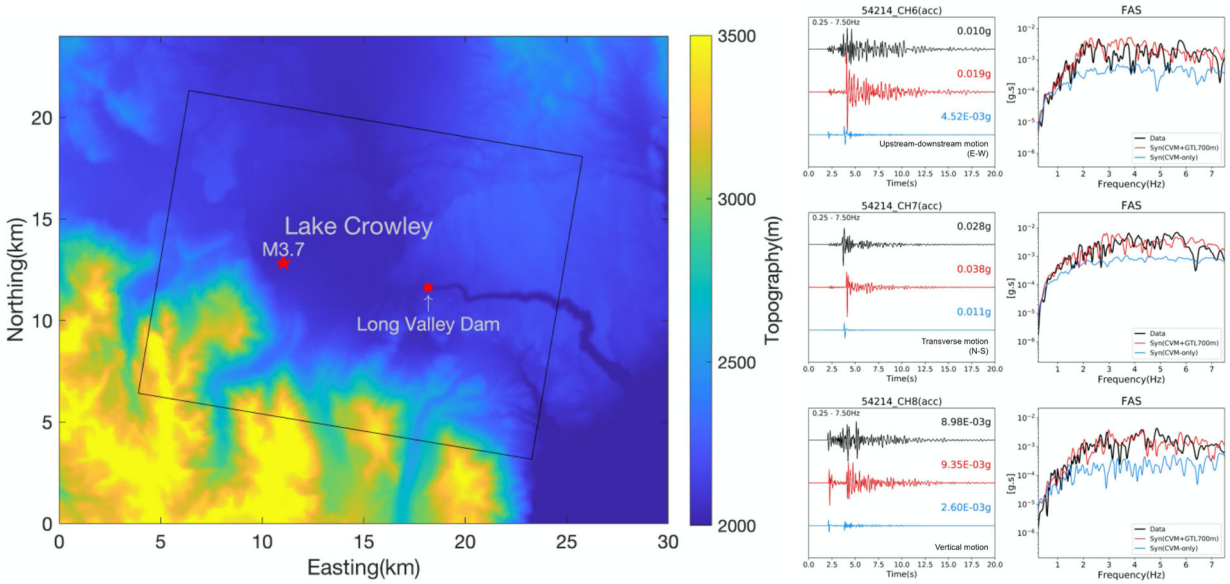

Figure 2. (left) Model domain (black rectangle) for the simulations of the 2015 M_w3.7 earthquake (rotated 9.51° clockwise, model depth 15 km). (right) Comparison of data (black traces) and synthetics (red and blue traces) in the time and FAS domains at sensors located at the dam crest (see Fig. 1 for sensor location). The red synthetic traces were computed with CVM-S, a GTL tapered to 700 m below the free surface, and a dam core with 450 m/s, whereas the blue traces were computed with CVM-S only (no GTL).

Near-surface geotechnical layer (GTL)

We follow the approach of Hu et al. (2022) to calibrate the near-surface velocity structure within our model domain. This calibration entails replacing the velocity model extracted from the SCEC CVM-S, from the free surface to a given tapering depth (z_T) with V_P, V_S, and ρ computed using the formulations of Ely et al. (2010) along with local V_S30 information. This approach provides a smooth transition between the near-surface velocity structures and the original model. We used the measured V_S30 values wherever available, and the values from Wills et al. (2015) elsewhere.

In order to estimate an optimal value for the tapering depth z_T, we compared simulations for models with GTL implemented with z_T of 350 m, 700 m, and 1,000 m to seismic data recorded off the dam (e.g., stations 54517 and 54933). Based on this analysis, we used z_T equal to 700 m in our simulations. This modification resulted in significantly lower V_S values near the surface of the domain as well as a higher degree of spatial complexities compared to CVM-S.

Elastic properties of the LVD

Earlier studies have modeled the LVD with an extensive rolled earthfill clay core, which constitutes the major portion of the dam structure with a thin layer of more permeable rock-fill shell on top (Lai and Seed, 1985; Yiagos and Prevost, 1991; Griffiths and Prevost, 1988). We explored different V_S for the homogeneous dam core as well as more complicated descriptions (see Fig. 1, right), using the M_w3.7 event. Our tests show that a homogeneous core with V_P=1,000 m/s, V_S=350 m/s, and ρ=2,110 kg/m^3 (Fig. 1, right, top) as well the presence of a thin shell with low V_S values used in the Griffiths and Prevost (1988)'s modeling (Fig. 1, right, bottom) overpredict the observed acceleration amplitudes (not shown here). On the other hand, our simulations show that using a homogeneous core with V_P=1,000 m/s, V_S=450 m/s, and ρ=2,110 kg/m^3 (Fig. 1, right, center) provides an unbiased prediction of the observed ground motions in both time and frequency domains. Due to its homogeneous nature, this model makes no distinction between the core and shell of the dam. We note that this model is fairly close to the actual structure of LVD, as an extensive rolled earthfill clay core constitutes the major portion of the dam structure with a thin layer of a more permeable rock-fill shell on top (Lai and Seed, 1985; Yiagos and Prevost, 1991; Griffiths and Prevost, 1988).

Anelastic attenuation

We carried out a grid search to estimate the values of k and γ that provide the best fit to the strong motion records for the M_w3.7 event at the LVD. These simulations included the estimated optimal GTL parameters and elastic properties of the dam, with recorded data both on and near the LVD. As an estimate of goodness-of-fit (GOF) we used the natural logarithm of the observed-to-simulated acceleration Fourier amplitude spectral ratio for all available channels, given by

$$GOF_{FAS}(f) = \ln\left(\frac{FAS_{obs}(f)}{FAS_{model}(f)}\right),$$

where $FAS_{obs}(f)$ and $FAS_{model}(f)$ are Fourier amplitude spectra of observed and simulated acceleration waveforms, respectively. Prior to computing the spectral ratio, both $FASobs(f)$ and $FAS_{model}(f)$ were smoothed with a Savitzky-Golay filter (Savitzky and Golay, 1964) with a 0.5 Hz window length to suppress large fluctuations. We calculated the mean GOF_{FAS} and the corresponding standard deviation between 0.2-7.5 Hz to quantify the model performance. Due to the definition of GOF_{FAS}, a positive value indicates under-prediction and vice versa. In addition, we defined an error value as a summary of the mean GOF_{FAS} over the entire frequency range,

$$Error = \frac{\sum_{i=1}^{Nf} |\mu_i|}{Nf},$$

where μ_i is the mean GOF_{FAS} at frequency point i. The GOF_{FAS} analysis shows a trade-off between k and γ, where (k = 0.05, γ = 0.4), (k = 0.075, γ = 0.2), and (k = 0.1, γ = 0) result in almost identical GOF_{FAS} curves. Based on this result, we proceeded with an intermediate model with k = 0.075 and γ = 0.2 in all following simulations.

Validation results

Our numerical simulation was able to generate synthetics that are reasonably close to the data in both time and frequency domains (see Fig. 2, right). The FAS of the full model (red trace in Fig. 2, right) shows no systematic bias where the model without a geotechnical layer clearly underpredicts the spectral energy across almost the entire frequency range. In summary, the attenuation model using k = 0.075 and γ = 0.2, the homogeneous dam structure with V_P=1,000 m/s, V_S=450 m/s, ρ=2,110 kg/m^3, along with a geotechnical layer in the top 700 m are capable of providing unbiased estimates of the recorded ground motions in both time and frequency domains up to 7.5 Hz.

Validation II: The 1986 M_w6.2 Chalfant Valley earthquake

We used the 2015 M_w3.7 event (Validation I, point source) to validate the CVM-S velocity model for the area, calibrate the attenuation model, and confirm the implementation of the GTL and the 3D structure of the LVD. The model was then used for the second validation event, namely the 1986 M_w6.2 Chalfant Valley earthquake. This earthquake is located 25 km to the east of LVD, which requires a larger computational domain to accommodate the entire fault and LVD (Fig. 3, left). The moment magnitude of this event (M_w6.2) clearly warrants a finite-fault description for its rupture. We use the Graves and Pitarka (2016) kinematic rupture generator to generate finite-fault descriptions for the Chalfant Valley event, described in the following section.

Finite-fault source model

The hypocenter locations for the Chalfant Valley earthquake reported by previous studies are fairly similar (varying horizontally ≤ 1 km), while the interpretation of the focal mechanism and the fault dimensions show larger variation (Smith and Priestley, 2000; Cockerham and Corbett, 1987; Pacheco and Nábelek, 1988; Savage and Gross, 1995). Based on the published focal mechanisms for the event (Cockerham and Corbett, 1987; Pacheco and Nábelek, 1988; Savage and Gross, 1995; Smith and Priestley, 2000), we assume a pure strike-slip focal mechanism in our simulations.

Following the hypocenter location and the interpreted fault length in Smith and Priestley (2000, 13.9 km), we used a fault width of 11.6 km from the empirical source scaling relations by Leonard (2014) for a M_w6.2 event (moment 2.65 10^{18} Nm), with strike/dip/rake of 150°/55°/-180° and hypocenter location of (-118.4408°, 37.5333°, 10.8 km). Using the Graves and Pitarka

(2016) kinematic rupture generator, we generated three realizations of slip distributions for the defined fault plane, focal mechanism and hypocenter.

Validation results

We generated synthetic seismograms for the Chalfant Valley event, including a GTL tapered to a depth of 700 m below the free surface and a homogeneous dam core with V_S=450 m/s. We found that the three source realizations for the Chalfant Valley event result in similar GOF_{FAS} values, where the model predictions are generally unbiased across the entire examined frequency range. As shown in Fig. 3, right (only showing seed #2), the synthetics are in reasonable agreement with the data recorded at different locations on the LVD in both time and frequency domains up to 7.5 Hz. We note that the Chalfant Valley earthquake validation was carried out using purely elastic rheology, as the PGAs at the dam (about 0.1 g) were deemed insufficient to trigger significant nonlinear soil behavior.

Hilton Creek Fault scenarios

As shown above, our validations for the M_w3.7 and the M_w6.2 1986 Chalfant Valley earthquakes resulted in well-calibrated velocity and attenuation models for the area. In addition, the results of the modeling of the Chalfant Valley event demonstrate that the Graves and Pitarka (2016) kinematic rupture generator is able to create source descriptions that produce ground motions in agreement with data for frequencies up to 7.5 Hz using deterministic simulations. We are therefore ready to perform simulations for scenario earthquakes to assess the stability of the LVD. The Hilton Creek Fault (HCF) is a significant range-bounding normal fault at the eastern side of the Sierra Nevada. Because of its closest distance to the LVD of just 8 km, it has been identified as a possible source for the MCE that could significantly affect the stability of the dam (Lai and Seed, 1985; Chen et al., 2014). Figure 4 (left) shows the model domain for the HCF scenarios, and Table 1 lists the modeling parameters.

Source description

We designed scenarios with M_w6.6 on the HCF with a fault length of 21 km and a width of 13.3 km estimated using the empirical magnitude-area relations by Leonard (2010). The M_w6.6 scenario is one of three cases presented in a study by Chen et al. (2014) for assessing the seismic hazard of the Long Valley Caldera area associated with the HCF. In addition to the M_w6.6 scenario, the study also considered M_w6.5 and M_w6.8 scenarios. However, Chen et al. (2014) pointed out that the fault rupture for the M_w6.8 scenario needs to extend into the Long Valley Caldera with a geometry that violates both geologic and kinematic constraints (Hill and Montgomery-Brown, 2015). Assuming that the hazards to the LVD from the M_w6.5 are smaller, we chose the M_w6.6 scenario to represent the MCE. Based on the estimate of Chen et al. (2014), the recurrence interval for this scenario is 204 years.

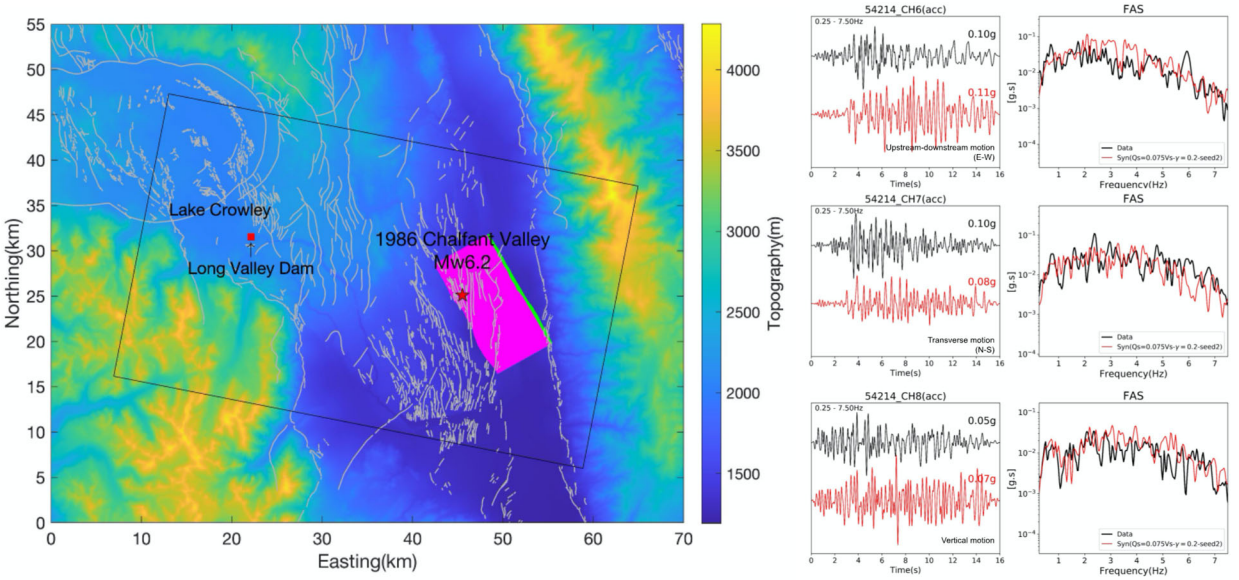

Figure 3: (left) Location map for the simulation domain of the 1986 M_w6.2 Chalfant Valley earthquake (rotated 11.08^o clockwise, model depth 30.75 km). The black box depicts the simulation domain for the earthquake. The pink area shows the surface projection of our finite fault source for the event, the red star shows the epicenter location and the green line depicts the top edge of the fault plane at 2.5 km depth. Green triangles depict station locations. (right) Comparison of data (black traces) and synthetics (red traces) in the time and the FAS domains at sensors located near the downstream base. The synthetic traces were computed with CVM-S, a GTL tapered to 700 m below free surface, and a dam core with V_S=450 m/s (see Fig. 1 for sensor location).

Three different rupture scenarios with the same slip distribution were selected to capture the range of ground motions generated among a southward, northward and a bilateral rupture mode (Fig. 4, right). The hypocenters of all three rupture scenarios are located 6 km down-dip from the top of the fault, all featuring surface ruptures. The source parameters of the HCF scenarios are listed in Table 2.

Elastic and nonlinear properties of materials

For the HCF simulations we used the SCEC CVM-S with a GTL layer tapered to 700 m, $Q_S = 0.075V_S\, f^{0.2}$, and $Q_P = 2Q_S$, the preferred model for the M_w3.7 and Chalfant Valley earthquake validations. In the HCF scenarios, we included nonlinear response of the material in our simulations using the Ducker-Prager yield condition (Drucker and Prager, 1952), where the material behaves purely linear until the yield stress is reached. The implementation of Drucker-Prager plasticity in AWP-ODC is based on the work of Roten et al. (2016). The non-associated Drucker-Prager plasticity is regularized using time-dependent relaxation (Andrews, 2005) via the return map algorithm, following the guidelines of the SCEC/USGS (U.S. Geological Survey) dynamic earthquake rupture code verification exercise (Harris et al., 2011). The Drucker-Prager yield stress *Y(σ)* is defined as

$$Y(\sigma) = max(0, c\ cos\phi - (\sigma_m + P_f)sin\phi)$$

where c is the cohesion, ϕ is the friction angle, P_f is the fluid pressure, and σ_m is the mean (normal) stress ($\sigma_{xx}+\sigma_{yy}+\sigma_{zz}$). The yield stress includes the hydrostatic condition for the fluid pressure, linearly increasing with depth below the water level. The water level inside the dam follows the pre-defined phreatic line shown in Fig. 5. We set P_f=0 for all material above the phreatic line inside the dam.

Table 1: Simulation parameters for the Hilton Creek fault M_w6.6 MCE scenarios

Domain		
Length		28.72 km
Width		40.82 km
Depth		30.68 km
Southwest corner		$-118.84019^o, 37.37252^o$
Northwest corner		$-118.96107^o, 37.72752^o$
Southeast corner		$-118.52681^o, 37.43966^o$
Northeast corner		$-118.64633^o, 37.79500^o$
Rotation angle		14.01^o counterclockwise from north
Spatial resolution		
Maximum frequency		7.5 Hz
Minimum V_S		175 m/s
Points per minimum wavelength		6.66
Grid spacing	3.5 m	4.23 km above sea level to 0.24 km below sea level
	10.5 m	0.22 km to 2.56 km below sea level
	31.5 m	2.49 km to 30.68 km below sea level
Temporal resolution		
Time step		0.00027 s
Simulation time		40 s

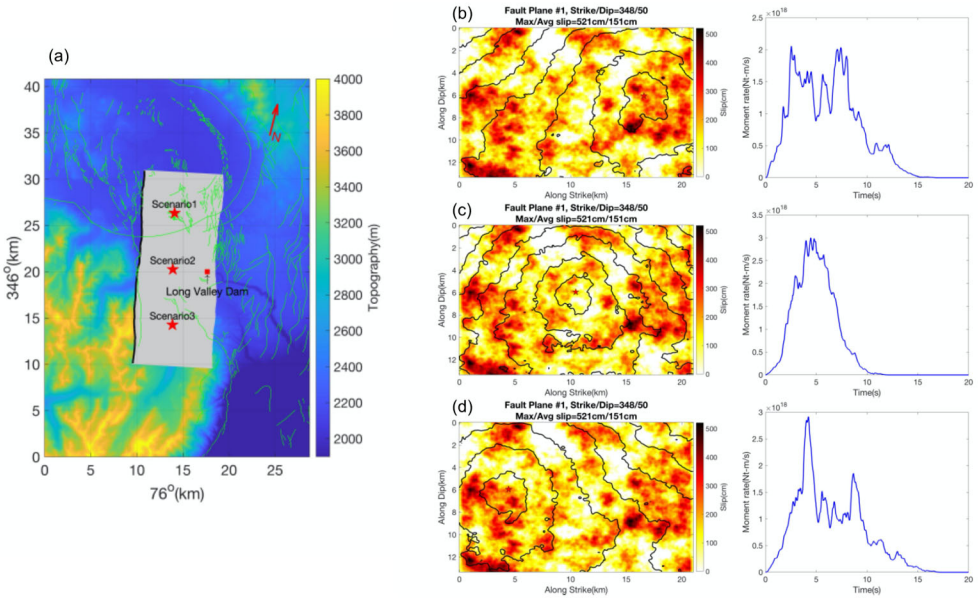

Figure 4: (left) Surface projection of the fault plane for the HCF scenarios, with epicentral locations for the 3 rupture scenarios (stars). (right) Slip (colors) and rupture time contours as well as moment rate histories (on the right of each slip model) for the 3 HCF scenarios with (a) southward, (b) bilateral and (c) northward rupture modes. Red stars on the slip models depict the rupture initiation locations.

Table 2: Source parameters for the Hilton Creek fault M_w6.6 MCE scenarios

Hypocenter location	Southward rupture: $Lon.: -118.7638^o$ $Lat.: 37.6347^o$ $Depth: 4.8$ km Bilateral rupture: $Lon.: -118.7481^o$ $Lat.: 37.5813^o$ $Depth: 4.6$ km Northward rupture: $Lon.: -118.4408^o$ $Lat.: 37.5291^o$ $Depth: 4.3$ km
Focal mechanism[a]	strike/dip/rake=$348^o/50^o/-90^o$
Fault dimensions[b]	Length=21 km Width=13.3 km

[a]: U.S. Geological Survey Quaternary fault and fold database (Haller *et al.*, 2004)
[b]: Leonard (2010)

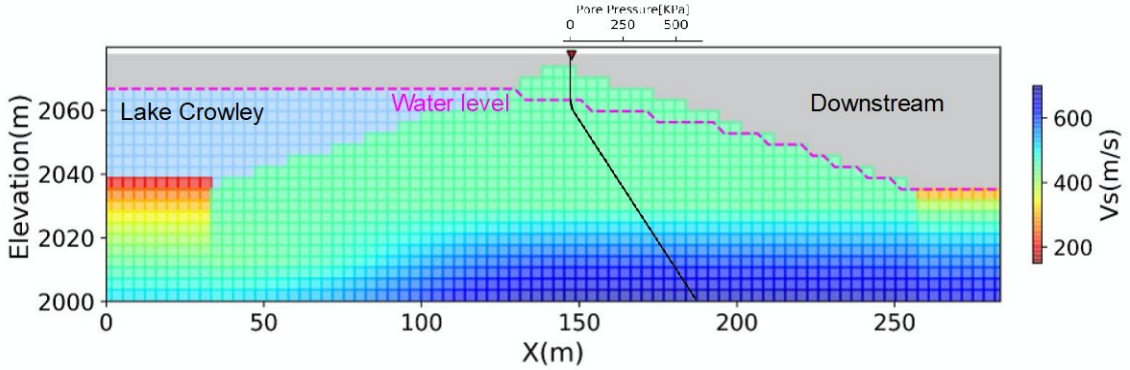

Figure 5. Water level assumed for the nonlinear simulations. The black line shows pore pressure as a function of depth.

For the material within the dam, we assumed a cohesion of 45 kPa and a friction angle ϕ=39º, as was used for the core material as described in Griffiths and Prevost (1988). To determine the yield stress of material off the dam, we adopted the generalized Hoek-Brown failure criterion that conveniently provides the effective cohesion and a friction angle needed for the Drucker-Prager yield condition (Hoek et al., 2002). The Hoek-Brown failure criterion uses a Geological Strength Index (GSI) value for each material. As the mechanical properties of near-surface material are poorly constrained, we make the assumption that GSI is correlated with the local shear wave speed (V_S). The V_S and GSI measurements for rock samples in southern California by Townsend et al. (2021) (Figure 5 of their study) illustrate the relationship between these two quantities. Their analysis shows that (1) rocks with V_S of 200-300 m/s can be characterized by a GSI of 20, (2) GSI of rock samples with V_S of 300-500 m/s fall in the 20-40 range, and (3) rocks with V_S of 1,500 m/s are usually associated with GSI values of ~90. Based on these observations, we first assigned each material into a category based on its S-wave speed, and used the corresponding relationship to compute the GSI value:

$$GSI = \begin{cases} 20 & \text{if } V_S < 300m/s \\ 20 + (V_S - 300) \times \frac{40-20}{500-300} & \text{if } 300m/s \le V_S < 500m/s \\ 40 + (V_S - 500) \times \frac{90-40}{1500-500} & \text{if } 500m/s \le V_S < 1500m/s \\ 90 + (V_S - 1500) \times \frac{100-90}{2000-1500} & \text{if } 1500m/s \le V_S < 2000m/s \\ 100 & \text{if } V_S \ge 2000m/s \end{cases}$$

HCF Scenario Ground Motion Results

We performed both linear and nonlinear simulations for the proposed HCF scenarios, in order to quantify the latter effects. Our results show that the variation of hypocenter location can cause variation of PGA predicted at the crest top by a factor of 1.5. Moreover, the predicted ground accelerations are lower around the downstream base as compared to the dam crest, which demonstrates that the structure of the dam itself amplifies the ground motion by a factor of 2 or more. Given that the southward rupture scenario produces the largest ground motions overall, we focus on this scenario in the following analysis. Fig. 6 illustrates the differences between the linear and nonlinear behavior at the crest center and downstream sensor locations. Notice the strong reduction of the PGAs due to nonlinear response of the material, up to a factor of 2.5, where we predict stronger reductions on the dam as compared to off the dam. These results indicate that nonlinear effects are significant for the ground motions at the LVD.

We illustrate the ground motion response of the dam for the HCF scenarios along a 2D transect across the dam (white line crossing the dam in Fig. 1). Fig. 7 shows that both peak ground velocities (PGVs) and PGAs are amplified along the surface of the dam. The largest PGVs occur at the center crest while the largest PGAs are found in the middle of the downstream face, in particular in the region between the downstream face and the phreatic line. This is expected as the material above the phreatic line is exposed to less nonlinear damping due to lack of fluid pressure, and therefore stronger ground motions. Also notice the 50 m by 20 m zone of elevated PGAs at the base of the dam, right beneath the crest, likely originating from interaction between the dam and the underlying material.

We followed the approach in Ma (2008) to calculate the accumulated strain values, η (Fig. 8). As mentioned in Ma (2008), this quantity is a good representation of actual material damage since it is the cumulative norm of the strain-tensor increments throughout the simulation and thus does not decay through time. The largest cumulative strain occurs in the upstream part of the dam, and areas of the downstream side, near the surface of the upstream and downstream faces, with values up to about 1%. Since the calculation includes all of the dynamic strain, the values in Fig. 8 are expected to be larger than the strain computed from the final permanent displacement field.

Settlement of the dam after a seismic event is crucial information for evaluating dam stability. We computed the relative displacements inside the dam along the 2D transect (Fig. 1) with respect to a control point below the lake as a proxy of the settlements (Fig. 9). Our simulation predicts primarily east-southeastward movement of the material on the upstream face by approximately 10 cm with 3 cm south-southwestward movement near the crest, and very little uplift of displacements with respect to the control point ($< |2|$ cm). The spatial extent of the relative horizontal movement of the LVD is confined to the upper half of the dam. The maximum displacements are about 0.2% of the height of the LVD.

To further assess the response of the LVD during the MCE scenario, we extracted synthetic waveforms every 7 m along a vertical array from the top to the base of the dam (see Fig. 10). As can be seen in the horizontal motions (Figs. 11-12), the high-frequency signal present in both acceleration and velocity waveforms at the bottom of the dam (elevations 2017 m

and 2024 m) gradually vanishes toward the crest top, where the amplitude first decreases between 2017 m and 2045 m, and then increases by nearly a factor of 2 from 2045 m to 2073 m (crest). Figs. 11-13 show acceleration and velocity waveforms, comparison of linear and nonlinear waveforms at the surface, and FAS at three select locations along the array. The FAS show that the elevated energy between 4-6 Hz in the waveforms at 2017 m is absent in the record at 2045 m, while the energy between 2-4 Hz is enhanced in the 2045 m record. The migration of energy from high to low frequency is a result of nonlinear soil behavior. Approaching the crest top, the seismic waves are further amplified by the shape of the dam structure at frequencies above 2 Hz. On the other hand, the vertical ground motions show increased amplitudes approaching the crest top without the high frequency energy depletion found on the horizontal components (Fig. 13). The reason for this is likely that the vertical component primarily contains P-waves which are less likely to trigger nonlinearity. Our results show that the combined effects of nonlinearity and the structure of the dam result in complex ground motion patterns inside the LVD.

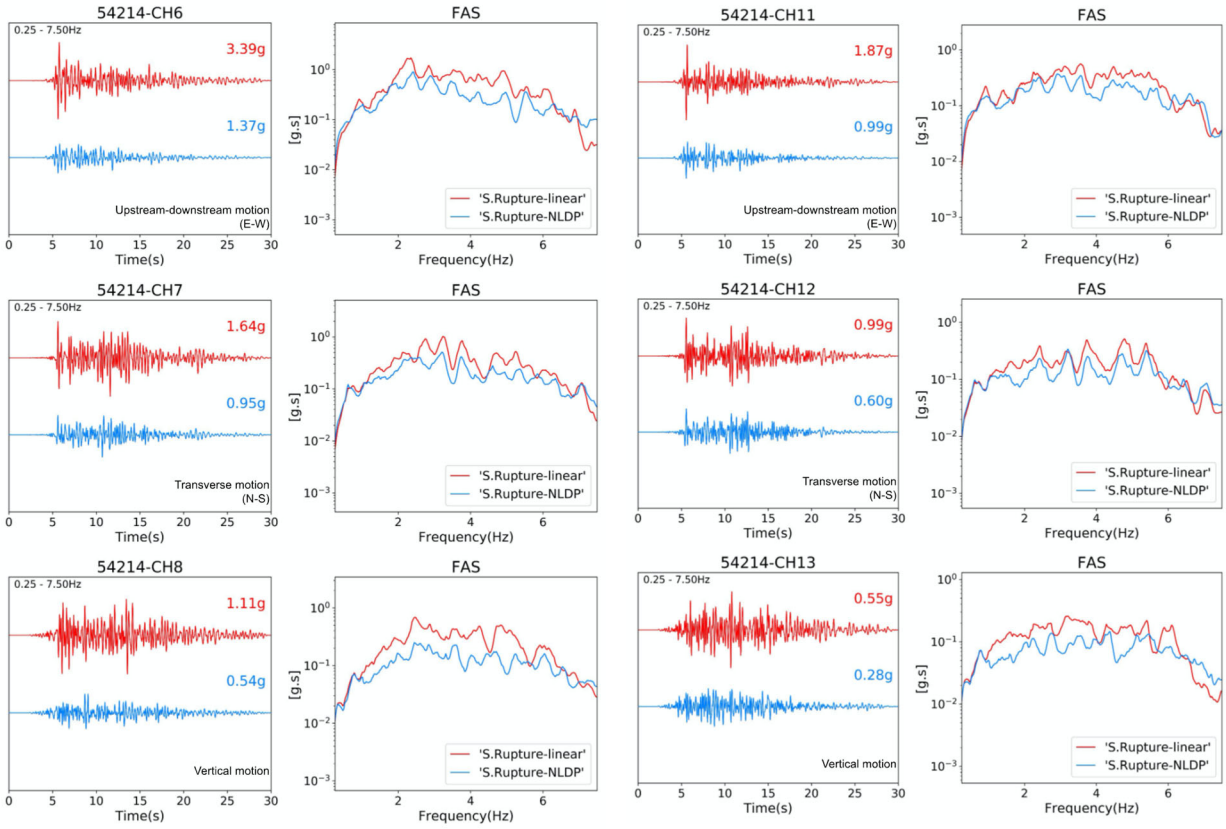

Figure 6: Comparison of linear (red traces) and nonlinear (blue traces) synthetics computed for the southward rupture scenario in the time and FAS domains at sensors located at the (left) crest center and the (right) downstream base (see Fig. 1 for sensor location).

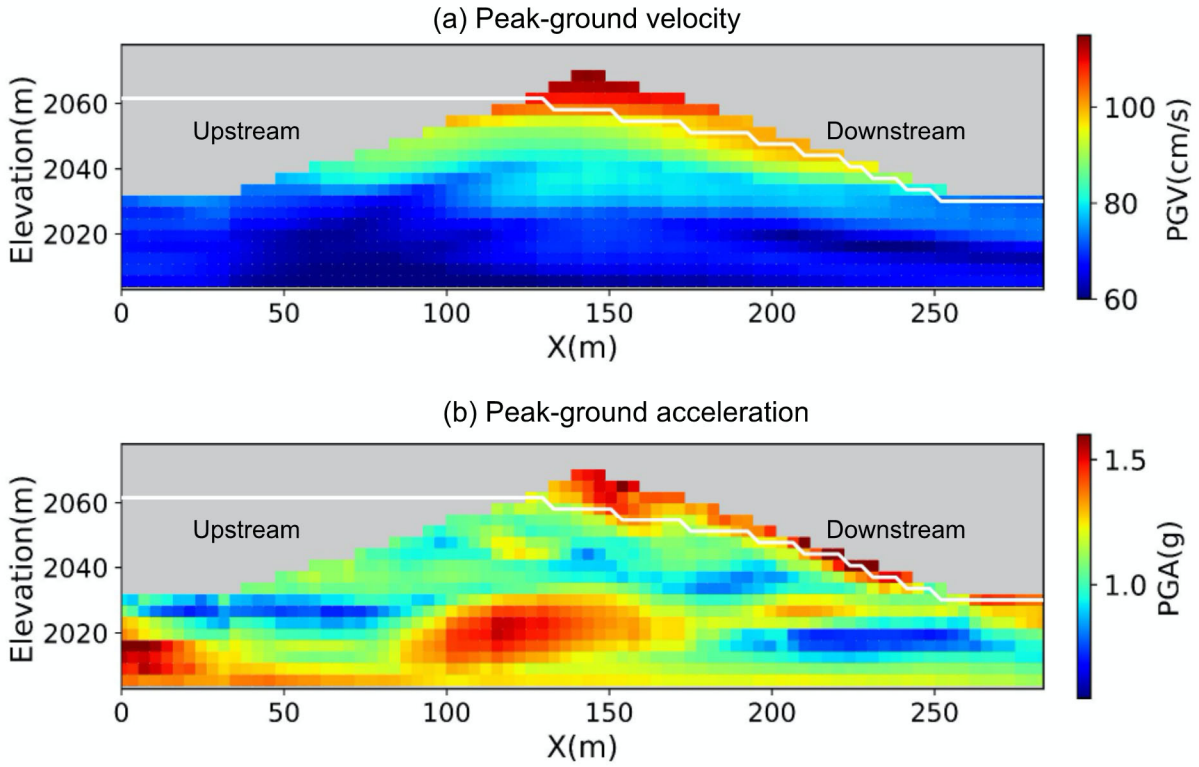

Figure 7. (top) PGV and (bottom) PGA from HCF southward rupture scenario along the transect shown by the white line in Fig. 1.

Discussion and conclusions

The goal of this study is to predict broadband (0-7.5 Hz) ground motions at the LVD for MCE scenarios that are expected to significantly affect the stability of the dam. To ensure that our predicted ground motions are accurate, we first conducted two validations, namely using (1) a 2015 M_w3.7 event with a point source representation and (2) the 1986 M_w6.2 Chalfant Valley earthquake modeled by finite-fault sources. During the first validation we calibrated the tapering depth for the near-surface GTL representation to z_T =700 m, with relatively small differences for z_T between 350-1000 m. Furthermore, we estimated optimal parameters k=0.075 and γ=0.2 for the relation $Q_s(f) = kV_S f^{\gamma}$ (V_S in m/s), as well as for the velocity structure of the dam. Using these calibrated models, we showed that our numerical simulation results can generate 0-7.5 Hz wavefields that are in good agreement with data. Finally, we successfully extended the validation to finite-fault sources for the 1986 Chalfant Valley event using the Graves and Pitarka (2016) kinematic rupture generator.

Very limited direct measurement of the material properties of the LVD is available. A numerical study on the seismic response of the LVD by Yiagos and Prevost (1991) used an exponential function to assign V_S increasing with depth. On the other hand, Griffiths and Prevost (1988) assigned material properties to discrete layers of the dam, including a thin, shallow layer representing the rock shell. Our simulations using the elastic parameters adopted in these studies significantly overpredicted the peak seismic amplitudes on the dam, due to the presence of material with low seismic speed at the shallowest depth. A possible explanation for this

discrepancy is that V_S of the rock shell has increased over time due to variation of the water level (Clariá and Rinaldi, 2007; Dong and Lu, 2016) or internal deterioration. However, future work is needed to address this issue, such as via shallow seismic surveys on the dam.

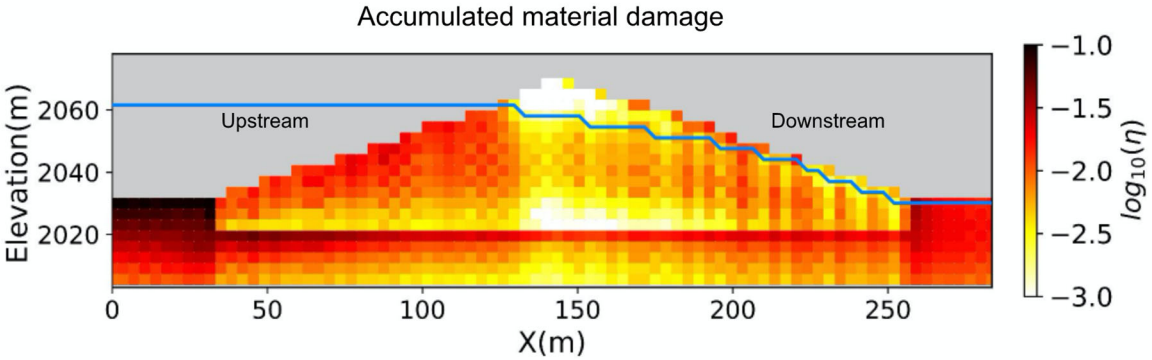

Figure 8. Accumulated material damage in the LVD from the HCF southward rupture scenario.

Based on the validations, we simulated both linear and nonlinear ground motions for a series of MCE rupture scenarios on the HCF, which is located within 8 km of the LVD. The southward rupture scenario generated the largest ground motions around the LVD, with PGAs exceeding 1 g considering the nonlinear rheology. However, plastic behavior in the LVD reduced PGVs and PGAs at the crest top by up to 2.5 times, with a highly complex wavefield. This reduction factor is similar to that found by Roten et al. (2014).

The effects on ground motions due to nonlinearity are expected to vary significantly with the nonlinear properties of the material, as shown by Roten et al. (2014, 2018). For this reason, we performed additional simulations with different cohesion values (c) and friction angles (ϕ) to estimate the variation of predicted ground motions due to uncertainties associated with the nonlinear properties of the LVD. Assuming that the cohesion used in our MCE simulation (c=45 kPa) is an upper bound for compacted clay, we considered two low-cohesion scenarios of c=20 kPa along with friction angles of 20° and 30°. The results of these simulations suggest another 30-40% reduction of horizontal PGAs when using lower cohesion, while the vertical motions appear mostly insensitive to the nonlinear parameters. Future studies should focus on acquiring more robust constraints on nonlinear properties of the studied structures. Finally, the simulations predict relatively small (~ 10 cm) settlements of the dam, with the largest displacements near the surface of the upstream side.

Acknowledgements

This research was supported by the California Geological Survey (Award #1020-006).

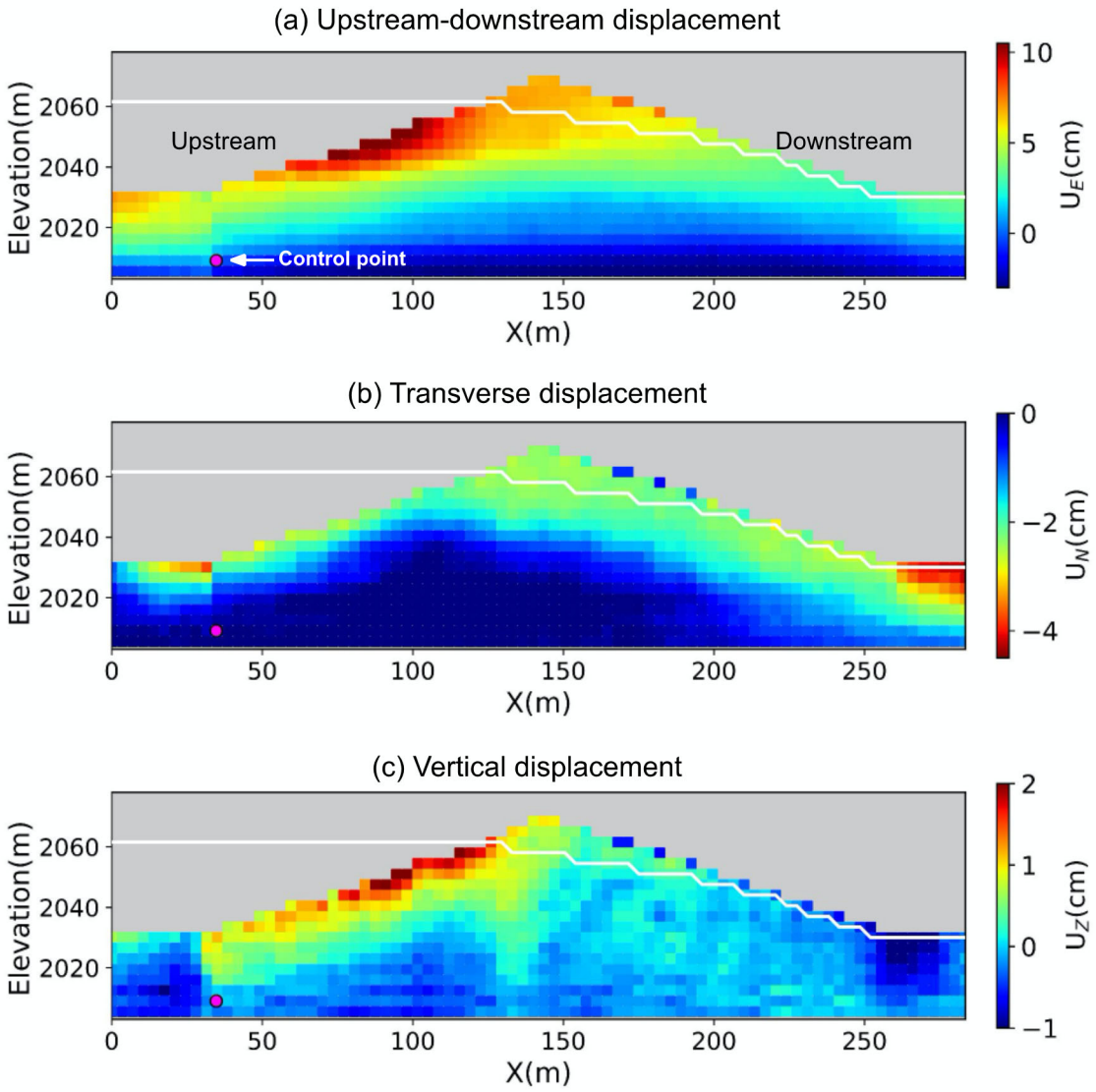

Figure 9. Relative displacement of the material within the LVD with respect to the control point (shown by the magenta dot) from the HCF southward rupture scenario.

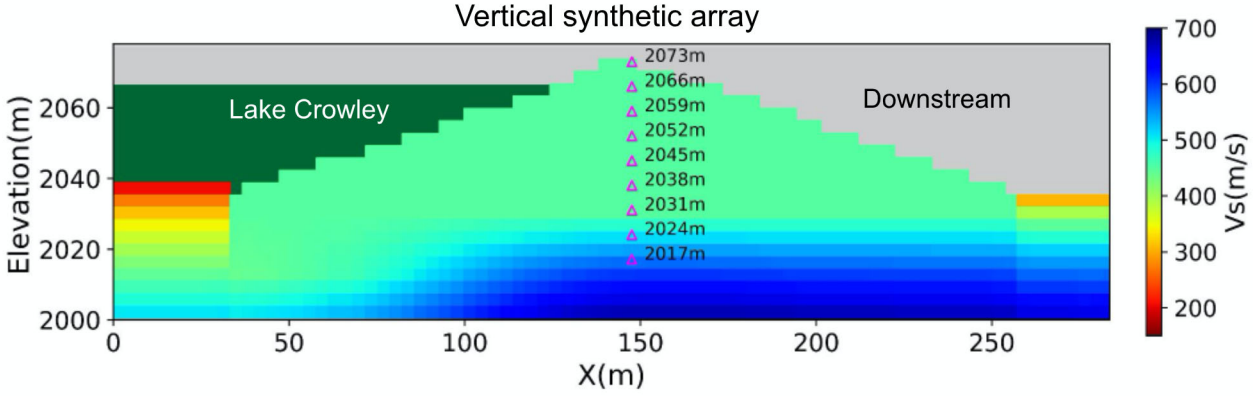

Figure 10. Locations of receivers in the virtual vertical array.

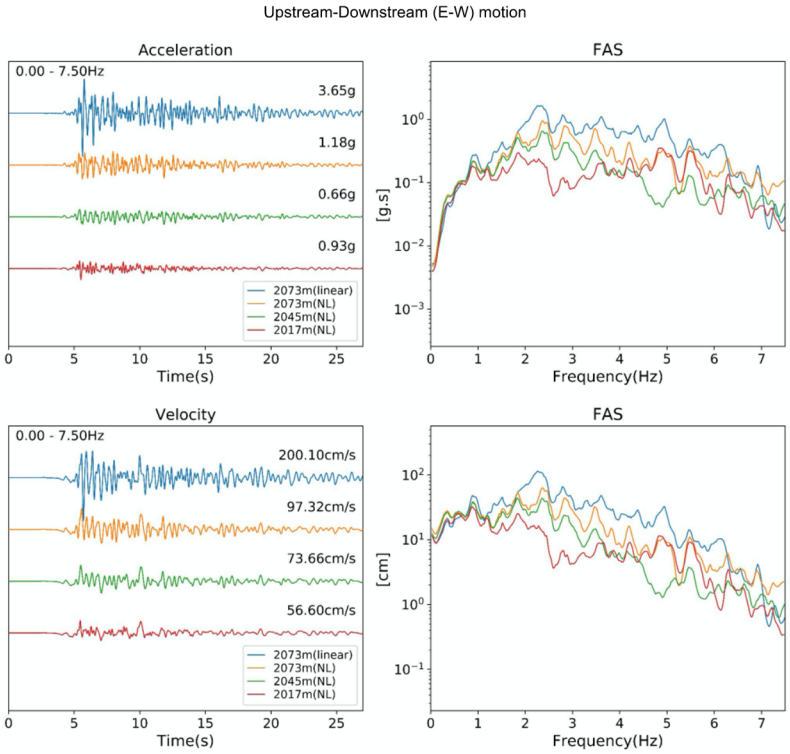

Figure 11. Comparison of nonlinear (top) acceleration and (bottom) velocity waveforms and FAS at stations at elevations of 2017 m (dam bottom), 2045 m, and 2073 m (dam crest surface), with the linear response at 2073 m for comparison (blue).

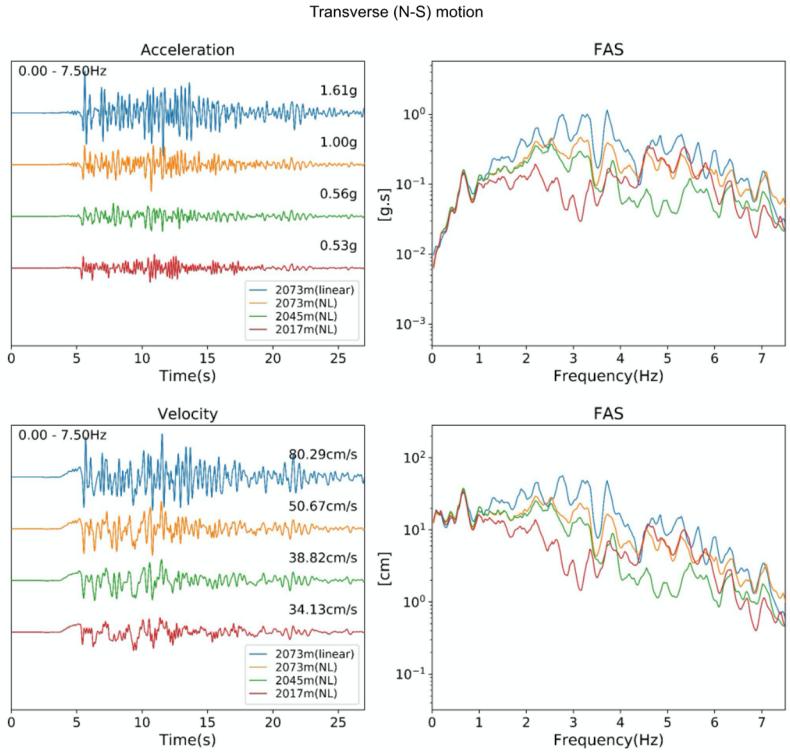

Figure 12. Same as Fig. 11, but for the transverse motion (N-S).

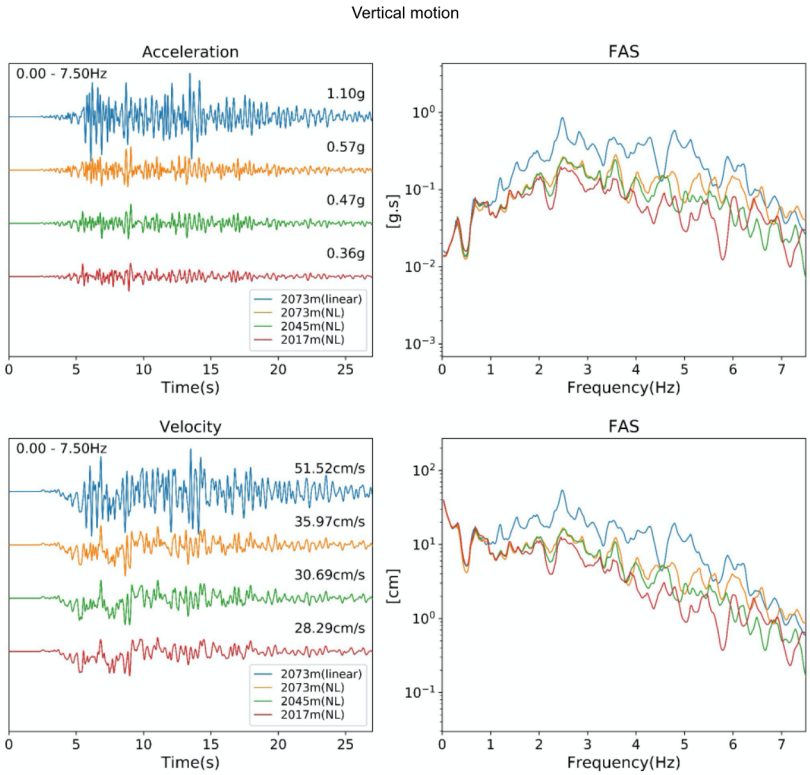

Figure 13. Same as Fig. 11, but for the vertical motion.

References

Andrews, D. J. (2005). Rupture Dynamics with Energy Loss Outside the Slip Zone, Journal of Geophysical Research: Solid Earth 110.B1. ISSN: 2156-2202.

Brune, J. N. (1970). Tectonic Stress and the Spectra of Seismic Shear Waves from Earthquakes, Journal of Geophysical Research (1896-1977) 75.26, pp. 4997–5009. ISSN: 0148-0227.

Chen, R., Branum, D. M., Wills, C. J., & Hill, D. P. (2014). Scenario earthquake hazards for the Long Valley Caldera-Mono Lake area, east-central California (ver. 2.0, January 2018).

Clariá, J. J. and Rinaldi, V. A. (2007). Shear Wave Velocity of a Compacted Clayey Silt, Geotechnical Testing Journal 30.5, pp. 399–408.

Cockerham, R. S. and Corbett, E. J. (1987). The July 1986 Chalfant Valley, California, Earthquake Sequence: Preliminary Results, Bulletin of the Seismological Society of America 77.1, pp. 280–289. ISSN: 1943-3573.

Cui, Y., Poyraz, E., Olsen, K. B., Zhou, J., Withers, K., Callaghan, S., Larkin, J., Guest, C., Choi, D, Chourasia, A., et al. (2013). Physics-based seismic hazard analysis on petascale heterogeneous supercomputers. Page 70 of: Proceedings of SC13: International Conference for High Performance Computing, Networking, Storage and Analysis. ACM.

Dong, Y. and Lu, N. (2016). Dependencies of Shear Wave Velocity and Shear Modulus of Soil on Saturation, Journal of Engineering Mechanics 142.11, p. 04016083. ISSN: 1943-7889.

Drucker, D. C. and Prager, W. (1952). Soil Mechanics and Plastic Analysis or Limit Design, Quarterly of applied mathematics 10.2, pp. 157–165.

Ely, G. P., Jordan, T., Small, P., and Maechling, P. J. (2010). A Vs30-derived near-surface seismic velocity model. AGU Fall Meet., San Francisco, California, 13–17 December, Abstract.

FEMA, P. (2005). Federal Guidelines for Dam Safety: Earthquake Analyses and Design of Dams. FEMA 65.

Graves, R. W. (1996). Simulating Seismic Wave Propagation in 3D Elastic Media Using Staggered-Grid Finite Differences, Bulletin of the Seismological Society of America 86.4, pp. 1091–1106. ISSN: 0037-1106.

Graves, R., and Pitarka, A. (2016). Kinematic Ground-Motion Simulations on Rough Faults Including Effects of 3D Stochastic Velocity Perturbations, Bulletin of the Seismological Society of America, 106(5), 2136-2153. https://doi.org/10.1785/0120160088

Griffiths, D. V., and Prevost, J. H. (1988). Two- and three-dimensional dynamic finite element analyses of the Long Valley Dam. Géotechnique, 38(3), 367-388. https://www.icevirtuallibrary.com/doi/abs/10.1680/geot.1988.38.3.367.

Harris, R. A., Barall, M., Andrews, D. J., Duan, B., Ma, S., Dunham, E. M., Gabriel, A.-A., Kaneko, Y., Kase, Y., Aagaard, B. T., Oglesby, D. D., Ampuero, J.-P., Hanks, T. C., and Abrahamson, N. (2011). "Verifying a Computational Method for Predicting Extreme Ground Motion". In: Seismological Research Letters 82.5, pp. 638–644. ISSN: 0895-0695.

Hill, D. P. and Montgomery-Brown, E. (2015). Long Valley Caldera and the UCERF Depiction of Sierra Nevada Range-Front Faults. In: Bulletin of the Seismological Society of America 105.6, pp. 3189–3195. ISSN: 0037-1106.

Hoek, E., Carranza-Torres, C., and Corkum, B. (2002). Hoek-Brown Failure Criterion-2002 Edition. Proceedings of NARMS-Tac 1.1, pp. 267–273.

Hu, Z., K.B. Olsen, and S.M. Day (2022). Calibration of the Near-surface Seismic Structure in the SCEC Community Velocity Model Version 4, Geophys. Jour. Int., 230, 2183-2198.

Iwan, W. (1967). On a class of models for the yielding behavior of continuous and composite systems, J. Appl. Mech, 34(4):612–617.

Lai, S.S., and Seed, H.B. (1985). Dynamic Response of Long Valley dam in the Mammoth Lake Earthquake Series of May 25–27 1980. Tech. rept. UCB/EERC-85/12. Earthquake Engineering Research Center.

Leonard, M. (2010). Earthquake Fault Scaling: Self-Consistent Relating of Rupture Length, Width, Average Displacement, and Moment Release, Bulletin of the Seismological Society of America 100 (5A), pp. 1971–1988. ISSN: 0037-1106.

Leonard, M. (2014). Self-Consistent Earthquake Fault-Scaling Relations: Update and Extension to Stable Continental Strike-Slip Faults, Bulletin of the Seismological Society of America, 104(6), 2953-2965. https://doi.org/10.1785/0120140087.

Ma, S. (2008). A physical model for widespread near-surface and fault zone damage induced by earthquakes, G3, 9, 11, Q11009, doi:10.1029/2008GC002231 ISSN: 1525-2027.

Nie, S., Wang, Y., Olsen, K. B., and Day, S. M. (2017). Fourth Order Staggered Grid Finite Difference Seismic Wavefield Estimation Using a Discontinuous Mesh Interface (WEDMI), Bull. Seism. Soc. Am. 107(5), 2183-2193.

Olsen, K.B., Day, S.M., and C.R. Bradley (2003). Estimation of Q for long-period (>2 s) waves in the Los Angeles Basin, Bull. Seis. Soc. Am. 93, 627-638.

O'Reilly, O., Yeh, T.-Y., Olsen, K.B., Hu, Z., Breuer, A., Roten, D., and Goulet, C. (2022). A high-order finite difference method on staggered curvilinear grids for seismic wave propagation applications with topography, Bull. Seis. Soc. Am., 112 (1), 3-22, https://doi.org/10.1785/0120210096.

Pacheco, J. and Nábelek, J. (1988). Source Mechanisms of Three Moderate California Earth quakes of July 1986, Bulletin of the Seismological Society of America 78.6, pp. 1907–1929. ISSN: 0037-1106.

Roten, D., Olsen, K. B., Day, S. M., Cui, Y., and Fäh, D. (2014). Expected Seismic Shaking in Los Angeles Reduced by San Andreas Fault Zone Plasticity, Geophysical Research Letters 41.8, pp. 2769–2777. eprint: https://agupubs.onlinelibrary.wiley.com/doi/pdf/10.1002/2014GL059411.

Roten, D., Cui, Y., Olsen, K. B., Day, S. M., Withers, K., Savran, W. H., Wang, P., and Mu, D. (2016). High-Frequency Nonlinear Earthquake Simulations on Petascale Heterogeneous Supercomputers, SC '16: Proceedings of the International Conference for High Performance Computing, Networking, Storage and Analysis, pp. 957–968.

Roten, D., Olsen, K. B., Day, S. M., and Cui, Y. (2018). Quantification of Fault-Zone Plasticity Effects with Spontaneous Rupture Simulations, Best Practices in Physics-based Fault Rupture Models for Seismic Hazard Assessment of Nuclear Installations. Ed. by L. A. Dalguer, Y. Fukushima, K. Irikura, and C. Wu. Cham: Springer International Publishing, pp. 45–67. ISBN: 978-3-319-72709-7.

Savage, J. C. and Gross, W. K. (1995). Revised Dislocation Model of the 1986 Chalfant Valley Earthquake, Eastern California, Bulletin of the Seismological Society of America 85.2, pp. 629–631. ISSN: 0037-1106.

Savitzky, A. and Golay, M. J. (1964). Smoothing and Differentiation of Data by Simplified Least Squares Procedures, Analytical chemistry 36.8, pp. 1627–1639.

Seed, H. B., Makdisi, F. I., and Alba, P. D. (1978). Performance of Earth Dams During Earthquakes, Journal of the Geotechnical Engineering Division 104.7, pp. 967–994.

Small, P., Gill, D., Maechling, P. J., Taborda, R., Callaghan, S., Jordan, T. H., et al. (2017). The SCEC Unified Community Velocity Model Software Framework, Seismological Research Letters, 88(6), 1539-1552. https://doi.org/10.1785/0220170082

Smith, K. D., and Priestley, K. F. (2000). Faulting in the 1986 Chalfant, California, Sequence: Local Tectonics and Earthquake Source Parameters, Bulletin of the Seismological Society of America, 90(4), 813-831. https://doi.org/10.1785/0119990129

Townsend, K. F., Clark, M. K., and Zekkos, D. (2021). Profiles of Near-Surface Rock Mass Strength Across Gradients in Burial, Erosion, and Time, Journal of Geophysical Research: Earth Surface 126.4, e2020JF005694. ISSN: 2169-9003.

Wills, C. J., Gutierrez, C. I., Perez, F. G., and Branum, D. M. (2015). A Next Generation Vs30 Map for California Based on Geology and Topography. *Bulletin of the Seismological Society of America, 105*(6), 3083-3091. https://doi.org/10.1785/0120150105

Withers, K. B., Olsen, K. B., and Day, S. M. (2015). Memory-Efficient Simulation of Frequency-Dependent Q Memory-Efficient Simulation of Frequency-Dependent Q, Bulletin of the Seismological Society of America 105.6, pp. 3129–3142. ISSN: 0037-1106.

Yiagos, A. N. and Prevost, J. H. (1991). Two-Phase Elasto-Plastic Seismic Response of Earth Dams: Applications, Soil Dynamics and Earthquake Engineering 10.7, pp. 371–381. ISSN: 0267-7261.

Zeghal, M. and Abdel-Ghaffar, A. M. (1992). Analysis of Behavior of Earth Dam Using Strong motion Earthquake Records, Journal of Geotechnical Engineering 118.2, pp. 266–277.

USING CSMIP DATA TO DERIVE RELIABLE DYNAMIC RESPONSE PARAMETERS FOR EARTH DAMS IN CALIFORNIA – An Illustrative Example

Ilgac, Makbule[1] and Athanasopoulos-Zekkos, Adda[2]

[1] Post-Doctoral Researcher, University of California, Berkeley, [2] Associate Professor, University of California, Berkeley

Abstract

The purpose of this paper is to improve understanding of the seismic response of earth dams and create a framework for strong-motion data processing that can lead to improvement in the seismic design code provisions and practices for earth dams. CSMIP earthquake recordings from different locations on the dams are assessed to develop Horizontal to Vertical spectral ratios to assess the fundamental resonance frequency of the sites and amplification factors as well as stiffness for the dam and foundation materials which are estimated directly from the recorded motions. The results for Seven Oaks Dam are presented as an illustrative example.

Introduction

Earthen dams play a very important role in flood defense, while many are also used for water supply, irrigation, power generation, transportation, and sediment retention among other roles. The state is also heavily reliant on the nearly 1500 dams, the vast majority of which are earthen, that play a crucial role in California's water management. The potential dam failure modes related to earthquakes and the associated seismic hazard of ground shaking are often the driving design criteria for new dams in earthquake-prone regions, and the primary concern when evaluating the safety of many existing dams. California is an active tectonic region characterized by high seismic hazards. There is a unique opportunity to utilize the CSMIP network's strong motion data to improve our understanding of the dynamic response of earth dams in California on a broader scale and beyond limited individual case studies, and therefore make our seismic hazard assessment more rigorous. The FEMA guidelines for Earthquake Analysis and Design of Dams (FEMA, 2005) do provide a general framework for how to approach this and minimum requirements, however, leave many aspects to the judgment of the engineer. The US Bureau of Reclamation provides more detail in the recent Design Standards for Embankment Dams (USBR, 2015); however, the main emphasis is on liquefaction assessment and permanent slope displacements, and not on best practices for site response and dynamic analyses.

Our objective in this proposed study is to improve our understanding of the seismic response of earth dams and create a framework for strong-motion data processing that can lead to improvement in the seismic design code provisions and practices with respect to earth dams. Specifically, it is proposed to use CSMIP earthquake recordings from different locations on the dams (toe, crest, abutment, etc.) to develop Horizontal to Vertical (H/V) spectral ratios (Nakamura, 1989) for each dam location. Stiffness (G_{max}) and damping parameters (d) for the dam and foundation materials will be estimated directly from the recorded motions and

simplified site response analyses will also be conducted to compare the computed amplification with the one observed in the recordings.

There are currently no explicit guidelines focusing on the evaluation of the dynamic response of dams. Engineers rely on published works in the literature for simplified procedures and guidance on analyzing the dynamic response of earth dams, and in doing so, often must qualitatively assess the site's fundamental period, the dynamic properties of the dam materials (e.g., G_{max}) and any expected amplification (site) effects. This literature also typically focuses on landmark cases of dam response following large earthquakes but does not provide a consistent framework that can be applied to a wide range of earth dams (small to large and in different geologic settings). It is aimed to first-time leverage a large dataset available through CSMIP to explore the general applicability of the proposed technique for a range of dam sites. Within the confines of this study, an illustrative dam site Seven Oaks Dam is selected to present the methodology to assess the HVSR curves to determine the resonance frequency of the site and amplification factors, and dynamic properties of the dam materials (e.g., G_{max}). A comparison of the results with 1-D equivalent linear site response analysis will be shown.

In subsequent analysis, this approach will be applied to more than 40 dam sites in California to understand the dynamic response of dams which is not the scope of this paper.

Background Information on Dynamic Response of Earth Dams

The seismic response of earth dams is admittedly rather complicated. Therefore, advanced dynamic analysis methods need to be employed to capture dams' actual behavior under seismic conditions. Such methods and associated advanced constitutive models do exist nowadays, but they need to be further developed and validated against known case studies so that reliable results can be obtained for further dam analysis and design. For example, Mejia and Dawson (2008) showed that when analyzing the dynamic response of the Seven Oaks Dam as part of a CSMIP Data utilization study, considerable uncertainties are associated with the assumed analysis inputs. The main sources of uncertainty appear to lie in the assumed seismic wave field at the site during the earthquakes, and the properties of the embankment and foundation materials. The uncertainties in the shear moduli of the embankment materials at small strains would be considerably reduced through in-situ measurements of the shear and compression wave velocities of the embankment materials.

The vibrations of earth dams in the upstream-downstream direction were initially investigated by Ambraseys (1960a) using the shear beam method. Dakoulas and Gazetas (1985) studied the crest amplification of a dam for various damping ratios and showed its dependency on the dam's fundamental period. It has generally been shown that dams built in narrow deep canyons behave in a stiffer manner than dams built in wider canyons. The stiffening effect of narrow canyon results in smaller natural periods. The effect of the three-dimensional geometry of the dam-canyon system was firstly studied in the 1950s by Hatanaka (1952) and Ambraseys (1960b). These authors concluded that canyon effects are negligible for dams in rectangular canyons with dam length-to-height ratios, $L/H > 4$. Later in-depth investigations include the work of Dakoulas and Gazetas (1986, 1987) using the shear beam method and Mejia and Seed (1983) using the finite element method.

With respect to inhomogeneity in dams, previous studies have shown that inhomogeneity affects the dynamic response of earth dams. It has been reported (e.g., Gazetas, 1987) that the effects of inhomogeneity are less pronounced if nonlinear material behavior is considered.

The methods for analyzing the dynamic response of earth dams fall into three main categories: (a) pseudo-static methods to assess the stability of the earth dam (i.e., the dam slope), (b) sliding block analysis methods which calculate the permanent displacements and (c) methods evaluating the dynamic response of the whole dam structure, such as the shear beam approach. However, advanced numerical techniques, such as the finite element method have the capacity to satisfy all the analysis objectives: stability, displacements, and dynamic response. Numerical methods have been formulated to model the nonlinear material behavior of the dam materials, which cannot be calculated analytically. Various methods have been developed over the years and these range from the simple numerical shear beam method up to the sophisticated nonlinear coupled dynamic analysis including consideration of reservoir-dam interaction effects. However, it is important to note, that as the methods become more sophisticated and are able to capture more aspects of the soil's response, the nonlinearity as well as the reservoir-dam interaction during shaking, the analyses become computationally intensive (and by extension, time-consuming). As a result, in practice a much smaller number of input ground motions are being used for the dynamic analyses, not allowing for the investigation of the impact of the input ground motion parameters.

Site effects associated with local geologic conditions constitute an important part of any seismic hazard assessment. Many examples of catastrophic consequences of earthquakes have demonstrated the importance of reliable analysis procedures and techniques in earthquake hazard assessment and in earthquake risk mitigation strategies. The fundamental period of the site, as well as the dam itself, are parameters that to a large degree control the dynamic response of the earth dam. The H/V spectral ratio method is an experimental technique to evaluate some characteristics of soft-sedimentary (soil) deposits. Due to its relative simplicity, both for the survey and analysis, the H/V technique has been frequently adopted in seismic microzonation investigations and has shown to be useful to estimate the fundamental period of soil deposits. However, measurements and analysis should be performed with caution. The main recommended application of the H/V technique by SESAME (2000) is to map the fundamental period of the site and help constrain the geologic and geotechnical models used for numerical computations. In addition, this technique is also useful in calibrating site response studies at specific locations. The European research project SESAME (Contract. No. EVG1-CT-2000-00026) conducted some years ago, provides guidelines for data processing and interpretation.

The H/V spectral ratio (i.e., the ratio between the Fourier amplitude spectra of the horizontal and the vertical component of microtremors was first introduced by Nogoshi & Igarashi (1970 and 1971) and became more widespread by Nakamura (1989, 1996, 2000). These authors have pointed out the correlation between the H/V peak frequency and the fundamental resonance frequency of the site and proposed to use the H/V technique as an indicator of the subsurface conditions. Since then, a large number of experiments (Lermo & Chavez-Garcia 1993; Gitterman et al. 1996; Seekins et al. 1996; Fah et al. 2001) have shown that the H/V procedure can be successfully applied to identifying the fundamental resonance frequency of sedimentary deposits. These observations were supported by several theoretical 1-D

investigations (Field & Jacob 1993; Lachet & Bard 1994; Lermo & Chavez-Garcia 1994; Wakamatsu & Yasui 1996; Tokeshi & Sugimura 1998), that have shown that noise synthetics computed using randomly distributed near-surface sources lead to H/V ratios that sharply peak around the fundamental S-wave frequency when the surface layer exhibits a sharp impedance contrast with the underlying stiffer formations. There is still ongoing research into the applicability of this technique to evaluating site amplification (Bard 1998; Bour et al. 1998; Mucciarelli 1998; Al Yuncha & Luzon 2000; Maresca et al. 2003; Rodriguez & Midorikawa 2003). If the shape of the H/V curves is controlled by the S-wave resonance within the sediments then both H/V peak frequency and amplitude may be directly related to the soil transfer function (in terms of fundamental resonance frequency and site amplification factor (Nakamura (1989, 2000. On the other hand, if the shape of the H/V curves is controlled by the polarization of fundamental Rayleigh waves (Lachet & Bard 1994; Kudo 1995; Bard 1998; Konno & Ohmachi 1998; Fah et al. 2001), then only an indirect correlation between the H/V peak amplitude and the site amplification may exist. Finally, combining H/V information with data from active source methods (SASW, MASW, etc.) provides additional constraints to the inversion problem needed for evaluating the shear wave velocity profile (V_s) (Wood et al. 2014).

The seismic recordings of vertical arrays of accelerometers have also been used for extracting shear stress-strain loops of soil which are then utilized for estimating the corresponding values of shear modulus, G, and damping, D, as a function of soil shear strain. The first applications of this technique have been reported by Abdel-Ghaffar and Scott (1979a, b), Lin and Chao (1990), Koga and Matsuo (1990), and Lin (1994). The first application of extracting shear stress-strain loops from the seismic recordings of the Superstition Hills 1987 earthquake at the Wildlife Refuge (Imperial County, California site) was made by Zeghal and Elgamal (1994) which forms the basis of the analysis discussed in this study.

Methodology

H/V spectral ratios will be used for evaluating the fundamental site period as well as the fundamental period of the dam. The effect of distance and depth of vibration source on the H/V ratios due to different earthquakes will also be investigated. Once the H/V ratios are determined, they can be used with near real-time generated shake maps, to predict locations of expected high-motion amplification and provide an immediate assessment of likely damage to the dam. This will be the first time this approach is implemented at the State level scale. This will allow for documentation of the accuracy of these methods depending on shaking intensity and dam characteristics, as well as assess the impact of the estimated fundamental site period on-site amplification.

The proposed research approach includes processing Ground Motion Recordings and calculations of H/V ratios. Firstly, all relevant recordings at the dam sites of interest work are collected and processed to develop Horizontal to Vertical (H/V or HVSR) spectral ratios for the dam location. Strong ground motion data is collected and band-filtered with the Butterworth filter to eliminate the low and high frequencies that are associated with noise and eventually earthquake-induced frequency levels will remain. The H/V spectral ratios will be used for evaluating the fundamental site period as well as the fundamental period of the dam. Lermo and Chavez-Garcia (1993) have shown that it is possible to identify a dominant period (i.e.,

resonance frequency) and local amplification using recordings from only one station if the site effects are due to simple geology (e.g., horizontal stratification). According to the method, records are transformed in the frequency domain, and smoothed, and the geometric mean of the horizontal components is divided by the vertical component. If there is a strong velocity contrast in the subsurface (e.g., an impedance ratio greater than ~2), a peak will be observed in the frequency-spectral ratio domain that will be equal to the fundamental site period. The effect of distance and depth of vibration source on the H/V ratios will be studied for the cases where recordings from multiple earthquakes are available. Once the H/V ratios are determined, they can potentially be used with near real-time generated shake maps, to predict locations of expected high-motion amplification and provide an immediate assessment of likely damage to the dam.

Our vision is to use the ground motion recordings at the earth dam sites that are part of the CSMIP database (and supplement them with a few more from the PEER NGA West 2 updated database) to develop such an approach. Specifically, our approach will aim to compute and analyze the H/V spectral ratios of recordings and investigate the resonance frequencies as well as the amplification characteristics of these sites. The procedure to calculate the resonance frequencies is summarized in Figure 1.

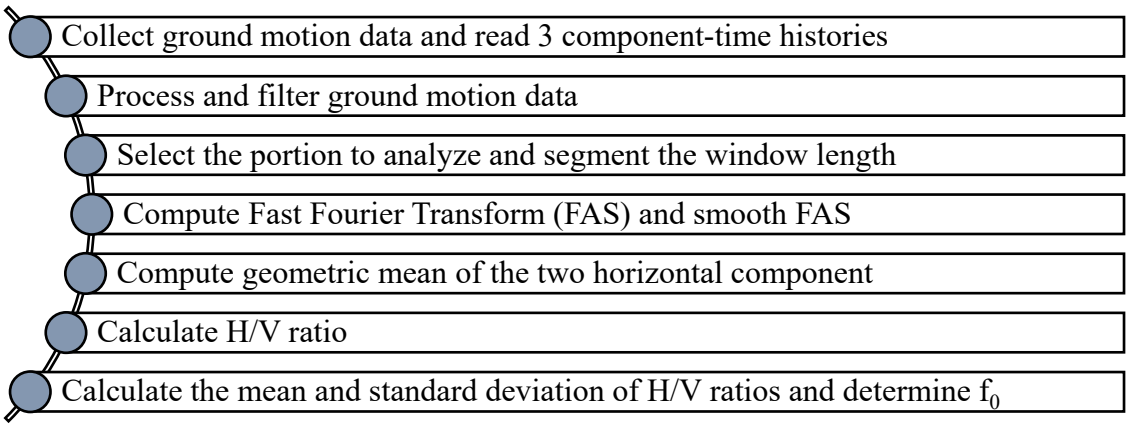

Figure 1. Flowchart of the procedure for calculating H/V ratios at strong ground motion stations.

The seismic recordings of vertical arrays of accelerometers will be used for extracting shear stress-strain loops of soil which are then utilized for estimating the corresponding values of shear modulus, G, and damping, D, as a function of soil shear strain following the procedure by Abdel-Ghaffar and Scott (1979a, b), Lin and Chao (1990), Koga and Matsuo (1990) and Lin (1994). The procedure to calculate stress-strain loops is summarized in Figure 2.

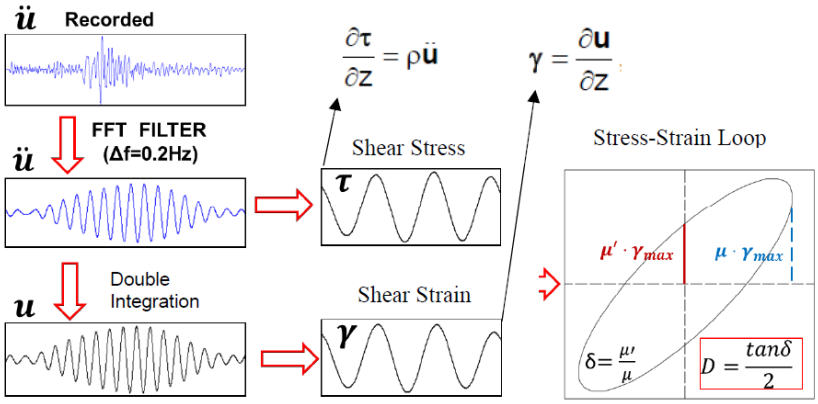

Figure 2. Overview of the steps used for developing the shear stress-strain loops from earthquake recordings

California Strong Ground Motion Network

Given the new recordings following some recent earthquakes in California (e.g., Ridgecrest sequence), and the upcoming updates to the CESMD database as presented during the 2019 annual COSMOS Technical Session (Haddadi, H., 2019), all relevant motions to our analyses in CESMD database is investigated. Figure 3 presents the location of the 40 dams in the State of California and Table 1 list these dams that we intend to include in future studies.

Figure 3. Map of the State of California with the locations of the dam sites that will be included in this study.

Table 1. Stations located at dams in the Center for Engineering Strong Motion Data (CESMD) Strong-Motion Database

Stations located at dams in the CESMD	
Anderson Dam	Los Gatos - Lenihan Dam
Big Pine - Tinemaha Dam	Martis Creek Dam
Bouquet Canyon Reservoir Dam No. 1	Monterey Park; Garvey Reservoir

Brea Dam	Murietta Hot Springs; Skinner Dam
Brea; Orange County Reservoir	New Hogan Dam
Briones Reservoir - Briones Dam	Palos Verdes Reservoir
Buchanan Dam	Paradise - Magalia Dam
Camanche Reservoir - Camanche Dam	Pomona - Puddingstone Dam
Carbon Canyon Dam	Prado Dam
Del Valle Dam	Redlands; Seven Oaks Dam
Fairmont Reservoir - Fairmont Dam R. Abut	Riverside - Mathews Dam, Dike 1
Hayfork - Ruth Lake Dam [Mathews Dam]	Riverside - Mathews Dam, Main Dam
Hidden Dam	San Antonio Dam
Indian Creek Dam - Crest	San Miguel - San Antonio Dam
Lake Crowley - Long Valley Dam	Santa Fe Dam
Lake Edison - Vermilion Dam	Sierra Madre - Cogswell Dam
Lake Isabella Dam	Terminus Dam
Lake Mathews Dam	Thousand Oaks - Wood Ranch Dam & Dike
Lake Piru - Santa Felicia Dam	Warm Springs Dam
Lake Success Dam	Whittier Narrows Dam

An Illustrative Case Study on Seven Oaks Dam

Within the confines of this study, Seven Oaks Dam is selected as an illustrative example to assess the H/V spectral ratios and subsequently estimate the resonance frequency (f_0) and amplification factors. This methodology will later be applied to a larger dataset and will be used with near real-time generated shake maps, to predict locations of expected high-motion amplification and provide an immediate assessment of likely damage to the dam.

Background Information on Seven Oaks Dam

Seven Oaks Dam is a flood control dam constructed by the U.S. Army Corps of Engineers, Los Angeles District. The dam is located on the Santa Ana River in Redlands, San Bernardino County, California (34.1105N, 117.0985W). The dam has a structural height of 640 feet, and a crest length of 2,760 feet earth-rockfill dam (Mejia and Dawson, 2008). Figure 4 presents the plan view of Seven Oaks Dam along with the location of the accelerographs as given by Mejia and Dawson (2008). There are 6 three-component accelerographs of the ground motions (2 horizontal and 1 vertical) on Seven Oaks Dam. These accelerographs are located on the right abutment, right crest, center crest (surface and downhole at -152 ft), intake structure, gate chamber, and downstream (surface and downhole at -53 ft).

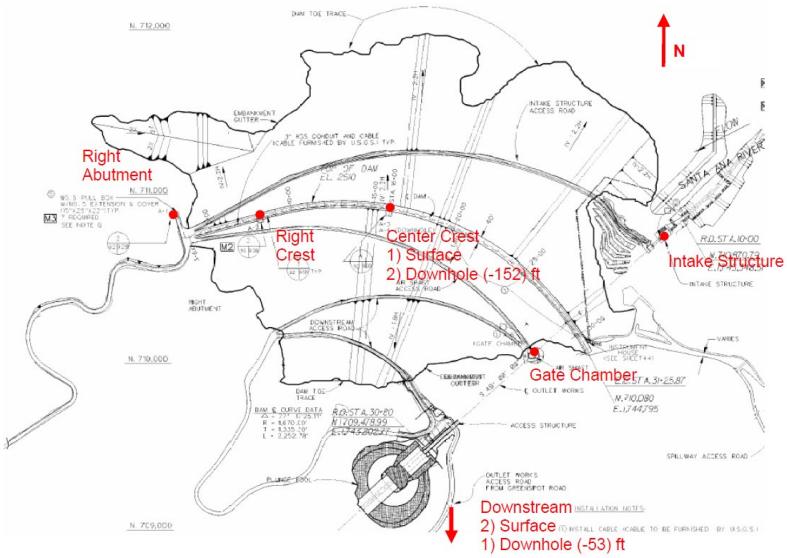

Figure 4. Plan view of Seven Oaks Dam along with the location of the accelerographs (Mejia and Dawson, 2008).

Figure 5 presents the site conditions and the location of the accelerographs located at the surface and at 53 ft at the downstream site as given by Mejia and Dawson (2008). The site consists of alluvium in the upper 37 ft underlaid by weathered bedrock which has a shear wave velocity of 3000 ft/s. The downstream site of Seven Oaks Dam represents free field conditions, and 15 digitally available records enable a more accurate estimation of the resonance frequency of the site hence the calculation of HVSR will be illustrated for the downstream site.

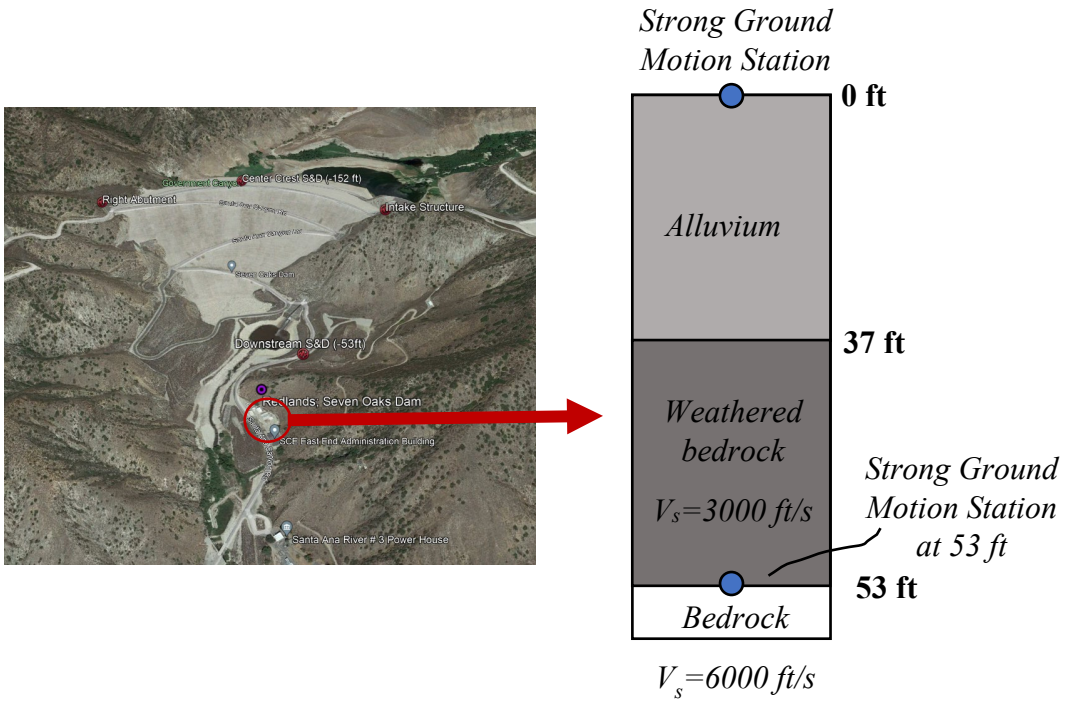

Figure 5. Site conditions at the downstream site (after Mejia and Dawson, 2008)

Ground Motion Recordings

Seismographs at Seven Oaks Dam downstream site recorded 17 earthquakes which are reported in the CSMIP network. These events are listed in Table 2.

Table 2. List of the events recorded at the Seven Oaks Dam site.

EQ#	Earthquake Name	Time USGS	M_w USGS	Epi_{dst} (km)
1	Hector Mine Earthquake	1999-10-16 09:46:44 (UTC)	7.1	93.1
2	Anza Earthquake	2001-10-31 07:56:16 (UTC)	5	86.9
3	Big Bear-02	2001-02-10 21:05:05 (UTC)	4.7	-
4	Big Bear City Earthquake	2003-02-22 12:19:10 (UTC)	5	31.5
7	San Bernardino Earthquake	2009-01-09 03:49:46 (UTC)	4.5	19
9	Ridgecrest Earthquake	2019-07-04 17:33:49 (UTC)	6.5	180.8
10	Searles Valley Earthquake	2019-07-05 11:07:53 (UTC)	5.4	188.1
11	Searles Valley Earthquake	2019-07-06 03:16:32 (UTC)	5	183.9
12	Searles Valley Earthquake	2019-07-06 03:23:50 (UTC)	4.8	193.1
13	Ridgecrest Earthquake	2019-07-06 04:13:07 (UTC)	4.8	170.2
14	Little Lake Earthquake	2019-07-06 04:18:55 (UTC)	5.4	206.7
15	Little Lake Earthquake	2019-07-06 04:19:54 (UTC)	3.8	205.1
16	Searles Valley Earthquake	2019-07-06 08:32:57 (UTC)	4.6	173.2
17	Little Lake Earthquake	2019-08-22 20:49:50 (UTC)	4.9	207
18	Barstow Earthquake	2020-01-25 03:03:34 (UTC)	4.6	110.1
19	Anza Earthquake	2020-04-04 01:53:18 (UTC)	4.9	88
20	Searles Valley Earthquake	2020-06-04 01:32:11 (UTC)	5.5	169.6

Most earthquakes are moderate events with a moment magnitude range of 4.0-7.1 with an epicentral distance of 19 to 207 km. The epicenter of the events along with the Seven Oaks Dam location is shown in Figure 6.

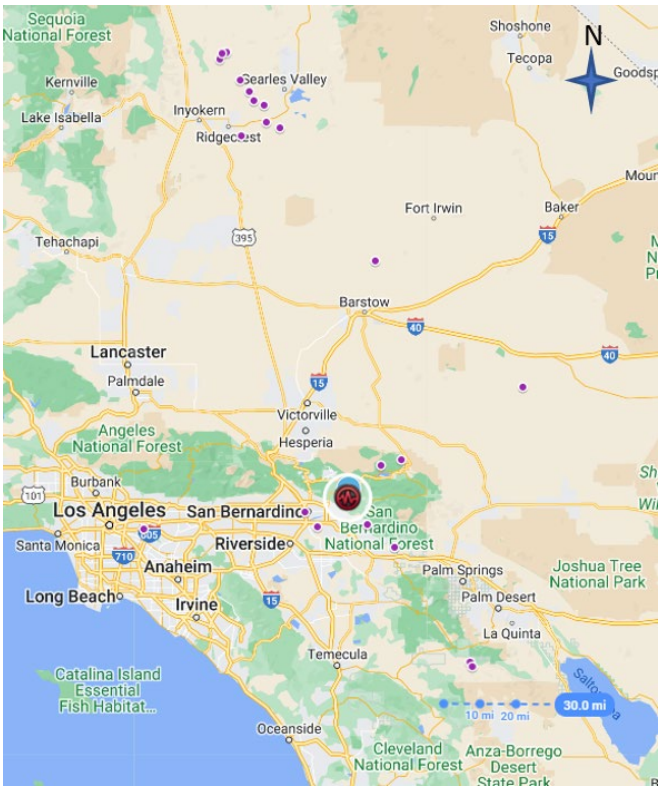

Figure 6. Epicenters of the earthquakes recorded at Seven Oaks Dam along with the location of the dam.

Among those recorded events, only a limited number of data is available at the crest on the other hand a large number of data is available at the downstream site. Considering the uncertainties involved in H/V ratio analyses to determine the resonance frequency of sites, it is more convenient to assess the downstream site since a large number of data can be used in the subsequent analysis. CSMIP network provided filtered, and baseline-corrected strong ground motion data, and most of these recorded are band-passed filtered by using Butterworth filtering to frequency levels of 0.3-33 Hz. Those motions are used directly in the analysis to assess the H/V ratio. For a limited number of strong ground motion data, only the raw recordings were available, and these are filtered by using Seismo Signal 2022 software. Table 3 presents a summary of the recorded ground motions the at Seven Oaks Dam site and the maximum ground acceleration for 3 components. The maximum peak ground acceleration (geometric mean of the two-horizontal components) of the recorded ground motions at downstream sites varies between 0.0007 to 0.0626 g.

Table 3. List of the events and corresponding maximum ground acceleration values recorded at Seven Oaks Dam.

Location of the Accelerograph		a_{max} (g)																				
	EQ#	1	2	3	4	5	6	7	8	9	10	11	12	13	14	15	16	17	18	19	20	21
Project Office	**360°**	0.0505						0.1545														
	90°	0.0631						0.1171														
	UP	0.0286						0.0006		0.0704												
Center crest surface	**360°**							0.1544														
	90°							0.1171														
	UP							0.0507														
Center crest downhole	**360°**							NA														
	90°							0.0270														
	UP							0.0322														
Right crest	**360°**																					
	90°																					
	UP																					
Right abutment	**360°**			0.0047	0.0130			0.0588														
	90°			0.0071	0.0113			0.0344														
	UP			0.0042	0.0082			0.0230														
Tunnel chamber	**360°**							0.0164														
	90°							0.0096														
	UP							0.0078														
Downstream surface	**360°**		0.0120	0.0417	0.0407			0.0557		0.0089	0.0011	0.0006	0.0006	0.0011	0.0019	0.0019	0.0010	0.0012	0.0024	0.0063	0.0037	
	90°		0.0081	0.0608	0.0313			0.0704		0.0085	0.0012	0.0008	0.0010	0.0009	0.0022	0.0022	0.0013	0.0012	0.0026	0.0067	0.0043	
	UP		0.0055	0.0173	0.0115			0.0211		0.0039	0.0005	0.0003	0.0004	0.0004	0.0013	0.0013	0.0005	0.0005	0.0009	0.0027	0.0017	
Downstream downhole	**360°**							0.0291														
	90°							0.0236														
	UP							0.0080														

Calculation of H/V (or HVSR) curves

The method to estimate the H/V (or HVSR) was proposed by Nakamura (1989) to interpret microtremor measurements. As mentioned before, the method is also applied to strong ground motion recordings (e.g., Lermo & Chavez-Garcia 1993, etc.) to implement the H/V procedure to identify the fundamental resonance frequency of sedimentary deposits.

The availability of free software “Geopsy” (Wathelet et al, 2020) enables a practical assessment of H/V ratios which is used in this study. Figure 7 presents the 3-component acceleration time histories recorded at the downstream site which are used to estimate the H/V ratios at the site and the processing of these recordings is achieved using “SeismoSignal” 2022 software. Following the procedure described above, for each earthquake recording, a different time window is selected to capture the intense part of the S-waves in the ground motion and this window is cosine tapered (5%) and Fourier transformed by using Geopsy software. The Fourier Amplitude spectra (FAS) are smoothed with the Konno and Ohmachi (1998) algorithm with a b-value of 40 using a logarithmic equation. The geometric mean of the horizontal components is calculated and divided by the vertical component.

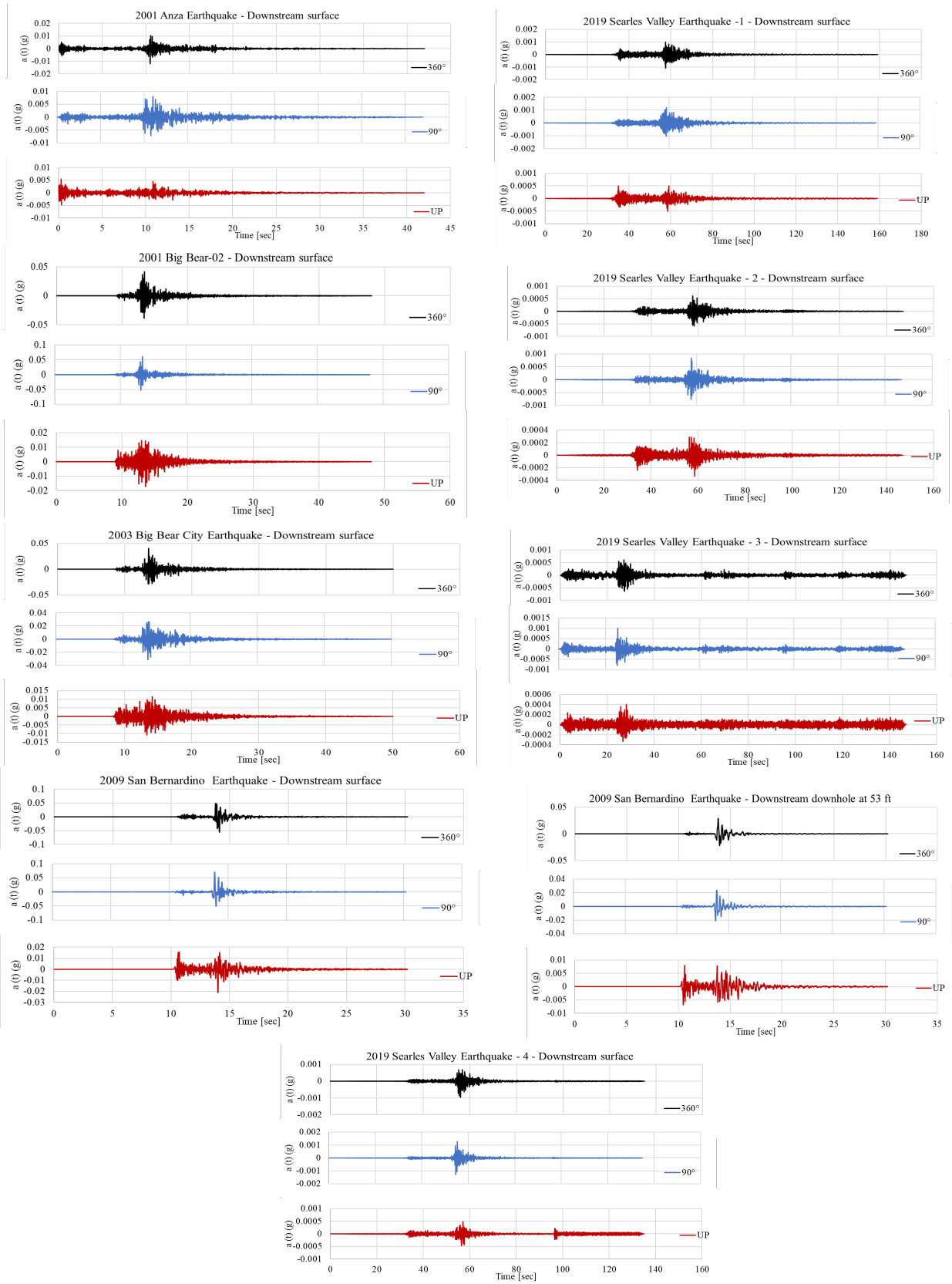

Figure 7. Acceleration time histories recorded downstream site

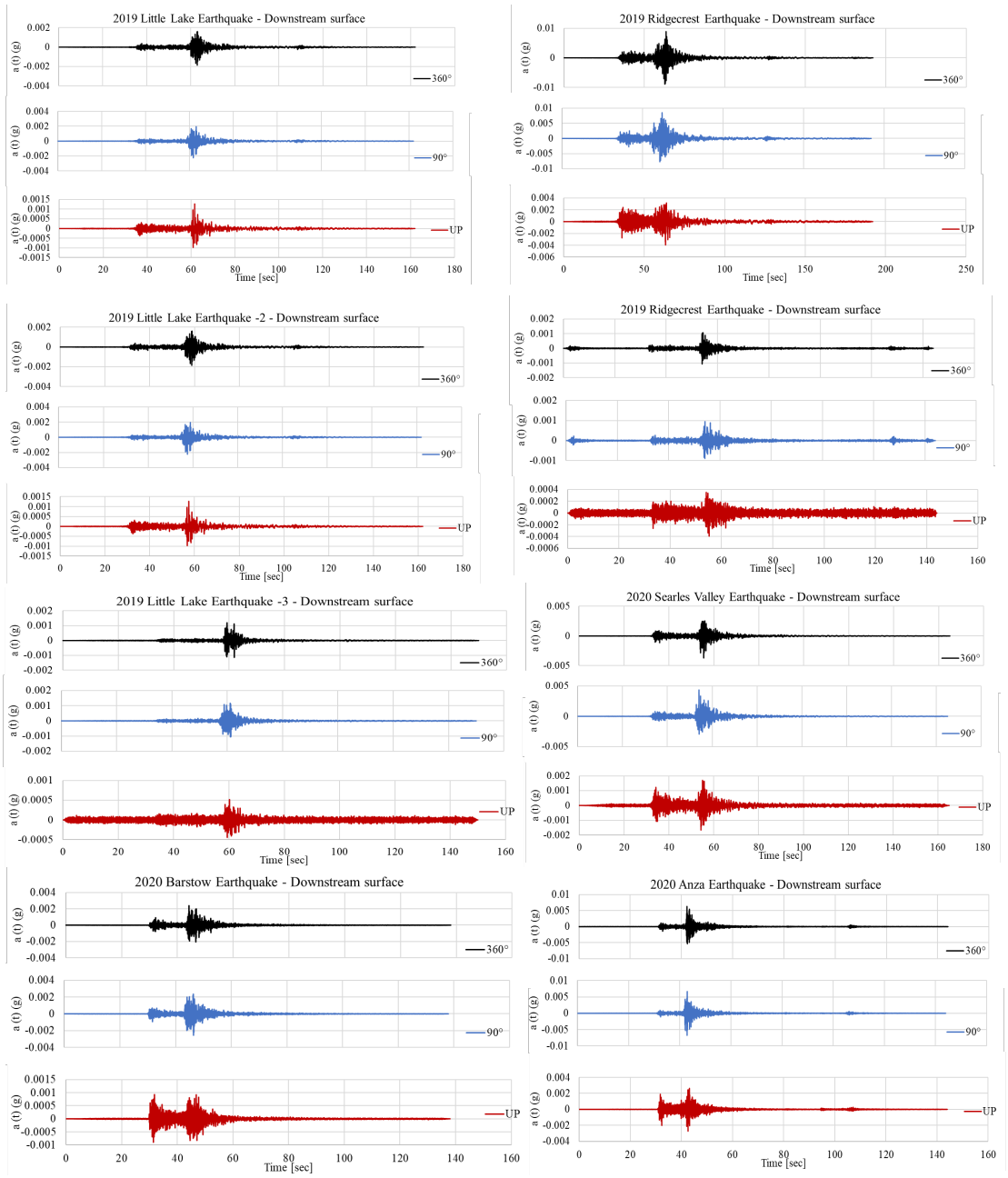

Figure 7. Acceleration time histories recorded downstream site (cont'd)

The results obtained are presented in Figure 8. Site effects as can be inferred from this figure indicates a resonance frequency between 6.1 and 7.5 Hz at the downstream site. The results show a consistent agreement of estimates for the HVSR, and the resonance frequency is estimated as 6.88 Hz (predominant period 0.145 sec) which is reasonable considering the stiff nature of the deposit with high shear wave velocity profile at the downstream site. The solid red line shows the average of the H/V curves obtained using 15 earthquake recordings. However, the results suggest that considerable uncertainties are associated when the amplification factors are investigated. These uncertainties are related to the assumptions involved in HVSR analysis. The main assumption of this analysis is that the horizontal and vertical ground motions at the firm

bedrock are identical and only the horizontal motions, not the vertical component, are amplified significantly by site conditions. Hence it should be carefully assessed if the HVSR bedrock is constant as discussed by Rong et al. (2017). This study also discussed that the vertical site response has a significant effect on the calculated HVSR curves. A careful examination should also be made for selecting the window length for the arrival of S-waves which contributes to uncertainties. All these aspects will be further studied in future studies.

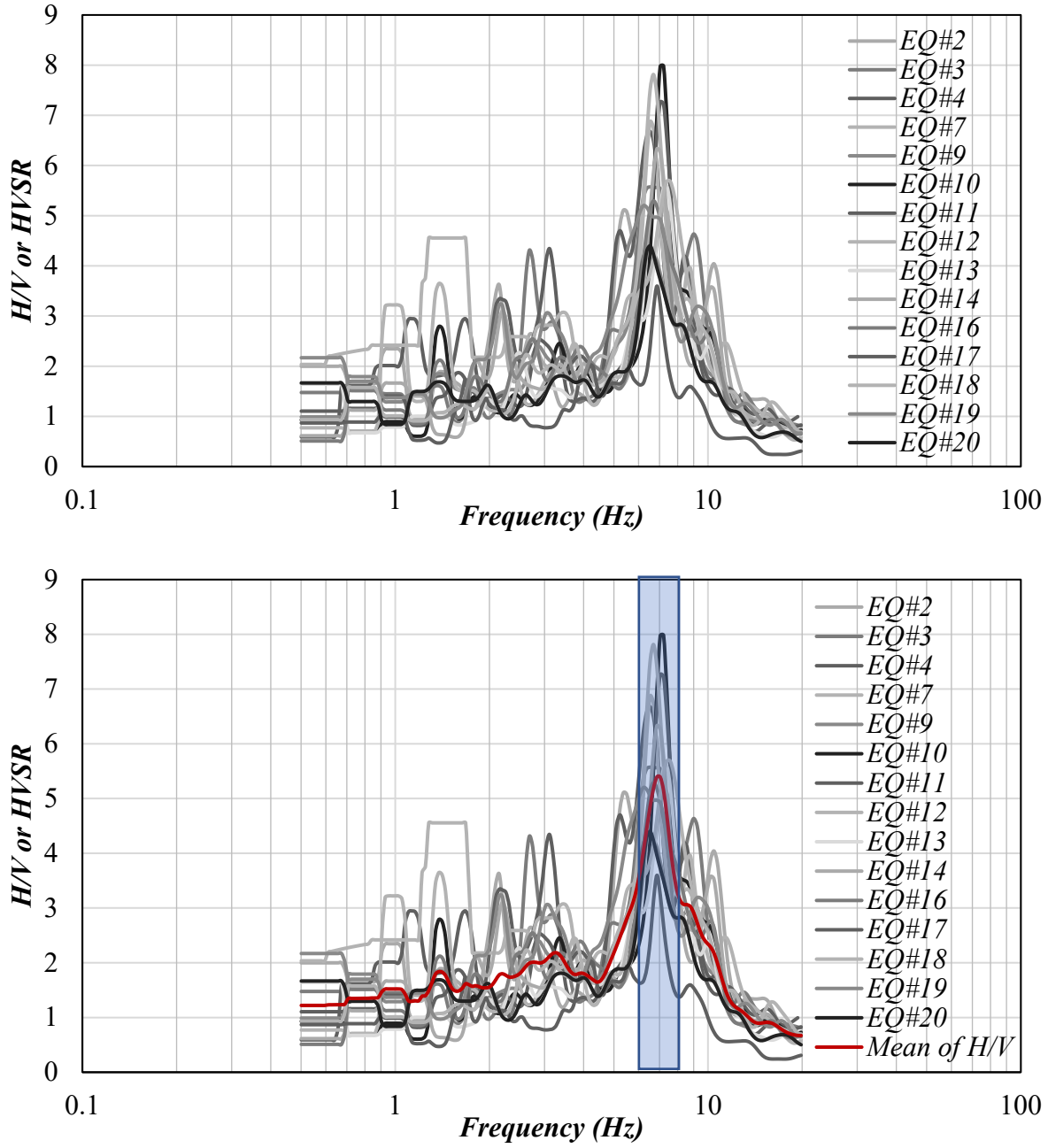

Figure 8. H/V ratios at the downstream site at Seven Oaks Dam for different events along with the average curve.

Table 4 presents the resonance frequency (f_0) and amplification factor (A_0) results for each earthquake recording at the downstream site along with moment magnitude (M_w), epicentral distance ($Epi_{dist.}$), and maximum ground acceleration (a_{max}). The effect of distance and depth of vibration source on the H/V ratios will be studied in future studies.

Table 4. Summary of the results for Seven Oaks Dam downstream site

EQ#	Earthquake Name	M_w USGS	Epi_{dst} (km)	a_{max} (g)			f_o	A_o
				360°	90°	UP		
2	Anza Earthquake	5	86.9	0.0115	0.0078	0.0059	6.14	3.82
3	Big Bear-02	4.7	-	0.0420	0.0607	0.0178	6.69	5.56
4	Big Bear City Earthquake	5	31.5	0.0419	0.0309	0.0125	6.70	6.59
7	San Bernardino Earthquake	4.5	19	0.0577	0.0705	0.0215	6.61	6.80
9	Ridgecrest Earthquake	6.5	180.8	0.0089	0.0085	0.0039	6.69	4.28
10	Searles Valley Earthquake	5.4	188.1	0.0011	0.0012	0.0005	7.43	6.65
11	Searles Valley Earthquake	5	183.9	0.0006	0.0008	0.0003	7.32	6.79
12	Searles Valley Earthquake	4.8	193.1	0.0006	0.0010	0.0004	6.66	7.75
13	Ridgecrest Earthquake	4.8	170.2	0.0011	0.0009	0.0004	6.92	4.78
14	Little Lake Earthquake	5.4	206.7	0.0019	0.0022	0.0013	7.08	6.14
16	Searles Valley Earthquake	4.6	173.2	0.0010	0.0013	0.0005	6.99	4.99
17	Little Lake Earthquake	4.9	207	0.0012	0.0012	0.0005	7.12	4.36
18	Barstow Earthquake	4.6	110.1	0.0024	0.0026	0.0009	7.48	5.68
19	Anza Earthquake	4.9	88	0.0063	0.0067	0.0027	6.57	5.03
20	Searles Valley Earthquake	5.5	169.6	0.0037	0.0043	0.0017	6.78	4.09

Site Response Analysis

1-D seismic site response analysis is performed using the software Deepsoil by Hashash et al. (2020) with an equivalent linear frequency domain method for the downstream site at Seven Oaks Dam. Site conditions at the downstream site are provided by Mejia and Dawson (2008) which are previously presented in Figure 5. A V_s profile for the downstream site is not fully available which restricts an accurate 1-D site response analysis, especially for the relatively soft layer of alluvium deposit, leading to larger uncertainty. A set of sensitivity analyses are performed to predict the surface recording by using the downhole recording at 53 ft as an input motion to compensate lack of V_s information. The results present an overall understanding of the site conditions however additional information is required for a more precise estimation of the amplification factors and site resonance frequency. Figure 9 presents the V_s profile used in the analysis of the downstream site.

In order to define the shear modulus degradation and damping characteristics of the site Rollins et al. (2020) study is used for the alluvium site which consists of gravelly materials and Idriss (1999) for the weathered rock. Figure 10 presents Fourier Amplitude Ratio determined for the downstream site by 1-D site response analysis along with the results obtained from HVSR analysis. The site response analysis was performed by using the 2009 San Bernardino Earthquake which is the only recording available at the downstream surface and downhole whose PGA is calculated as 0.0577 g, 0.0705 g, and 0.0215g for 360°, 90°, and vertical components respectively. The lack of adequate knowledge of the upper alluvium layer may potentially cause unrealistic amplification factors. When the HVSR curves are compared with

the theoretical amplification spectra obtained from site response analysis in Figure 10, it is observed that the resonance frequencies are mostly close (e.g., 5.3 Hz and 6.4 Hz) however the amplitudes are dramatically different. Further data is needed to compare the result of both methods which may be performed with a more accurate V_s profile and using several different ground motion recordings.

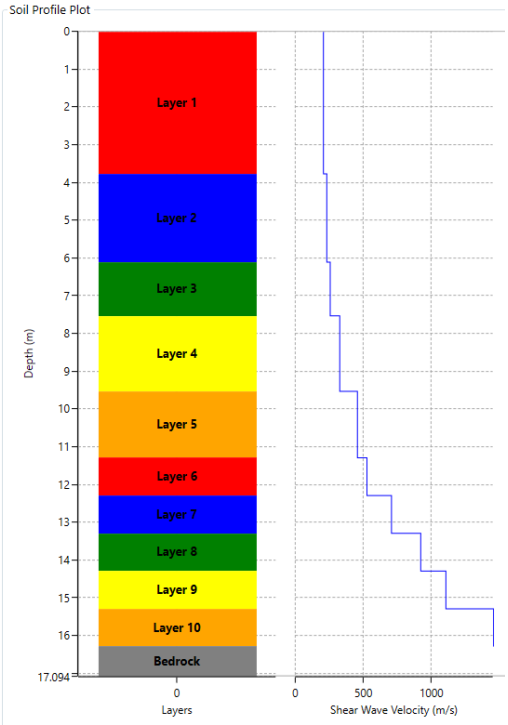

Figure 9. Estimated V_s profile of the downstream site at Seven Oaks Dam.

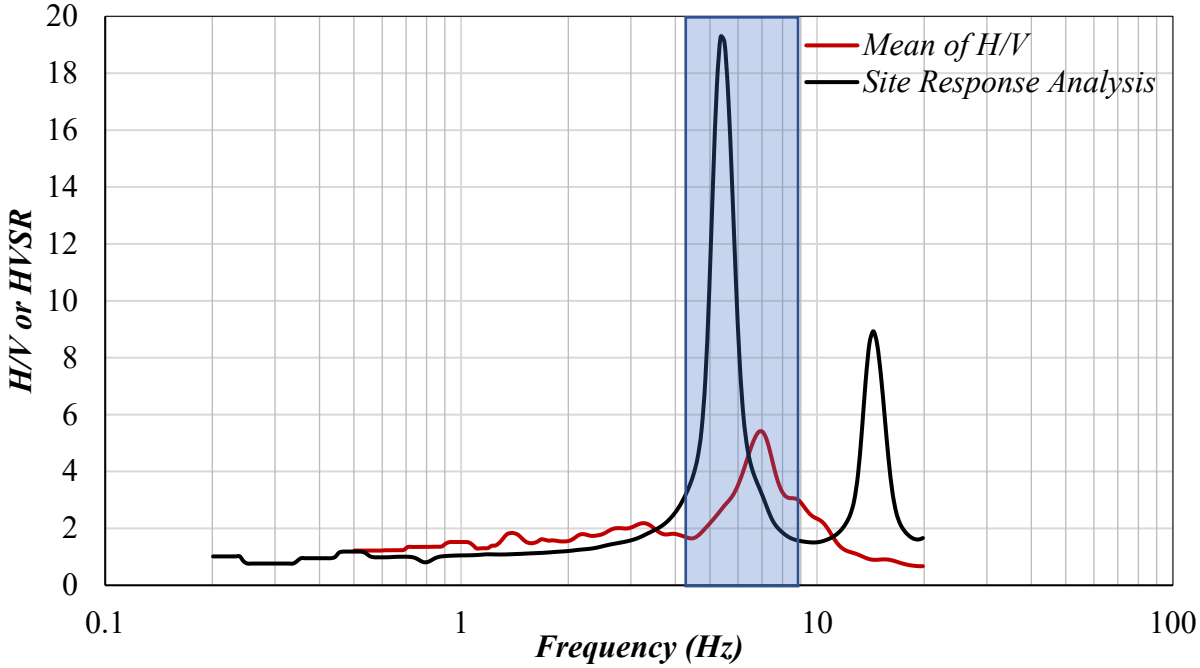

Figure 10. Comparison of HVSR and 1-D site response analysis results for the downstream site at Seven Oaks Dam.

Calculation of G_{max} and Damping

Seismic recordings of vertical array of accelerometers in the downstream site is used for extracting shear stress-strain loops to determine the corresponding value of maximum shear modulus, G_{max}. Following the procedure by Abdel-Ghaffar and Scott (1979a, b), Lin and Chao (1990), Koga and Matsuo (1990), and Lin (1994) and adopted by Zeghal and Elgamal (1994), shear strain versus shear stress loops are investigated at the downstream site by using the 2009 San Bernardino Earthquake recordings which is the only recording available at the downstream surface and downhole at 53 ft. Average shear stress-strain values are determined with the following formulations given in Equations 1 and 2 by Zeghal and Elgamal (1994).

$$\tau_z = \frac{1}{2}\rho z\left(a_2 + \left(a_2 + (a_1 - a_2)\left(\frac{z}{h}\right)\right)\right) \quad \text{Eq. (1)}$$

$$\gamma = (d_1 - d_2)/h \quad \text{Eq. (2)}$$

where τ_z = average shear stress, ρ = density of the soil layer, a_2=horizontal acceleration at the surface, a_1=horizontal acceleration at depth z, $d_1 and\ d_2$ =displacement at the surface and downhole and h=the layer thickness.

The strong ground motion data obtained from the 2009 San Bernardino Earthquake is pass-filtered and the analysis is performed for the 90° component which is the dominant direction. Figure 11 shows the acceleration time history for the 90° component of the 2009 San Bernardino Earthquake. As can be inferred from this figure, ground acceleration has a low amplitude between 10.4-13.6 sec. Figure 12a presents the shear strain versus shear stress graph for the 2009 San Bernardino Earthquake for the entire motion and Figure 12 b presents the stress-strain curve for the 11.0-11.2 sec cycle which is used to determine the G_{max} value at the downstream site considering the small shear strain levels at that time window. This G_{max} value represents an average estimate of the alluvium layer and weathered rock. G_{max} can also be estimated directly based on V_s value with the expression of $G_{max}=\rho \cdot V_s^2$. Based on assumed V_s value for alluvium, the method of extracting G_{max} based on strong ground motion values results in reasonable estimates.

Small strain equivalent linear (secant) shear modulus is estimated from shear stress-strain loops. The results cannot be evaluated as the shear wave velocity profile is not available for the downstream sites. But considering that an estimated V_s profile was used in site response analysis the results are reasonable which should be further investigated with more information.

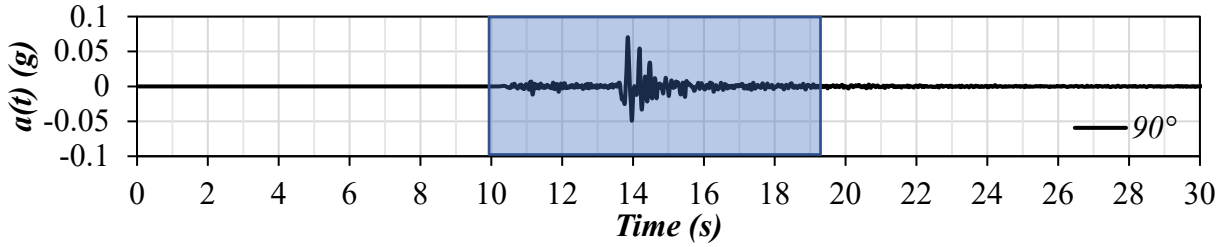

Figure 11. Acceleration time histories of 2009 San Bernardino Earthquake at downstream site surface

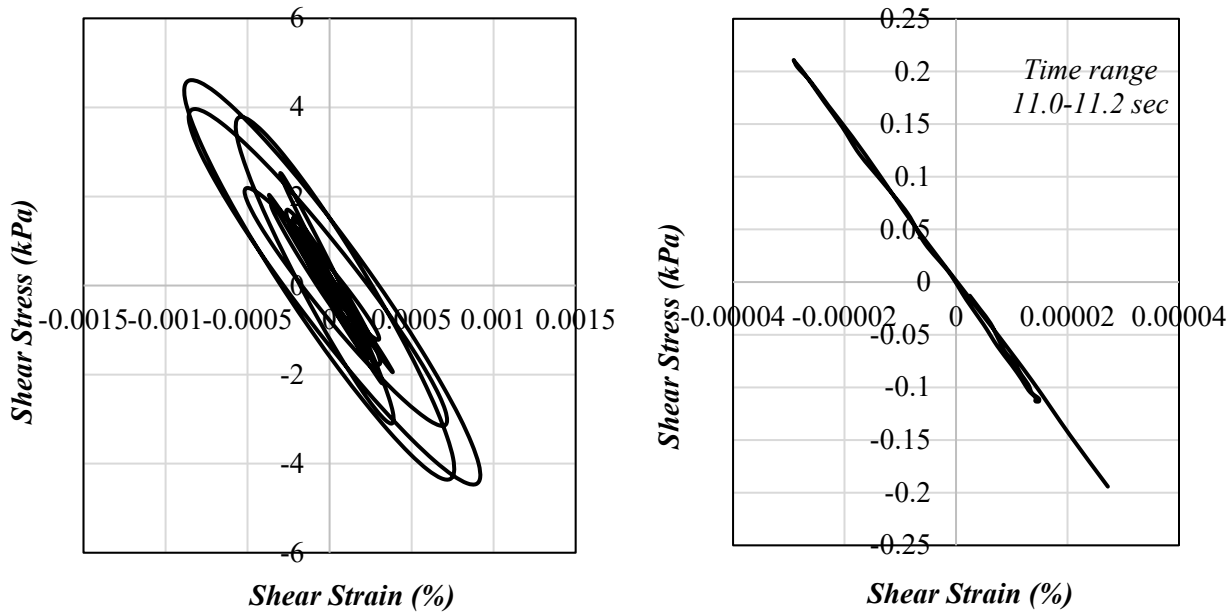

Figure 12. Shear strain versus shear stress graph for the 2009 San Bernardino Earthquake a) for the entire motion and b) for 11-11.2 sec cycle.

Conclusions

The purpose of this paper is to improve our understanding of the seismic response of earth dams and create a framework for strong-motion data processing that can lead to improvement in the seismic design code provisions and practices with respect to earth dams. For this purpose, CSMIP earthquake recordings from different locations on the dams (toe, crest, abutment, etc.) are assessed to develop Horizontal to Vertical (H/V) spectral ratios for selected dam locations estimated directly from the recorded motions to assess the fundamental resonance frequency of the sites and amplification factors. For this purpose, the results of Seven Oaks Dam are presented as an illustrative example. 15 earthquakes were recorded by Seven Oaks downstream site. These recordings were assessed by using Geopsy software and for each recording H/V ratios are calculated following the procedure offered by Nakamura (1989). The average of the H/V ratios are also determined which indicates the predominant frequency for the downstream site as 6.88 Hz. Amplification factors for each strong motion station are obtained from the H/V curve which has large uncertainties. 1-D site response analyses are performed; however, the lack of an accurate V_s profile enables an accurate comparison of the available models. Further research is needed to verify the applicability of the current method to assess the amplification factors. Following the procedure by Abdel-Ghaffar and Scott (1979a, b), Lin and Chao (1990), Koga and Matsuo (1990), and Lin (1994) and adopted by Zeghal and Elgamal (1994), shear strain versus shear stress loops are investigated at the downstream site by using the 2009 San Bernardino Earthquake recordings and results found reasonable for a stiff site as the downstream of Seven Oaks Dam. However, this suggests that this case history does not fully satisfy the minimum requirements of the methods discussed in this study, and further site investigation data and digital recording at the vertical arrays at the crest surface and downstream sites are required to assess dynamic properties.

Acknowledgments

This study is funded by the California Strong Motion Instrumentation Program (CSMIP).

References

Abdel-Ghaffar, A. M. and Scott, R. F. (1979b), `Shear moduli and damping factors of earth dam', Journal of the Geotechnical Engineering Division, ASCE 105(GT12), 1405{1426.

Abdel-Ghaffar, A. M., and Scott, R. F. (1979a), "Analysis of earth dam response to earthquakes", Journal of Geotechnical Engineering Division, Vol. 105, No. 12, pp. 1379-1404.

Al Yuncha, Z. & Luzon, F., 2000. On the horizontal-to-vertical spectral ratio in sedimentary basins, Bull. seism. Soc. Am., 90, 1101–1106.

Ambraseys, N. N. (1960b), The seismic stability of earth dams, in `Proceedings of the 2nd World Conference on Earthquake Engineering', Tokyo.

Bard, P.-Y., 1998. Microtremor measurements: a tool for site effect estimation? Proceeding of the Second International Symposium on the Effects of Surface Geology on Seismic Motion, Yokohama, Japan, 3, 1251–1279.

Bard, P.-Y., SESAME-team, 2004. Guidelines for the Implementation of the H / V Spectral Ratio Technique on Ambient Vibrations Measurements, Processing and Interpretation, SESAME European research project EVG1-CT-2000–00026.

Bour, M., Fouissac, D., Dominique, P. & Martin, C., 1998. On the use of microtremor recordings in seismic microzonation, Soil Dyn. and Earthq. Eng., 17, 465–474.

Dakoulas, P. and Gazetas, G. (1985), `A class of inhomogeneous shear models for seismic response of dams and embankments', Soil Dynamics and Earthquake Engineering 4(4), 166{182.

Dakoulas, P. and Gazetas, G. (1986), `Seismic lateral vibration of embankment dams in semi-cylindrical valleys', Earthquake Engineering and Structural Dynamics 13(1), 19{40.

Dakoulas, P. and Gazetas, G. (1987), `Vibration characteristics of dams in narrow canyons', Journal of Geotechnical Engineering 113(8), 899{904.

Fah, D., Kind, F. & Giardini, D., 2001. A theoretical investigation of average H/V ratios, Geophys. J. Int., 145, 535–549.

FEMA (2005) Federal Guidelines for Dam Safety: Earthquake Analyses and Design of Dams

Field, E. & Jacob, K., 1993. The theoretical response of sedimentary layers to ambient seismic noise, Geophys. Res. Lett., 20, 2925–2928.

Gazetas, G. (1987), `Seismic response of earth dams: some recent developments', Soil Dynamics and Earthquake Engineering 6(1), 3{47.

Gitterman, Y., Zaslavsky, Y., Shapira, A. & Shtivelman, V., 1996. Empirical site response evaluations: case studies in Israel, Soil Dyn. and Earthq. Eng., 15, 447–463.

Haddadi, H. 2019 “Updates on the Center for Engineering Strong Motion Data (CESMD), Presentation at the 2019 COSMOS Technical Session

Hashash, Y.M.A., Musgrove, M.I., Harmon, J.A., Ilhan, O., Xing, G., Numanoglu, O., Groholski, D.R., Phillips, C.A., and Park, D. (2020). "DEEPSOIL 7, User Manual". Urbana, IL, Board of Trustees of University of Illinois at Urbana-Champaign.

Koga, Y., and Matsuo, O. (1990), “Shaking table tests of embankments resting on liquefiable sandy ground”, Soils and Foundations, Vol. 30, No. 4, pp. 162-174.

Konno, K. & Ohmachi, T., 1998. Ground-motion characteristics estimated from spectral ratio between horizontal and vertical components of microtremor, Bull. seism. Soc. Am., 88, 228–241.

Kudo, K., 1995. Practical estimates of site response. State-of-art report, Proceedings of the fifth International Conference on Seismic Zonation, Nice, France.

Lachet, C. & Bard, P.-Y., 1994. Numerical and theoretical investigations on the possibilities and limitations of Nakamura’s technique, J. Phys. Earth,42, 377–397.

Lermo, J. & Chavez-Garcia, F.J., 1994. Site effect evaluation at Mexico city: dominant period and relative amplification from strong motion and microtremor records, Soil Dyn. and Earthq. Eng., 13, 413–423.

Lermo, J., and Chávez-García, F. J. (1993), “Site effect evaluation using spectral ratios with only one station”, Bulletin of the seismological society of America

Lin, J.S. (1994), “Extraction of dynamic soil properties using extended Kalman filter”, Journal of Geotechnical Engineering, Vol. 120, No. 12, pp. 2100-2117.

Lin, J.S., and Chao, B.K. (1990), “Estimation of shear moduli and damping factors of earth dam materials”, Earthquake Engineering & Structural Dynamics, Vol. 19, No. 6, pp. 891-910.

Maresca, R., Castellano, M., De Matteis, R., Saccorotti, G. & Vaccariello, P., 2003. Local site effects in the town of Benevento (Italy) from noise measurements, Pure appl. Geophys., 160, 1745–1764.

Mejia, L. and Dawson, E. (2008) Analysis of Seismic Response of Seven Oaks Dam, Data Utilization Report, CSMIP, California Dept of Conservation, Division of Mines and Geology

Mejia, L. H. and Seed, H. B. (1983), `Comparison of 2-D and 3-D dynamic analyses of earth dams', Journal of Geotechnical Engineering, ASCE 109(11), 1383{1398.

Mucciarelli, M., 1998. Reliability and applicability of Nakamura's technique using microtremors: an experimental approach, J. Earthq. Eng., 2, 625–638.

Nakamura, Y., (1989), "A method for dynamic characteristics estimation of subsurface using microtremor on the ground surface", QR of Railway Technical Research Institute, Vol 30, pp. 25-33

Nakamura, Y., 1996. Real-time information systems for hazards mitigation, Proceedings of the 11th World Conference on Earthquake Engineering, Acapulco, Mexico.

Nakamura, Y., 2000. Clear identification of fundamental idea of Nakamura's technique and its applications, Proceedings of the 12th World Conference on Earthquake Engineering, Auckland, New Zealand.

Nogoshi, M. and Igarashi, T. (1970). On the propagation characteristics of microtremors. J. Seism. Soc. Japan 23, 264-280(in Japanese with English abstract).

Nogoshi, M. and Igarashi, T. (1971). On the amplitude characteristics of microtremors. J. Seism. Soc. Japan. 24, 24-40(in Japanese with English abstract).

Rodriguez, H.S. & Midorikawa, S., 2003. Comparison of spectral ratio techniques for estimation of site effects using microtremor data and earthquake motions recorded at the surface and in boreholes, Earthq. Eng. Struct. Dyn., 32, 1691–1714.

Rong, M., Fu, L. Y., Wang, Z., Li, X., Carpenter, N. S., Woolery, E. W., & Lyu, Y. (2017). On the Amplitude Discrepancy of HVSR and Site Amplification from Strong-Motion ObservationsOn the Amplitude Discrepancy of HVSR and Site Amplification from Strong-Motion Observations. Bulletin of the Seismological Society of America, 107(6), 2873-2884.

Seekins, L.C., Wennerberg, L., Marghereti, L. & Liu, H.-P., 1996. Site amplification at five locations in San Fransico, California: a comparison of S waves, codas, and microtremors, Bull. seism. Soc. Am., 86, 627–635.

Tokeshi, J.C. & Sugimura, Y., 1998. On the estimation of the natural period of the ground using simulated microtremors, Proceeding of the Second International Symposium on the Effects of Surface Geology on Seismic Motion, Yokohama, Japan, 2, 651–664.

US Bureau of Reclamation (2015) Embankment Dams: Chapter 13: Seismic Analysis and Design, Design Standards No 13

Wakamatsu, K.&Yasui, Y., 1996. Possibility of estimation for amplification characteristics of soil deposits based on ratio of horizontal to vertical spectra of microtremors, Proceedings of the 11th World Conference on Earthquake Engineering, Acapulco, Mexico.

Wathelet, M., B. Guillier, P. Roux, C. Cornou and M. Ohrnberger (2018). Rayleigh wave three-component beamforming: signed ellipticity assessment from high-resolution frequency-wavenumber processing of ambient vibration arrays. Geophysical Journal International, 215(1), 507-523.

Wood, C., Ellis, T., Teague, D., Cox, B., 2014. Analyst I: Comprehensive analysis of UTexas1 surface wave dataset, ASCE GeoCongress: Geocharacterization & modeling for sustainability: 820-829.

Zeghal, M., and Elgamal, A.-W. (1994), "Analysis of site liquefaction using earthquake records", Journal of geotechnical engineering, Vol. 120, No. 6, pp. 996-1017.